FLOW AND PRESSURE DROP OF HIGHLY VISCOUS FLUIDS IN SMALL APERTURE ORIFICES

A Thesis
Presented to
The Academic Faculty

By

Lalit Kumar Bohra

In Partial Fulfillment
Of the Requirements for the Degree
Masters of Science in Mechanical Engineering

Georgia Institute of Technology
June 2004

FLOW AND PRESSURE DROP OF HIGHLY VISCOUS FLUIDS IN SMALL APERTURE ORIFICES

Approved by:

Dr. Srinivas Garimella, Chair

Dr. G. Paul Neitzel

Dr. S. Mostafa Ghiaasiaan

Date Approved: July 8, 2004

DEDICATION

To my parents and siblings who had always shown faith in me and guided me through difficult times

ACKNOWLEDGEMENTS

First and foremost, I sincerely express my deep sense of gratitude towards my advisor Dr. Srinivas Garimella for his expert guidance and continuous support throughout the course of this project.

I am also deeply indebted to all the members of Sustainable Thermal Systems Laboratory for their support in one or other way. Special thanks to Matthew Determan for his guidance during the early stage of my experimental work. Special thanks are also due to Tim Ernst and Jesse Killion for their expert advices on experimentation and documentation respectively. I am extremely grateful to Leo Mincks for the help in overcoming troubles in experiments. My thanks are also due to Akhil Agarwal and Biswajit Mitra for their support.

I am also grateful to my committee members for their patient perusal of my thesis and valuable comments.

Lalit Kumar Bohra

TABLE OF CONTENTS

LIST OF FIGURES

LIST OF TABLES

SYMBOLS

A	cross sectional area (m^2)
C	energy dissipation constant
C_c	contraction coefficient
C_d	orifice discharge coefficient
C_{du}	ultimate orifice discharge coefficient
C_p	velocity profile coefficient
C_v	viscosity coefficient
C_{ve}	vena contracta coefficient
C_μ	viscous coefficient
D	pipe diameter (m)
d	orifice diameter (m)
Eu	Euler number ($2\Delta P/\rho V^2$)
f	friction factor
g	gravitational constant (9.81 m/s^2)
K_L	loss coefficient for sudden expansion
L	length (m)
P	Pressure (kPa)
Pr	Prandtl number
Q	flow rate (m^3/s)
Re	Reynolds number ($\rho Vd/\mu$)
r	orifice radius (m)

St	Strouhal Number
T	temperature (°C)
V	average velocity (m/s)

Greek Letters

β	diameter ratio (d/D)
Δ	differential
ε	roughness (m)
κ	shear rate
μ	dynamic viscosity (kg/m-s)
ρ	density (kg/m^3)
σ	surface tension (N/m)
τ	shear stress
λ_0	inverse shear rate at the inception of shear thinning

Sub-scripts and Super-scripts

eff	effective
f	frictional
g	gas
ge	generalized
l	liquid
lam	laminar
seg	segment

t	turbulent
tp	two-phase
turb	turbulent

SUMMARY

A study of the pressure drop characteristics of the flow of highly viscous fluids through small diameter orifices was conducted to obtain a better understanding of hydraulic fluid flow loops in vehicles. Pressure drops were measured for each of nine orifices, including orifices of nominal diameter 0.5, 1 and 3 mm, and three thicknesses (nominally 1, 2 and 3 mm), and over a wide range of flow rates ($2.86\times10^{-7} < Q < 3.33\times10^{-4}$ m^3/s). The fluid under consideration exhibits steep dependence of the properties (changes of several orders of magnitude) as a function of temperature and pressure, and is also non-Newtonian at the lower temperatures. The data were non-dimensionalized to obtain Euler numbers and Reynolds numbers using non-Newtonian treatment. It was found that at small values of Reynolds numbers, an increase in aspect ratio (length/diameter ratio of the orifice) causes an increase in Euler number. It was also found that at extremely low Reynolds numbers, the Euler number was very strongly influenced by the Reynolds number, while the dependence becomes weaker as the Reynolds number increases toward the turbulent regime, and the Euler number tends to assume a constant value determined by the aspect ratio and the diameter ratio. A two-region (based on Reynolds number) model was developed to predict Euler number as a function of diameter ratio, aspect ratio, viscosity ratio and generalized Reynolds number. This model also includes data at higher temperatures ($20 \leq T \leq 50^oC$) obtained by Mincks (2002). It was shown that for such highly viscous fluids with non-Newtonian behavior at some conditions, accounting for the shear rate through the generalized Reynolds number

resulted in a considerable improvement in the predictive capabilities of the model. Over the laminar, transition and turbulent regions, the model predicts 86% of the data within $\pm 25\%$ for $0.32 < l/d$ (orifice thickness/diameter ratio) < 5.72, $0.023 < \beta$ (orifice/pipe diameter ratio) < 0.137, $0.09 < Re_{ge} < 9677$, and $0.0194 < \mu_{ge} < 9.589$ (kg/m-s).

1. INTRODUCTION

In many automotive and hydraulic applications, oil flows through small openings that can be simulated by small-diameter, square-edged orifices. These fluids (oils) are highly viscous, and in many instances, their properties vary with temperature and pressure. Some of these also exhibit non-Newtonian behavior, at least at the very low temperatures. Rheological (so called non-Newtonian) fluids are very frequently encountered in food processing and chemical industries. In such applications, the flow remains laminar even at large flow rates. The most commonly available orifice correlations are those used for metering applications and developed for large diameter and small aspect ratios, often in turbulent flow. Also in practical applications, orifices have varying thicknesses governed by considerations such as component strength and manufacturability. The proposed research therefore addresses the problem of relating flow rate to pressure drop across square-edged orifices over a wide range of orifice geometries and operating conditions.

Considerable research in the study of orifice flow has been devoted to applications involving flow meters. These orifices typically have diameter ratios (β) in the range of 0.2 to 0.75 and aspect ratios (l/d) less than 1. Figure 1.1 shows the orifice geometry and terms that will be used throughout this thesis. Orifices of interest for the present study have diameter ratios of 0.022, 0.044 and 0.137, with aspect ratios ranging from 0.33 to 6. Additionally, the fluid used in this investigation is highly viscous (0.151 kg/m-s $< \mu_{ge} <$ 9.589 kg/m-s) in nature.

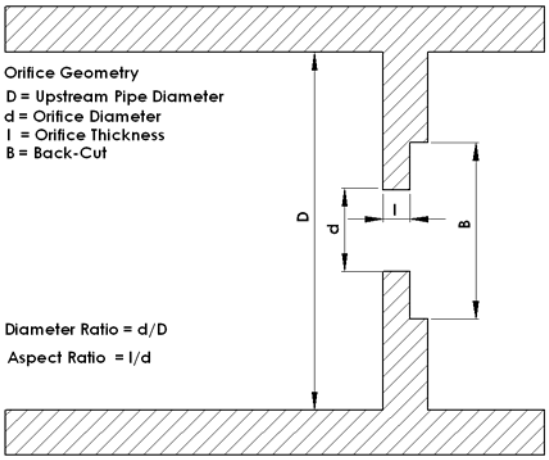

Figure 1.1 Orifice Geometry

The standard convention for relating orifice flow rate to differential pressure is through the use of the orifice discharge coefficient (C_d) as seen in Equation (1.1).

$$C_d = \frac{Q}{A_{or}}\sqrt{\frac{\rho}{2\Delta P}} \tag{1.1}$$

Mincks (2002) conducted an experimental study to find pressure drop characteristics of the fluid under investigation at slightly lower viscosities (higher temperatures, $20 \leq T \leq 50^{o}C$). He related the non-dimensional pressure drop to the orifice geometry and Reynolds number. Similarly, past research (Lichtarowicz *et al.* 1965; Sahin and Ceyhan 1996) has also shown that at low flow rates, C_d is generally considered to be a function of the aspect ratio, the diameter ratio ($\beta = d/D$), and the orifice Reynolds number (Re). At high Reynolds numbers, the effects of aspect ratio and Reynolds number decrease, with C_d depending primarily on diameter ratio (Grose 1985). Non-dimensional pressure drop can also be expressed as an Euler number Eu, which depends on the orifice geometry, and Reynolds number as follows:

$$Eu = 1/C_d^2 = f(Re, \beta, l/d) \tag{1.2}$$

1.1 Orifice Terminology

Orifices are categorized depending upon the upstream and downstream surface profiles, with these specific geometric details being designed for specific applications. Figure 1.2 shows the geometries for several different types of orifices, while Figure 1.3 shows the standard tapping arrangements generally used by orifice measuring devices (ASME 1990). The dimensions given in Figures 1.3c and 1.3d are based on characteristics of the flow meter and are influenced by the installed geometry. For the pipe tap arrangement, the dimensions d1 and d2 are usually either equal to each other (d1 = d2) or based on the pipe diameter such that d1 = D and d2 = D/2.

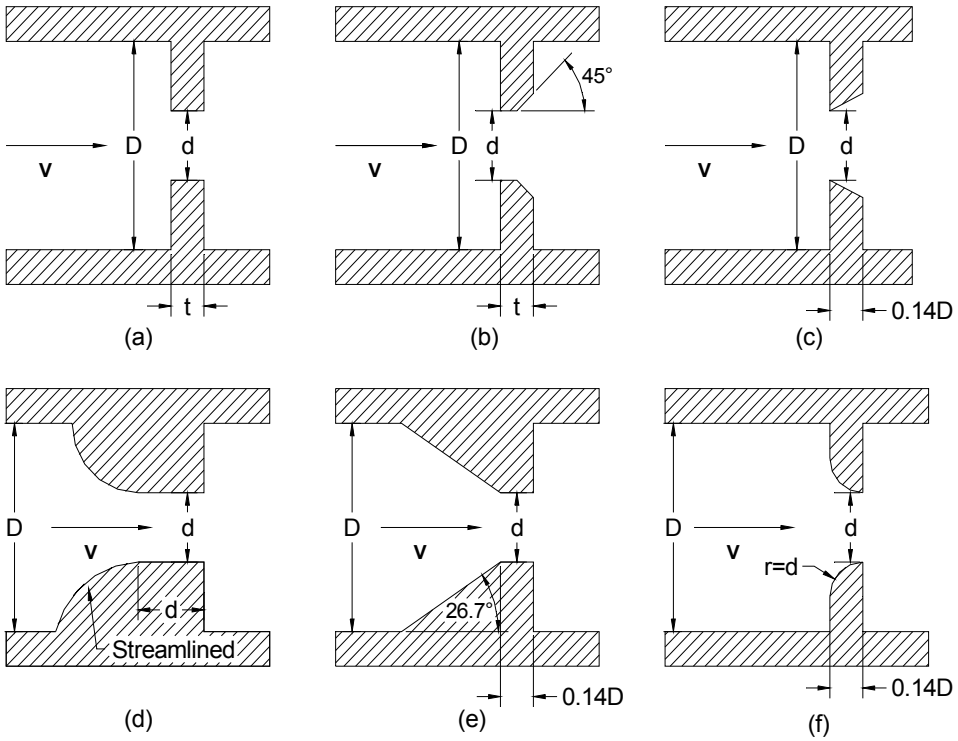

Figure 1.2 Geometries of Orifice Plates (Mincks 2002): (a) Square-Edged; (b) ASME Standard (Square-Edged with 45° Back-cut); (c) Sharp-Edged; (d) Streamlined-Approach (Rouse and Jezdinsky 1966); (e) Sloping-Approach (Zhang and Cai 1999); (e) Quadrant-Edged

The taps for vena contracta meters are somewhat different where the location of the downstream tap is based on the lowest pressure in the flow profile. For these meters, the upstream tap is located at d1 = D, while the downstream tap usually lies between 0.3D and D.

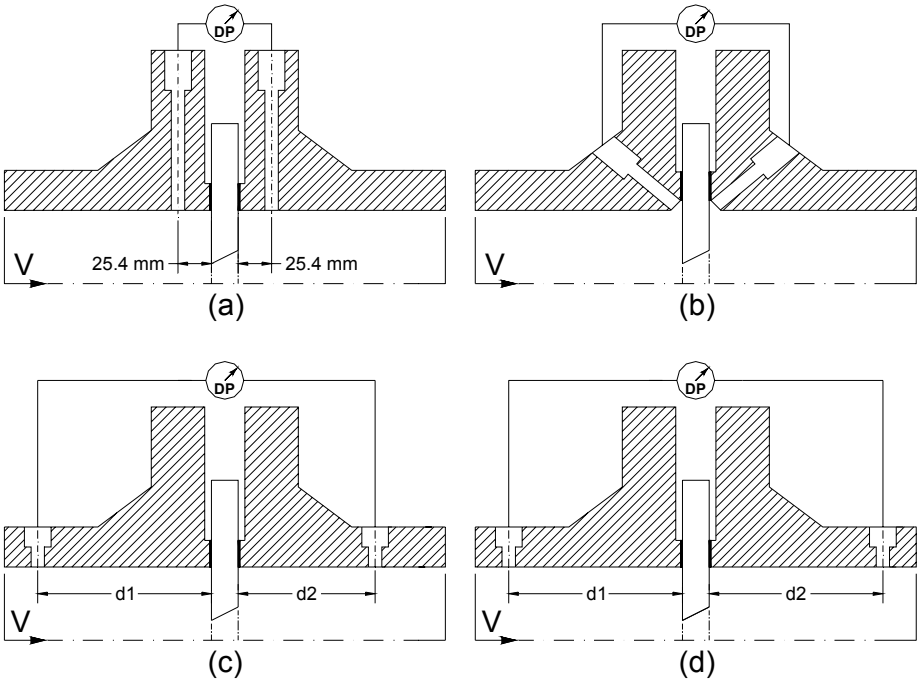

Figure 1.3 Pressure Tapping Arrangements (Mincks 2002): (a) Flange Taps; (b) Flange Corner Taps; (c) Vena Contracta Tap; (d) Pipe Taps

1.2 Research Objectives

As discussed in the previous sections, there is a need to understand orifice flow better for highly viscous fluids and for certain orifice geometries. Therefore, the research objectives of this study are defined as follows:

- Determine the flow rate for a given pressure drop for several different orifice plates for fluid viscosities of $0.151 < \mu_{ge} < 9.589$ kg/m-s.
- Analyze the effects of temperature and orifice geometry on pressure drop - flow characteristics.
- Develop a model for the flow of viscous fluids through small diameter ratio orifices that accounts for the effects of geometry and fluid properties.

1.3 Thesis Organization

This thesis is organized in several chapters as follows:

- Chapter 2 provides background information available in literature on experimental and theoretical studies of orifice flow characteristics and discusses the need for further research in this area.
- Chapter 3 describes the test facility used for this study and the procedures adopted for conducting the experiments.
- Chapter 4 presents experimental results in terms of pressure drop-flow characteristics. Effect of geometry and fluid temperature is also presented through these results.
- Chapter 5 presents comparison of the results from current study with those available in literature. This chapter also presents non-dimensional analyses and the development of the orifice flow model.
- Chapter 6 summarizes the important conclusions of this study and provides recommendations for further work in this area

2. LITERATURE REVIEW

Orifice flow has been studied in the past for several applications. Available literature on the subject of small-diameter orifices is categorized here into incompressible Newtonian flow, compressible Newtonian flow and non-Newtonian flow as it applies to the current study. The parameter that has received the most attention, or has been used extensively for characterizing orifice flow in such studies has been the discharge coefficient. Other parameters are pressure drop, flow rate and non-dimensional pressure drop (Euler number).

2.1 Incompressible Newtonian Flow

As early as 1929, Johansen (1930) conducted a visualization study of the flow characteristics of sharp-edged orifices. Using water, Castor oil ($\nu = 1.209\times10^{-3}$ m^2/s at 18°C) and mineral oil ($\nu = 1.14\times10^{-4}$ m^2/s at 18°C) as the working fluid, tests were conducted to determine the discharge coefficients for orifices with five different diameter ratios (β = 0.090, 0.209, 0.401, 0.595, and 0.794) over a range of Reynolds numbers from less than 1.0 to 25,000. He tried to interpret the resulting plot of the discharge coefficients based on the flow mechanisms observed in the dye injection test. He found that for Re < 10, C_d increases linearly and corresponds to the steady flow conditions seen in the dye test. A further increase in Reynolds number up to a value of 250 results in a nonlinear increase in C_d up to its maximum, and corresponds to the formation of a divergent jet in the flow patterns. The value of C_d then begins to decrease as vortices

appear in the flow until it reaches a steady value of approximately 0.615 as the flow becomes turbulent at Re > 2000. Johansen also notes that as the diameter ratio increases, the Reynolds number at which these flow transitions occur is higher. Thus, the flow remains laminar at higher Reynolds numbers for increased diameter ratios.

In another experimental study to establish an extensive plot of C_d versus Reynolds number, Tuve and Sprenkle (1933) conducted over 500 experiments for the Bailey Meter Company. Tests were conducted with water, light paraffin oil, light motor oil, and heavy motor oil ($\nu = 1.62\times10^{-3}$ m^2/s) as the working fluids over the range of $4 < Re < 40{,}000$. The eight orifices used in the testing were constructed of brass, monel and stainless steel, with thicknesses of 0.794 mm ($^1/_{32}$ in.) and diameter ratios ranging from 0.2 to 0.8. The orifices were beveled at 45° on the downstream side to produce an orifice edge length of 0.397 mm ($^1/_{64}$ in.). Based on the results of their experiments, the authors recommended that orifice meters should have diameter ratios between 0.2 and 0.5, and that they only be used for flow rates corresponding to $Re \geq 100$. They also compared their results with data from authors such as Johansen (1930), Witte (1928), and Hodgson (1929) and proposed that the slight differences in their results were due to a lack of similarity in variables such as orifice bevel angle or pipe diameter.

Medaugh and Johnson (1940) constructed a test facility that could measure flow rate and pressure drop across brass orifices at various conditions using water as the test fluid. Orifices were constructed from 6.35 mm (0.25 in.) brass sheet with diameters ranging from 6.35 to 50.80 mm (0.25 to 2 in.) and pressure drops ranging from approximately 2.41 to 358.5 kPa (0.35 to 52 psi). It was observed that as the flow rate through the orifice increased, the discharge coefficient decreased and that as the orifice

diameter increased, the discharge coefficient decreased for the same pressure drop. The authors determined that if the flow rate was increased enough, the discharge coefficient would eventually decrease to a value of 0.588, which was 6% lower that the data from Smith and Walker (1923) that were widely used at the time. This was attributed to potential problems in the Smith and Walker data due to bowing of the thin plate from the pressure, or from a depression that might have occurred around the orifice opening during the drilling process.

The influence of other parameters on C_d such as aspect ratio started gaining attention by the early 1960s. In 1965, Lichtarowicz et al. (1965) presented the results of investigations by James (1961), Sanderson (1962) and Morgan (1963), who examined the effects of aspect ratio on the discharge coefficients of square-edged orifices. Testing by these three investigators was conducted on orifices with aspect ratios ranging from 0.5 to 10 with $1 < Re < 50{,}000$. Lichtarowicz et al. (1965) then compared C_d values from these investigations with data from previous investigations and found a correlation between the aspect ratio and the maximum or ultimate value of the discharge coefficient (C_{du}). As the aspect ratio increases from 0 to approximately 1, C_{du} increases linearly from 0.61 to 0.78, while in the range of aspect ratios from 1 to 2, the increase is non-linear and achieves a maximum value of 0.81. Further increases in aspect ratio result in a gradual linear decrease in C_{du} to a value of 0.74 at an aspect ratio of 10. Based on their results, the authors recommended changes to the previously proposed equations for C_d and C_{du}.

Alvi et al. (1978) compared the flow characteristics of nozzles and sharp-edged orifices to those of quadrant-edged orifices. They conducted tests on these flow geometries with diameter ratios of 0.2, 0.4, 0.6, and 0.8 for each geometry, and orifice

Reynolds numbers in the range of 1 to 10000. They found that quadrant-edged orifices exhibit pressure drops similar to those of sharp-edged orifices at low Reynolds numbers, while pressure drops at high Reynolds numbers are closer to pressure drops in nozzles. They also suggest that the flow characteristics of orifices can be divided into four regimes: Fully Laminar Region, Critical Reynolds Number Region, Re-laminarizing Region, and Turbulent Flow Regime.

During the 1970s orifice-meter pressure-drop equations published by engineering societies and meter manufactures received further scrutiny. Miller (1979) compared laboratory flow data from different orifice-type flow meters with two commonly used equations for predicting the flow characteristics of these flow meters: the ASME (1971)-AGA (1955) equation, and the ISO-5167 (1978) or Stolz (1975) equation. By using statistical analysis, he found that for flange tap orifice meters with $0.25 < \beta < 0.75$ and pipe diameters from 102 to 610 mm (4 to 24 in.), these equations are accurate to ± 1%, with the Stolz (1975) equation being better. He also states that based on the work of Miller and Kneisel (1974), it would be possible to further reduce these uncertainties to ±0.5% with better data.

Dagan et al. (1982) provided an infinite-series solution for creeping viscous flow through orifices (pores) of low and moderate aspect ratios. The series solution was obtained by dividing the flow field in two simply bounded regions: a cylindrical volume bounded by the walls of the pore and the entrance and exit planes, and second, an infinite half space outside the orifice. The streamline patterns were computed numerically for $0.25 < l/d < 2$ and they found that the axial velocity inside the pore approaches a Poiseuille profile with less than 1.5% deviation after a short entrance distance of half the

pore radius for the pores with l/d > 0.5. This suggests that upstream effects were significant only near the pore opening. Further, once the Poiseuille profile is established inside the pore, the streamline pattern must remain similar for all values of l/d >0.5, therefore the velocity at the exit of the pore is unchanged. The pressure field obtained by the authors showed very good agreement in the far field outside the pores with the solution obtained by Sampson (1891) for a pore with zero thickness. They showed that pressure drop across the orifice has a linear dependence on the aspect ratio and found an expression assuming Poiseuille flow throughout the pore and Sampson's solution outside as follows:

$$\Delta P = \frac{Q\mu}{r^3}\left(\frac{16(l/d)}{\pi} + 3\right) \tag{2.1}$$

The above expression does not account for upstream influence across the orifice opening because a Poiseuille profile is assumed throughout the pore.

Grose (1983) suggests that the orifice discharge coefficient is a product of three coefficients (the viscosity coefficient, C_v, the contraction coefficient, C_c, and the velocity profile coefficient, C_p) such that $C_d = C_c \cdot C_v \cdot C_p$. He used the Navier-Stokes equations to model an orifice and proposed a "viscosity coefficient". At low Reynolds numbers, the contraction coefficient and the velocity coefficient tend to a value of one, resulting in the discharge coefficient being a function of only the viscosity coefficient. He then compares viscosity coefficients with experimentally determined discharge coefficients for Re < 16 and shows excellent agreement between the two. Beyond this range, the viscosity coefficient over-predicts the value of the discharge coefficient, which is most probably due to the contraction coefficient beginning to decrease in value from one, which in turn causes a decrease in the value of the discharge coefficient. In a subsequent paper Grose

(1985), he develops equations for the contraction coefficient (C_c). Using the Navier-Stokes equations with an elliptical surface profile, the contraction coefficient is predicted solely as a function of diameter ratio ($\beta = d/D$). He proposes that for purely inviscid flow ($Re > 10^5$), the effects of the viscous and profile coefficients can be ignored, resulting in $C_d = C_c$. For diameter ratios between 0 and 0.75, comparisons are made between the elliptical equation and modified empirical equations derived from data from Stolz (1975) and Miller (1979), and the ASME-AGA orifice equation with vena contracta taps as presented by Miller (1979). The equations agree quite well up to a diameter ratio of about 0.4, at which point the elliptical equation begins to over-predict the results of the empirical equations. It is suggested that this occurs because the empirical equations do not take into account the fact that the velocity profile coefficient tends to unity as the Reynolds number tends to infinity. For contraction coefficients, the empirical equations diverge from the theory and each other, with only the Miller (1979) equation still moving in the direction suggested by the theory.

During the 1990s, continuous improvements in computer technology led to a greater number of orifice flow problems being solved numerically. Jones and Bajura (1991) developed a numerical solution for laminar, pulsating flow through an orifice with Reynolds numbers ranging from 0.8 to 64 and Strouhal numbers (St) ranging from 10^{-5} to 100, where:

$$St = \frac{2\pi f D}{V} \tag{2.2}$$

where: f = pulsation frequency
D = pipe diameter
V = average velocity in pipe

Two different orifice geometries with diameter ratios (β) of 0.5 and 0.2 were used

in their analysis. The thickness of each orifice was 0.2 times the pipe diameter and each had a 45-degree bevel on the downstream side to a depth of 50 percent. The Navier-Stokes equations were used as the starting point in their analysis, and initial comparisons with steady flow data from Johansen (1930), Tuve and Sprenkle (1933), and Keith (1971) as presented by Coder (1973) showed good agreement with the resulting discharge coefficients. Results from the pulsating analysis were plotted as discharge coefficient vs. time for every 45 degrees, and show that the discharge coefficient initially oscillates around the discharge coefficient that would be expected for steady flow. As the Strouhal number increases (increase in pulsation frequency), both the amplitude of the oscillations and the time-averaged discharge coefficient begins to decrease. By plotting the normalized discharge coefficient (mean discharge coefficient divided by steady flow discharge coefficient) vs. the natural log of the Pulsation Product ($P_p = Re \times St$) it is seen that the normalized discharge coefficient remains fairly constant until $\ln(P_p) = -2.5$. At this point, the discharge coefficient begins to decrease rapidly and becomes 40 percent of the steady flow value at $\ln(P_p) = 2.5$.

Sahin and Ceyhan (1996) used experiments and numerical analysis to examine incompressible flow through orifices with diameter ratios of 0.5 and aspect ratios ranging from 0.0625 to 1. A gear pump was used in their experiments to circulate oil through an orifice at temperatures ranging from 30°C to 50°C with the resulting Reynolds numbers ranging from less than 1 to 150. The numerical analysis was conducted using two-dimensional Navier-Stokes equations for axi-symmetric, viscous, incompressible flow through a square-edged orifice in a circular pipe. The resulting equation for the discharge coefficient is given as:

$$C_d = \frac{1}{2\sqrt{2}}\left(\frac{1}{\beta}\right)^2\left(1-\beta^4\right)^{1/2}\left(\frac{\rho V_{max}^2}{\Delta P}\right)^{1/2}, \qquad (2.3)$$

where V_{max} is the velocity at the centerline of the pipe.

The numerical results were compared with their own experimental results and with those of Nigro et al. (1978), Alvi et al. (1978) and Johansen (1930), and were found to agree within 5%.

Hasegawa et al. (1997) examined several thin orifices ranging from 1 mm to 10 μm in diameter. Experiments were performed with distilled water ($\nu = 1.00\times 10^{-6}$ m^2/s), silicone oils ($\nu = 1.10\times10^{-6}$, 2.22×10^{-6}, and 5.13×10^{-6} m^2/s), and glycerin solutions ($\nu = 1.69\times10^{-6}$, 2.39×10^{-6}, 3.44×10^{-6}, and 5.28×10^{-6} m^2/s) as the working fluids. The resulting pressure drop-flow rate relationship was examined for Reynolds numbers in the range of 1 to 1000. Additionally, numerical analysis was conducted for these same flow conditions. The numerical solution compares quite well for orifices with diameters larger than 65 μm, but under-predicts the pressure drop for smaller orifices. The under-prediction becomes worse as either the orifice diameter or the fluid viscosity decreases. To explain this, the authors examined possible causes such as the material used in construction, burring that occurred in manufacturing, and boundary layer thickness increases due to ionic effects of the liquid. They found that none of these causes could produce the increases in pressure drop that were seen between the experimental data and the numerical solution. It is unclear, however, whether the increase in the length-to-diameter ratio, which increased as the orifice diameter decreased for all orifices, was ever examined as a possible cause by the authors.

Dugdale (1997) mathematically modeled the radial and angular velocity profiles

of a sharp-edged orifice. An experimental apparatus was also constructed to test molasses at flow rates corresponding to Reynolds numbers on the order of 10^{-4}. Two 0.082 mm thick orifice plates were constructed from brass with diameters of 5.1 mm and 2.396 mm respectively. For an applied pressure of 2.121 kPa, an energy dissipation constant (C) was experimentally determined such that:

$$\mathrm{Eu} = 4\pi \mathrm{C}(\mathrm{Re})^{-1} \tag{2.4}$$

These data were compared with the experimental results of Bond (1922) on mixtures of glycerin and water. The energy dissipation constant calculated from Bond (3.21) was within the range $3.17 < C < 3.30$ predicted from their data.

Zhang and Cai (1999) conducted an investigation to examine the pressure drop characteristics of orifices with different profiles and contraction ratios in an application where the orifice is used as an energy dissipater in flood conduits. Their primary concern was to identify a compromise orifice geometry (that is neither sharp-edged nor streamlined) that produces the lowest local pressure drop while achieving the desired energy loss. By minimizing excessive pressure drops across orifices in flood conduits, cavitation and the resulting damage to concrete tunnels and orifices can be reduced or eliminated. A model resembling a flood conduit used in dam construction was fabricated for the testing of the orifices. Orifices with four different diameter ratios ranging from 0.5 to 0.8 were tested with Reynolds numbers ranging from 1.04×10^5 to 2×10^5. The authors also mentioned that non-dimensional energy loss ($k = \Delta h/(V^2/2g)$, where Δh = amount of energy loss, expressed as water head) for any β is larger than that of axisymmetric sudden enlargement, $k(\beta) \geq (1-\beta^2)^2/\beta^4$, and found that for k values between 0.5 and 4, the sloping-approach type orifice worked best. Here k is analogous to the

Euler number.

The concern that cavitation on the downstream side of an orifice could affect the discharge coefficient, or cause damage to the system, also received the attention of researchers. Kim et al. (1997) investigated the effects of cavitation and plate thickness on the orifice discharge coefficient by conducting tests on 3 orifices with diameter ratios of 0.10, 0.15, and 0.33. They found that cavitation occurred for pipe Reynolds numbers ($Re_D = \beta Re$) above 14000 for a β of 0.10, 43000 for a β of 0.15, and 100,000 for a β of 0.33. It was seen that for the three diameter ratios, cavitation did not affect the discharge coefficient for aspect ratios less than or equal to 0.55 over the entire range examined ($4000 < Re < 170{,}000$).

Ramamurthi and Nandakumar (1999) examined the effects of aspect ratio and cavitation on the discharge coefficients of square-edged orifices. Orifices with diameters of 0.3, 0.5, 1.0, and 2.0 mm and aspect ratios ranging from 1 to 50 were tested at flow rates with Reynolds numbers in the range of 2000 to 100,000. They found that for flow conditions exhibiting attached flow, the discharge coefficient was a function of both the aspect ratio and the Reynolds number. When the flows became separated or exhibited cavitation, however, they found that the discharge coefficient became a function of only orifice diameter. In the separated flow region, it was noted that as the orifice diameter decreased, the discharge coefficient increased. It was proposed that effects such as increased wetting of the orifice walls and surface tension-induced pressure play an increasingly important role in the discharge coefficient as orifice diameter decreases. It was also noted that cavitation has the greatest effect on orifices with aspect ratios of approximately 5. It was proposed that this occurs because bubbles formed during

cavitation tend to collapse very near the exit of the orifice causing the greatest disturbance in the flow patterns.

In recent years, studies on flow through constricted geometries have also been conducted by researchers interested in the use of orifices for component cooling. In addition to orifice flow characteristics, these researchers have also studied the effects of two-phase flow conditions and examined how free jets discharging from an orifice are affected by component spacing.

Kiljanski (1993) examined free jets from orifices and proposed that the discharge coefficient can be related to the orifice Reynolds number by the equation: $C_d = B\sqrt{\mathrm{Re}}$, where B is an experimentally determined constant based on the aspect ratio. Four liquids (ethylene glycol [μ= 0.02 kg/m-s], potato syrup [μ= 10 kg/m-s], and two glycerol solutions [μ= 0.15 and 0.40 kg/m-s]) were tested using five different orifices over a flow range of $0.01 < \mathrm{Re} < 500$. Three orifices with aspect ratios of 0.5 and diameters of 2, 3, and 5 mm were used along with two additional 3 mm diameter orifices with aspect ratios of approximately 0 (sharp-edged) and 1.0 respectively. It was shown from plots of C_d versus Reynolds number that for $\mathrm{Re} < 10$, all data followed lines with a slope of approximately 0.5. Additionally, the value for the constant B increased as the aspect ratio increased. For $\mathrm{Re} > 10$, the curves for the different aspect ratios begin to converge, and become one curve near Re = 300. The author suggests that this occurs because of the dominant effects of kinetic energy in this region and that for $\mathrm{Re} > 300$, the aspect ratio no longer affects the discharge coefficient.

Morris and Garimella (1998) extended their previous work on jet impingement heat transfer in 3.18 mm and 6.35 mm diameter orifices (Morris *et al.* 1996) to determine

the length of the separation region in the orifice plate, the pressure losses across the orifice plate, and the flow features in the confinement region using the finite volume code FLUENT (1995). Numerical results were presented for various area ratios (d^2/D^2) and aspect ratios (l/d) for Reynolds numbers in the range of 8500 to 23,000. The authors then compared the numerical results for the 3.18 mm and 6.35 mm diameter orifices with the experimental data from Ward-Smith (1971). The data from Ward-Smith (1971) were correlated to yield three equations for the discharge coefficient that were based on the aspect ratio. The losses predicted numerically by them were within 5% of the empirical correlations in all cases.

Morris et al. (1999) compared the flow fields generated from their numerical simulation with photographs and laser-Doppler velocimetry measurements taken from a test loop constructed by Fitzgerald and Garimella (1997). They found good agreement between the data from the numerical simulation and the experimental data at Re > 8500 but not for Reynolds numbers of 2000 and 4000. They propose that this is due to not fully accounting for the effects of "laminar/semi-turbulent" flow fields in their model.

In a very recent study, Mincks (2002) conducted an experimental study to determine pressure drop characteristics of the viscous fluid through small diameter orifices. The fluid investigated has temperature and pressure dependent properties however at the temperatures ($20 \leq T \leq 50^oC$) investigated in his study, the properties do not changes drastically with the temperature. He noted that pressure drop across orifices can be presented as function of aspect ratio, diameter ratio and Reynolds number and proposed a correlation for non-dimensional pressure drop. More studies at lower temperatures are needed to understand the effect of varying properties of the fluid on the

pressure drop characteristics.

2.2 Compressible Newtonian Flow

Kayser and Shambaugh (1991) investigated compressible flow of gases through small diameter orifices ($0.9 < d < 1.9$ mm) with geometries such as knife-edged, square-edged straight-bore, rounded-entry, and elliptical-entry. For the flows examined, orifice Reynolds numbers ranged from 3,000 to 80,000 and pressure drops ranged from 100 to 350 kPa. They found that for the knife-edged orifice plate, the discharge coefficient correlates poorly with the Reynolds number but correlates quite well with the dimensionless pressure drop $(P_{in} - P_{out})/(P_{crit} - P_{out})$, and that the discharge coefficient showed virtually no dependence on fluid temperature or orifice diameter. For the straight bore orifices, they found that the discharge coefficient was a function of both the pressure ratio (P_{in}/P_{out}) and the aspect ratio and that as the aspect ratio increased, so did the discharge coefficient. Finally, it was observed that both the round and elliptical-nozzles performed similarly, and that they had the highest discharge coefficient of any of the elements tested.

More recently Gan and Riffat (1997) constructed an experimental apparatus to measure the pressure drop across an orifice plate in a square duct using air as the working fluid. They also experimented with a perforated plate having the same area reduction as the orifice plate. The plates were 2 mm thick with the orifice plate having an orifice diameter of 0.239 m, and the perforated plate having 145, uniformly spaced, 20 mm diameter holes. Data for both plates were compared for Reynolds numbers ranging from 1.6×10^5 to 3.7×10^5 and showed that the orifice plate had a lower pressure drop than the perforated plate, which contrasted earlier findings of Idelchik et al (1986). A CFD

analysis using FLUENT (1995) was conducted to predict the pressure loss coefficients (Euler numbers) of the orifice plate and the perforated plate with the results being within 8% of the experimental data. The CFD program was then used to predict discharge coefficients for orifice plates of varying thicknesses. The results show that for a constant free area ratio (area of orifice/area of duct), the pressure loss coefficient decreases as the aspect ratio increases up to an aspect ratio of approximately 1.5. As the aspect ratio increases beyond this value, the pressure loss coefficient value shows a small but slightly increasing variation, which is similar to the results of Stichlmair and Mersmann (1978) for Reynolds numbers of 400 to 10^6.

Emmons (1997) showed that the venting that occurs when holes are created during a building fire can be modeled as a nozzle or an orifice. He proposed that the discharge coefficient (C_d) is comprised of two parts: C_μ which represents viscous effects and C_{ve} which corrects for the flow area change due to the vena contracta, such that $C_d = C_\mu \cdot C_{ve}$. He also showed that at low Reynolds numbers, C_μ tends towards zero and C_{ve} tends towards unity as is supported by data from Heskestad and Spaulding (1991) and Tan and Jaluria (1992) over the range $800 < Re < 4000$. Mathematical equations were then developed to determine the mass flow rate through vertical and inclined vents based on C_d, and through the horizontal orifice based on the Froude Number. Based on these equations, Emmons (1997) then determined a theoretical Froude number equation for conditions where the flow is due only to differences in density. He found good agreement between his equation and data from Heskestad and Spaulding (1991) and Epstein and Kenton (1989), but not with those from Tan and Jaluria (1992).

2.3 Non-Newtonian Flow

Though fluid rheology and non-Newtonian fluid flow are areas of considerable research and industrial interest, the available literature related to orifice flow for such fluids is limited. Instead, the focus of attention in the research on non-Newtonian flow is typically the rheological properties of the fluid.

Steffe and Salas-Valerio (1990) conducted experiments to study the effect of the rheological properties of non-Newtonian (power law) fluids on C_d. The test fluids in their study were 5%, 7.5% and 10% corn starch solutions. The orifice discharge coefficient was found to be in the range of 0-0.7 and depended on the orifice diameter, fluid velocity and rheological properties (consistency and power law index). At lower velocities, C_d increases with increasing velocity but tends to assume a constant value at high velocities. Shear rates in their study were in the range of 20-250 s^{-1}. They found that C_d decreases as the consistency coefficient increases. They also proposed that C_d may be expressed as an exponential function of the generalized Reynolds number.

Sorab et al. (1993) examined the effect of temperature and shear rate on the viscosity of multigrade lubricant oils. They extended the Carreau viscosity function (Bird *et al.* 1987) and also accounted for the temperature dependence, which resulted in improved prediction of viscosity for a wide range of oil formulations. The resulting expression can determine the viscosity parameters for shear thinning fluids in terms of measured viscosities at some reference state. The non-Newtonian viscosity is then expressed as a function of viscosities of the first Newtonian region (low shear rates) and those of the second Newtonian region (power law, high shear rates). Their method can be used even at shear rates greater than 10^6 s^{-1}.

Recently Samanta et al. (1999) investigated pressure drops resulting from the flow of a mixture of a gas and a non-Newtonian pseudoplastic liquid through orifices of varying diameter. An apparatus was constructed to measure this pressure drop using air as the gas, and sodium salt of carboxy methyl cellulose (SCMC) as the non-Newtonian liquid at temperatures of 31°C ± 1.5°C. Three orifice plates were used with diameters of 5.9 mm, 7.6 mm, and 9.0 mm, and diameter ratios of 0.4646, 0.5984, and 0.7087 respectively. Single-phase data were collected for both water and the sodium salt mixtures, with pressure drops ranging from approximately 1 kPa to 26 kPa. Two-phase data for the air-sodium salt mixture were also collected in this same pressure range with liquid Reynolds numbers ranging from 45 to 2200 and gas Reynolds numbers ranging from 230 to 2200. From these data, formulae were presented for both the liquid-only and the gas-liquid pressure drops in terms of the non-dimensional Euler number. The liquid-only Euler number was represented as a function of Reynolds number and contraction ratio as shown in Equation (2.5), while the two-phase Euler number was shown to be a function of the liquid Reynolds number, the gas Reynolds number, the contraction ratio, and the fluid properties of the liquid as shown in Equation (2.6).

$$Eu_l = 1.202\,Re_l^{-0.048\pm0.044}\left(\frac{d}{D}\right)^{-4.380\pm0.248} \tag{2.5}$$

$$Eu_{tp} = Eu_l\left[1 + 0.003\,Re_l^{-0.536\pm0.063}\,Re_g^{0.797\pm0.060}\left(\frac{g\mu_{eff}^4}{\rho_l\sigma_l^3}\right)^{-0.125\pm0.021}\left(\frac{d}{D}\right)^{0.205\pm0.166}\right] \tag{2.6}$$

McNeil et al. (1999), interested in modeling small pressure relief valves, constructed a test facility to measure the flow rate, pressure drop, and momentum effects in a nozzle and an orifice. The nozzle and orifice both had a diameter ratio (β) of 0.491

and tests were conducted with Reynolds numbers ranging from 40 to around 400 using a solution of Luviskol K90 in water as the working fluid. The momentum results were determined from the impingement of the fluid onto a balance plate as it was discharged from the test loop into a catch tank. The data from the momentum test were used to calculate the actual momentum correction factor which is the reciprocal of the contraction coefficient (C_c). The velocity coefficient (C_v) was found by using the equation for the discharge coefficient ($C_d = C_c \cdot C_v$) from Massey (1975). The authors concluded that the contraction coefficient tends to unity at low Reynolds numbers, and that the discharge coefficient is dependent on both the Reynolds number and the flow geometry.

Valle et al. (2000) constructed a nozzle flow meter that used orifices with 45° converging and diverging sections and diameters ranging from 0.6 to 3.0 mm. The flow meter was initially tested with water and oil (μ = 0.08 and 1.62 kg/m-s), at room temperature (≈25°C), and flow rates ranging from 2.0 to 75 ml/s. The results showed the dependence of Euler number on Reynolds number for the two fluids. The authors concluded that "At low Reynolds numbers, the flow is purely laminar and the pressure drop increases proportionally with the viscosity. At high Reynolds numbers, the flow is dominated by inertia and the pressure drop becomes independent of viscosity." The flow meter was then used to investigate the extensional properties of a Boger (1993) fluid and a Newtonian fluid with suspended solids. A Boger fluid is a fluid that exhibits significant elastic properties while the viscosity remains independent of shear rate (Valle *et al.* 2000). The authors showed that it was possible to determine the extensional viscosity (μ_e) of visceolastic fluids and suspensions from the following equation:

$$\mu_e = 3\mu R \tag{2.7}$$

Where: 3μ = extensional viscosity of a Newtonian fluid.
R = the vertical shift between the elastic fluid data and the Newtonian fluid data on the Eu vs. Re plot.

They note that the extensional viscosity of the fluids was found to be about 45 times that of the shear viscosity, which was similar to the findings of Sridhar (1990) for a different Boger fluid.

2.4 Need for Further Investigation

A summary of the above discussed literature is presented in Table 2.1. It is clear from the literature review presented in the previous sections that considerable work has been done in the area of orifices, but deficiencies still exist. Here, the need for further investigation is discussed based on each of the parameters of interest in orifice flow.

The majority of the work reviewed has been dedicated to the study of incompressible flow through orifices with $0.2 < \beta < 0.8$ as found in orifice flow meters where the flow regime is turbulent. There are few studies for orifices of $\beta < 0.1$. Lichtarowicz et al. (1965) presented data from Morgan (1963) in which two sets of orifices were used with $\beta = 0.044$ and $\beta = 0.071$, respectively. The first set had aspect ratios of 0.5 and 2.0, while the second set had aspect ratios of 1.0 and 4.0. Morgan's data are limited to $Re < 100$, but show that for this region, an increase in the aspect ratio results in a decrease in C_d for similar flow rates. However, the flow remains laminar for $Re > 100$, and the limited data range of Morgan cannot be applied with confidence for laminar flows at higher Re values, as is the case here for the highly viscous fluid under consideration.

Most of the research on square-edged orifices with $\beta < 0.1$ (or $d < 1$ mm) and $Re < 1000$, concentrates on the coefficient of discharge for orifice flow. Few researchers

demonstrate the effects of varying aspect ratio on C_d and non-dimensional pressure drop (Euler number). Hasegawa et al. (1997) experimented with very small orifices and showed that as the diameter of the orifice decreases to less than 0.035 mm, the pressure drop is higher than the predicted values. However, since all of the orifices of diameters less than 0.109 mm that they tested were of the same thickness, it is unclear as to whether the resulting increase in aspect ratio was taken into account as the orifice diameter decreased. Morris and Garimella (1998) have also shown that aspect ratio plays an important part in determining C_d for Reynolds number in the turbulent regime. However, their expressions for C_d at different aspect ratios are valid for $\beta \leq 0.0635$, and only for the turbulent region.

In summary, it can be seen that there still exists a need to understand flow through small diameter, squared-edged orifices over a wide range of Reynolds numbers. Also, the effect of aspect ratio on the orifice flow characteristics for these geometries should be given more attention. It has also been suggested that for very small diameter orifices, a fourth, as yet unidentified, parameter may be required to further explain the increased pressure drop seen in these orifices (Hasegawa *et al.* 1997).

Apart from geometry and Reynolds number, the fluid investigated in this study is highly viscous and exhibits a significant dependence of properties on temperature and pressure. This interaction of geometries, flow conditions and temperature (through viscosity) is further complicated by partial non-Newtonian behavior of the fluid, which is not understood well.

Therefore, this study addresses the interaction of geometries, flow conditions and fluid properties in determining the flow and pressure drop characteristics of orifice flow.

The orifices investigated have diameter ratios of 0.023, 0.044 and 0.137, and cover aspect ratios in the range 0.33 to 6. This study also aims at understanding the orifice flow characteristics over a large range of Reynolds numbers.

Table 2.1 Summary of the Literature Review

Author	Geometry	Orifice Diameter (mm)	Diameter Ratios (β)	Aspect Ratio l/D	Re Range	Fluids $\nu = m^2/s$ $\mu = kg/m\text{-}s$	Technique	Data Presentation Format	Findings
Incompressible Newtonian Flow									
Johansen (1930)	Square-Edged with 45° Back Cut		Visualization: 0.1, 0.25, 0.5, 0.75 Pressure Drop: 0.209, 0.401, 0.509, 0.794	Thin ($\leq$ 0.083)	<1 to 25,000	Water, Castor oil ($\nu = 1.21 \times 10^{-3}$ at 18°C), Mineral lubricating oil ($\nu = 1.14 \times 10^{-4}$ at 18°C)	E, V	Photos from dye test. Plots of C_d versus square root of Re for experiments.	Changes in the C_d can be correlated to changes in flow patterns as observed by dye test.
Tuve and Sprenkle (1933)	Square-Edged with 45° Back Cut		0.2 to 0.8	Thin ($\leq$ 0.04)	4 to 40,000	Water, Heavy Motor Oil ($\nu = 1.62 \times 10^{-3}$), Light Motor Oil, Light Paraffin Oil	E	Plots of C_d versus log Re for their data, Plots of C_d vs. β (constant Re) comparison with other data	Found close agreement for Re > 150 and β < 0.5 with previous work.
Medaugh and Johnson (1940)	Square-Edged	6.35, 12.7, 19.1, 25.4, 50.8		$\leq$ 1.0	30,000 to 350,000	Water	E	Plots of C_d versus pressure drop, plot of C_d vs Re for high Re, table of C_d and DP values	Compared to Smith and Walker (1923), Judd and King (1906), Bilton (1908) and H. Smith (1886). good agreement with H. Smith (1886) and Strickland (1909)
Lichtarowicz et al. (1965)	Square-Edged		0.044, 0.054, 0.071, 0.251, 0.252	0.5, 1.0, 2.0, 4.0, 10.0	0.5 to 50,000	Water, Water-Glycerin Mixture, Oil (various viscosities - not given)	R	Plots of C_d vs Re for various aspect ratios.	Compared experimental work done by Morgan (1963), James (1961) and Sanderson (1962) with previous work. Recommend changes to C_d equations suggested by Nakayama (1961) and Asihmin (1961)

Table 2.1 Summary of the Literature Review (Continued)

Author	Geometry	Orifice Diameter (mm)	Diameter Ratios (β)	Aspect Ratio l/D	Re Range	Fluids $\nu = m^2/s$ $\mu = kg/m\text{-}s$	Technique	Data Presentation Format	Findings
Alvi et al. (1978)	Sharp-Edged, Quadrant-Edged and Long Radius Flow Nozzles		0.2, 0.4, 0.6, and 0.8 (Quadrants: r/d = 0.08, 0.125, 0.18, 0.25)	Not Given	1 to 10,000	4 oils were used (ν = 1.05 x 10^{-5}, 2.0 x 10^{-5}, 1 x 10^{-4}, and 3.5 x 10^{-4} at 30°C)	E	Plots of Eu vs. Re for different Orifices based on diameter Ratios.	Compared well with Zampaglione (1969) and Lakshmana Rao and Sridharan (1972). Determined that quadrant-edge orifices act sharp at low Re and like nozzles at high Re.
Miller (1979)	Sharp-Edged, Quadrant-Edged and Long Radius Flow Nozzles		0.2 to 0.7	Not Given	50,000 to 4,000,000	Water	A	Percent deviation vs Re	Laboratory data are compared with numbers predicted by ASME-AGA and Stoltz equations to conclude that error can be reduced with better measurement.
Dagan et al. (1982)	Pore of finite length			0.25 to 2	Creeping flow		A	Plots of velocity profiles and pressure fields at various locations	Related pressure drop across orifice (pores) for very small Reynolds number. Pressure field agrees well in the far space outside the pore with previous study of Sampson (1891)
Grose (1983)	Sharp-Edged				Less than 1		A	Plot of C_d vs Re for experimental data and predicted values from equations.	Predicted values compare quite well with data from previous investigators for Re < 16. C_d is proportional to square root of Re in this range.

Table 2.1 Summary of the Literature Review (Continued)

Author	Geometry	Orifice Diameter (mm)	Diameter Ratios (β)	Aspect Ratio l/D	Re Range	Fluids $\nu = m^2/s$ $\mu = kg/m\text{-}s$	Technique	Data Presentation Format	Findings
Grose (1985)	Sharp-Edged		< 0.7		> 100,000		A	Plots of C_d vs β for Grose's equation, the Stoltz (1975), ASME (1971)-AGA (1955) equation, Miller's equation (1979), and available data	The elliptical equation compares well with data from Flugge (1960) and predictions from other equations for beta < 0.4 but over predicts above this. Postulates that it is due to profile effects.
Jones and Bajura (1991)	Square-Edged with 45° Back Cut		0.2 and 0.5	Thin ($\leq$ 0.25)	0.8 to 64		C	Tabular data compared with previous research. Plots of C_d vs Strouhal number and streamline Visualizations	Steady flow data predictions agreed fairly well with experimental data for this range. $St = \frac{2\pi D_{pipe}}{V_{pipe}}$
Sahin and Ceyhan (1996)	Square-Edged		0.5	0.0625, 0.125, 0.25, 0.5, and 1	0 to 150	Oil (viscosities were not given)	E, C	Plot of C_d vs square root of Re for their numerical and experimental data and data from Alvi (1978) and Johansen (1930)	Found that as Re increases in this range, the upstream separated flow region shrinks and downstream lengthens. Theory and experiments agree well.
Dugdale (1997)	Square-Edged	2.396 and 5.100		Thin ($\leq$ 0.034)	on order of 10^{-4}	Molasses (μ = 14 to 19.7)	E, A	Small table of data giving the flow rate, energy dissipation constant (C), temperature, and viscosity	Compares well with work by Bond (1922) but is 5 to 10% higher than predicted by theory.

Table 2.1 Summary of the Literature Review (Continued)

Author	Geometry	Orifice Diameter (mm)	Diameter Ratios (β)	Aspect Ratio l/D	Re Range	Fluids $\nu = m^2/s$ $\mu = kg/m\text{-}s$	Technique	Data Presentation Format	Findings
Hasegawa et al. (1997)	Square-Edged	0.01 to 1.0		Not controlled but ranges from 0.051 up to 1.14	1 to 1000	Distilled water, glycerin solutions (ν = 1.7 x 10^{-6}, 2.4 x 10^{-6}, 3.4 x 10^{-6}, 5.3 x 10^{-6}), and silicon oils (ν = 1.1 x 10^{-6}, 2.2 x 10^{-6}, 5.1 x 10^{-6})	E, C	Plots of Eu vs. Re for different orifice configurations and numerical solution. Also shows departure from Stokes flow occurring at approximately Re = 10	As the diameter of the orifice decreases below 0.065 mm, the numerical solution under predicts the pressure drop that occurs. Below this value, the under prediction becomes worse as either the orifice diameter or the fluid viscosity decreases.
Zhang and Cai (1999)	Square-Edged, Sharp-Edged, Stream-Lined, Quadrant-Edged and Sloping Approach	51.0, 61.2, 70.4, and 81.6	0.5, 0.6, 0.69, and 0.8	Not Given	104,000 to 200,000	Water	E	Dimensionless wall pressure vs position in pipe, dimensionless pressure drop vs β	Determined that for Eu between 0.5 and 4, the sloping approach orifice geometry provides the highest pressure drop for the same downstream minima as compared to the other orifices.
Kim et al. (1997)	Square-Edged with 45° Back Cut	10, 15, and 33	0.1, 0.15, 0.33	0.21 to 0.7	4000 to 100,000 based on pipe diameter	Water	E	C_d vs. Re, Cavitation in dB vs Re	Determined that cavitation did occur in orifices and that C_d was only affected for beta = 0.1 and l/d = 0.7. Cavitation did not affect C_d for all other cases.
Ramamurthi and Nandakumar (1999)	Square-Edged	0.3, 0.5, 1.0, and 2.0	0.03, 0.05, 0.1, and 0.2	1 to 50	2000 to 100,000	Water	E, V	C_d vs. Re plots for different geometries	Determined that orifices with aspect ratios of 5 are most affected by cavitation.

Table 2.1 Summary of the Literature Review (Continued)

Author	Geometry	Orifice Diameter (mm)	Diameter Ratios (β)	Aspect Ratio l/D	Re Range	Fluids $\nu = m^2/s$ $\mu = kg/m\text{-}s$	Technique	Data Presentation Format	Findings
Kiljanski (1993)	Sharp-Edged	2, 3, and 5	0.053, 0.079, and 0.132	0 and 1.0 for 3 mm orifice. 0.5 for others	10^{-2} to 500	Ethylene Glycol (μ = 0.02), Glycerol Solutions (μ = 0.15, 0.40), Potato Syrup (μ = 10)	E	C_d vs Re plots and tabular data for all data points	Aspect ratio only affects C_d for Re < 300.
Morris and Garimella (1998)	square-edged	3.18 and 6.35		1 to 6	8500 to 23,000		C (FLUENT)	Plot of C_d vs aspect ratio, tabular data for pressure drop computed from equations and experimental data	The authors re-correlated the experimental data from Ward-Smith (1971) to develop C_d expressions that were found to agree with numerical predictions to within 5%
Morris et al. (1999)	square-edged	3.18 and 6.35			2000 to 23,000		E, V, C (FLUENT)	Velocity profiles for various arrangements	Experimental data agreed well with numerical simulation for Re > 8500, but not at 4000 or 2000. Postulated that this was due to not accounting to laminar/semi-turbulent flow fields
Mincks (2002)	Sharp-edged	0.5, 1 and 3	0.023, 0.044 and 0.137	0.33, 0.66, 1, 2, 4 and 6	8 to 7285	Viscous hydraulic oil (μ = 0.028 to 0.135 kg/m-s) in the temperature range of 20 < T < 50^{o}C	E	Eu vs Re plots	Eu increases with l/d at smaller Re while influence of l/d is not significant at higher Re. Developed a model to predict Eu for a range of orifice geometries.

Table 2.1 Summary of the Literature Review (Continued)

Author	Geometry	Orifice Diameter (mm)	Diameter Ratios (β)	Aspect Ratio l/D	Re Range	Fluids $\nu = m^2/s$ $\mu = kg/m\text{-}s$	Technique	Data Presentation Format	Findings
Compressible Newtonian Flow									
Kayser and Shambaugh (1991)	Sharp-Edged, Square-Edged, Quadrant-Edged, and Elliptical-Entry	0.9 to 1.9		0 to 3.56	3000 to 80,000	Air, CO2, Argon, Helium, He mixes	E	C_d vs pressure ratio and C_d vs. Re	Round and elliptical nozzles perform best. Knife edge does not correlate well with Re
Gan and Riffat (1997)	Square-Edged Orifice and Multi-Holed Plate	145.0 and 239.0	0.71		160,000 to 370,000	Air	E, C (FLUENT)	Pressure ratio vs position in plate, Eu vs. Re, Eu vs l/d	A perforated plate has a higher pressure drop than an orifice with similar flow area. The pressure loss coefficient (Eu) drops as aspect ratio increases to 1.5, then increases slowly
Emmons (1997)	Round Holes					Air	A	Plot of C_d vs Re for experimental data and predicted values from equations.	Determined equations for mass flow rate through holes based on C_d and Froude number. Found good agreement with data from Heskestad and Spaulding (1991) and Epstein and Kenton (1989) but not well with Tan and Jaluria (1992)
Non-Newtonian Flow									
Steffe and Salas-Valerio (1990)	Hole in a pipe	3.18, 4.76 and 78.4		Not given	Up to 2300; Shear rate from 20 to 250 s^{-1}	5, 7.5 and 10% corn starch solutions	E	Plot of C_d vs generalized Re and predicted values from correlation	C_d varies from 0 to 0.7 for power law fluids. C_d decreases as consistency coefficient increases

Table 2.1 Summary of the Literature Review (Continued)

Author	Geometry	Orifice Diameter (mm)	Diameter Ratios (β)	Aspect Ratio l/D	Re Range	Fluids $\nu = m^2/s$ $\mu = kg/m\text{-}s$	Technique	Data Presentation Format	Findings
Sorab et al. (1993)						Multi-grade lubricant oils	A	Viscosity-shear rate- Temperature surface plot	Extended Carreau viscosity function to include the effect of temperature.
Samanta et al. (1999)	Square-Edged		0.4646, 0.5984, and 0.7087		liquid: $45 < Re < 2200$ gas: $230 < Re < 2200$	Sodium salt of Carboxy methyl cellulose	E	DP vs. volumetric flow rate, pressure vs position	Presented Eu equations for liquid only and two-phase conditions. The liquid for this case is non-Newtonian.
McNeil et al. (1999)	Sharp-Edged, Nozzle		0.491	Not Given	40 to 400	Water and Solutions of Luviskol K90 in Water	E	Flow coefficient vs Re, Friction factor vs Re, C_d vs Re	Flow coefficients are dependent on Re and flow geometry at low Re. The contraction coefficient tends to unity as Re goes to 0.
Valle et al. (2000)	45° Bevel on inlet and outlet	0.6 to 3.0		Not Given	< 1 to 100,000	Water, Oil (μ = 0.08 ,1.62), Corn Syrup	E, C (POLY2D)	Plots of Eu vs Re for Newtonian fluids, Boger fluid, and suspension fluids.	Shows that it is possible to determine the extensional viscosity of visceolastic fluids and suspensions. $\mu_e = 3\mu R$ where R is shift in plot and 3μ is the extensional viscosity of a Newtonian fluid by the Trouton relation.

Note: The following abbreviations are used: A - Analytical Approach, C - Computational Methods, E - Experimental Investigation, V - Visualization

3. TEST FACILITY AND EXPERIMENTATION

This chapter discusses the overall test facility and the components within the facility. The original test facility was designed and developed by Mincks (2002) who investigated the pressure drop characteristics of the orifices under consideration for the temperature range of $20 \leq T \leq 50^{o}C$. Several significant modifications were made to that facility to enable testing at the desired test conditions.

3.1 Test Loop

The test facility used for conducting the experiments in this study is shown in Figure 3.1. The corresponding schematic of this test facility is shown in Figure 3.2. The hydraulic fluid was circulated around the test facility using a triplex plunger pump (Cat Pumps Model #660), capable of delivering a flow rate of 38 L/min at a maximum discharge pressure of 21.1 MPa. This pump is belt driven by an electric motor and can be configured to produce lower flow rates and pressures by changing the pulley sizes on the motor and pump. To obtain the desired flow rates, a 10 hp motor was chosen, which delivered a nominal flow rate of 34.2 L/min at a discharge pressure of 11.3 MPa. The pump head is constructed of bronze and contains the suction and discharge valve assemblies. The ceramic plungers use Viton seals that are resistant to oil.

System pressure was controlled by a backpressure control valve located at the discharge side of the pump and a test section bypass valve. The backpressure control method was used for system pressures > 800 kPa because this is the minimum discharge

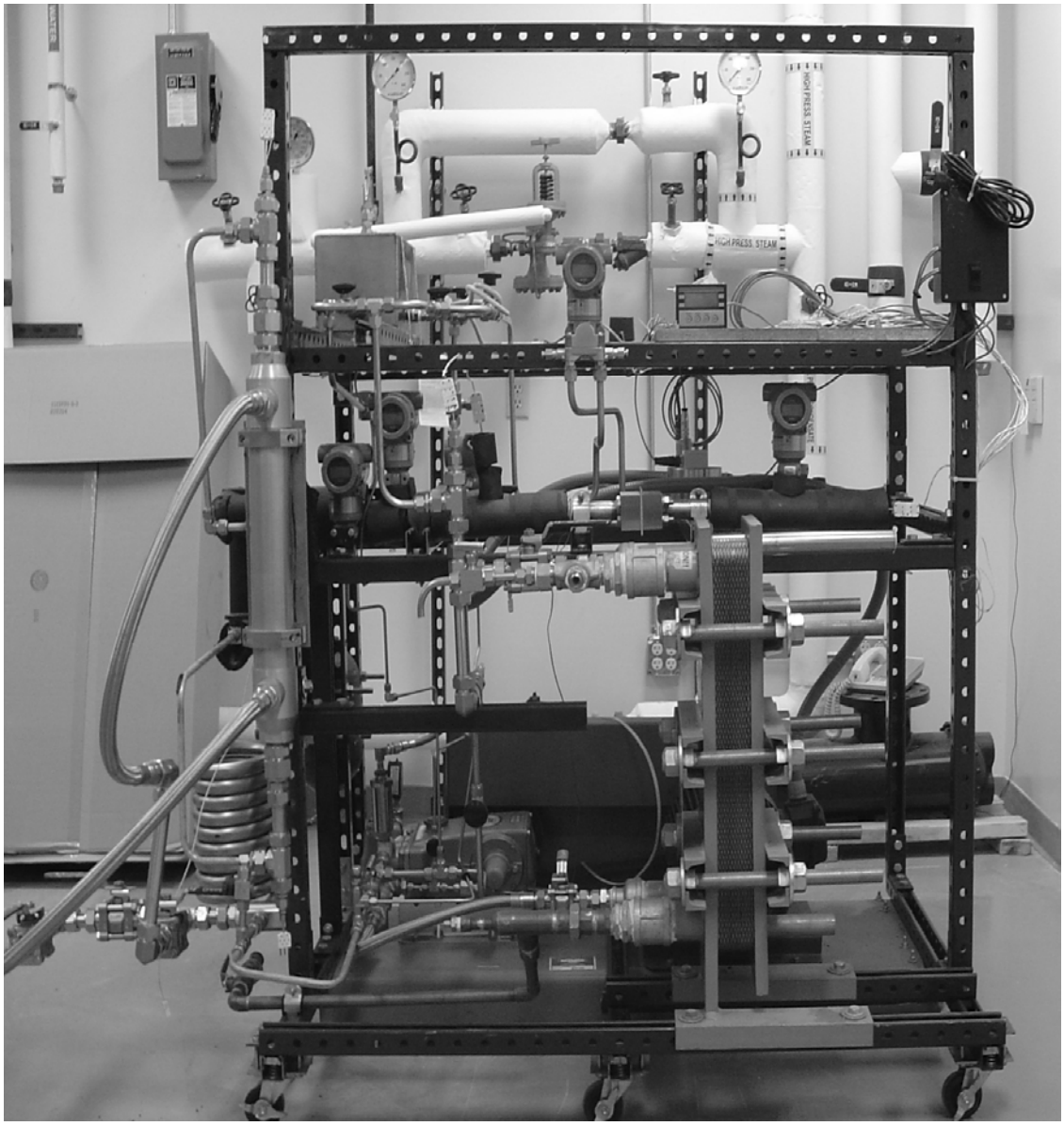

Figure 3.1 Photograph of Test Loop

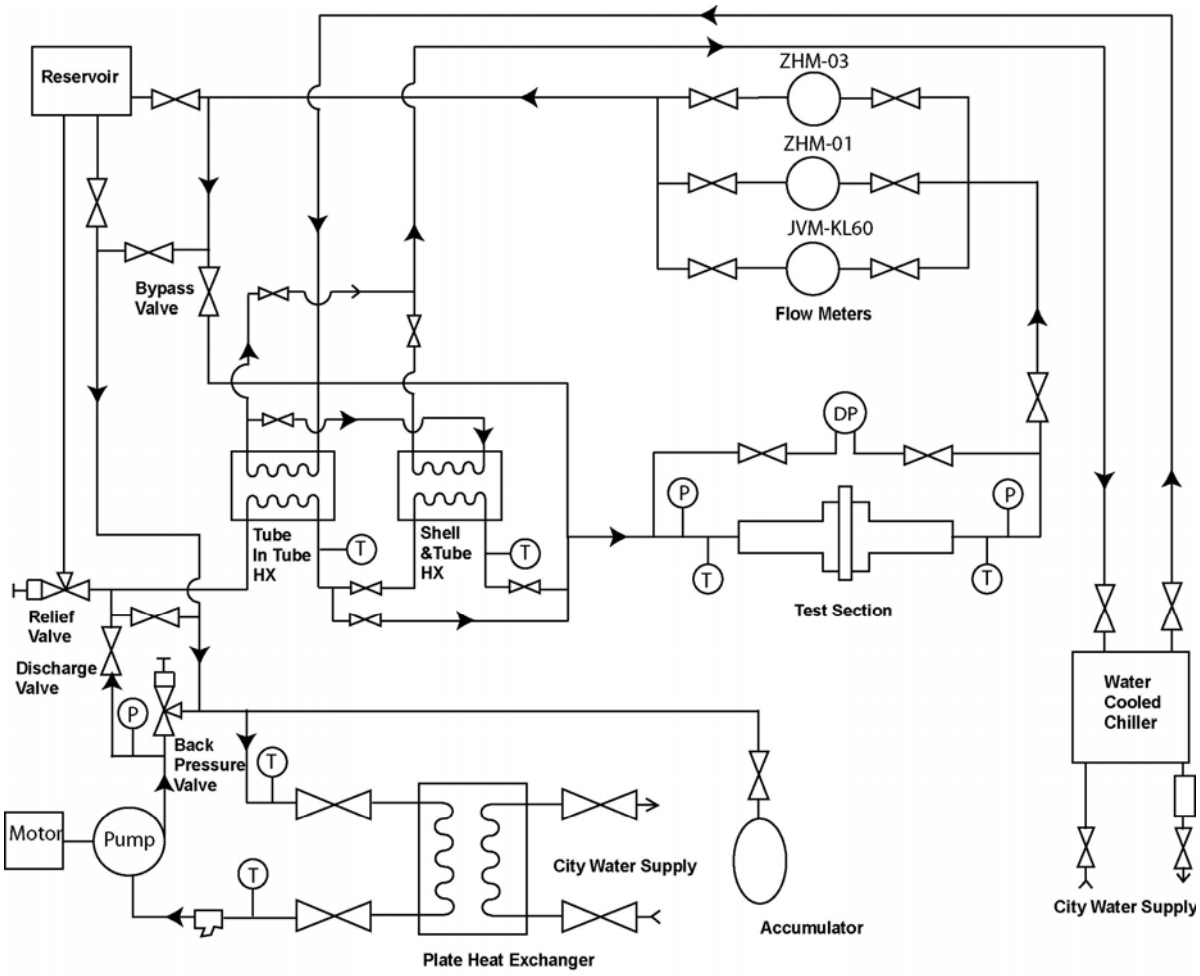

Figure 3.2 Test Loop Schematic

pressure for the pump. For testing at lower system pressures, the test section bypass valve was opened to enable bypassing a desired amount of liquid flow around the test section, with the balance flowing through the test section. This combination of back pressure and bypass valve control allowed testing over a wide range of flow rates. In addition to the minimum discharge pressure requirement, the Cat pump also required a minimum suction pressure of 170 kPa. A 45 cubic inch accumulator manufactured by

Accumulators, Inc. (Model #AM4531003) was installed on the suction side of the pump to meet this requirement. With the loop shut down, the accumulator was pressurized to 500 kPa, which was the maximum pressure required to maintain the 170 kPa at the pump suction during loop operation.

An 8.7 liter (2.3 gallon) stainless steel reservoir was connected to the loop on the suction side of the pump. Because this reservoir was at the highest point in the loop, besides acting as an oil reserve for the system, it also provided an easy location for adding additional oil to the test loop. Also, the reservoir could be pressurized with nitrogen, typically to a pressure of 400 kPa, which was useful for two reasons. First it allowed for filling the accumulator with the proper amount of oil. Second, the loop was configured to operate with the reservoir inline after it was opened for maintenance, such as changing the orifice plate. This allowed any foreign material that may have been left in the loop to collect and settle out in the reservoir. Under normal operation, the reservoir was isolated from the test loop and flow was bypassed around it.

System temperature was maintained by a Tranter Inc. (Model #UX-016-UJ-21) plate heat exchanger located on the suction side of the pump. Cold water required for heat rejection was supplied to the heat exchanger from a city water line. To eliminate the effect of city water line pressure variations on the cold water flow rate, it was first supplied to an open 55 gallon tank with a drain and an overflow. This helped maintain a constant inlet pressure to the Little Giant (Model #977458) magnetic drive pump, which supplied water from the tank to the heat exchanger.

3.1.1 Achievement of Low-Temperature Conditions

Tests in this study were conducted at temperatures as low as -30°C. These extreme low temperatures were achieved using two heat exchangers in the test facility. This subsection details the arrangement and operation of the heat exchangers, and the challenges faced in obtaining extremely low temperatures with the highly viscous fluid ($0.170 < \mu_{ge} < 9.589$ kg/m-s for $10 \geq T \geq -30$°C).

A shell-and-tube heat exchanger (Exergy Inc., Model #00677-3), with 253 tubes of 3.2 mm (0.125 in.) outer diameter, 0.32 mm (0.012 in.) wall thickness, and a length of 508 mm (20 in.) in a 76 mm (3 in.) outer diameter shell, was installed upstream of the test section. This heat exchanger cooled the test fluid to the desired low temperature before it entered the test section. The test fluid flowed through the tube-side while cold fluid (Dow Chemical Syltherm HF) from a dedicated chiller flowed through the shell side in a counterflow orientation. A Mydax chiller (Model #1VL72W) provided the required heat exchange fluid (Syltherm HF) for this heat exchanger. The chiller, which uses R-507 as the refrigerant, has a cooling capacity of 7 kW (2 tons) at -50°C. This heat exchanger was used to conduct experiments for cases with a differential pressure of up to 3000 kPa (435 psi) (and no higher) for the temperature range of $-25 < T < 10$°C. The upper limit on the differential pressure was due to the maximum tube-side pressure limit of 5171 kPa (750 psi) on the shell-and-tube heat exchanger. Accounting for the pressure drop through the heat exchanger itself, the pressure drop in the orifice, and the pressure drop between the orifice outlet and the pump inlet (at which the pressure must be non-negative) the maximum absolute pressure upstream of the test section was always considerably less than 5171 kPa (750 psi). For a representative case with an orifice differential pressure of

30 bar at -10°C across the 1 mm diameter, 1 mm thickness orifice, the flow rate was 3.682×10^{-5} m^3/s (0.583 gpm). At this flow rate, losses in the plumbing from the outlet of the test section to the pump inlet corresponding to an equivalent length of approximately 3.8 m (150 in) are ~1380 kPa (200 psi). The losses in the plumbing from pump outlet to the shell-and-tube heat exchanger corresponding to an equivalent of 0.635 m (25 in.) are ~205 kPa (30 psi). The pressure drop in the shell-and-tube heat exchanger is about 99 kPa (15 psi). Finally, the losses in the plumbing of an equivalent length of 1.27 m (50 in.) from the shell-and-tube heat exchanger outlet to the test section inlet are about 480 kPa (70 psi). Thus, with the above-mentioned pressure of 5171 kPa (750 psi) at the pump discharge, the test section inlet pressure is approximately 4378 kPa (635 psi). Accounting for the losses downstream of the test section of 1380 kPa (200 psi), the maximum differential pressure that can be achieved with this configuration for this test section is 3000 kPa (435 psi). Allowable test conditions for the other orifices were similarly established based on the allowable shell-and-tube heat exchanger pressure and the respective losses.

To address this high pressure limitation on the shell-and-tube heat exchanger, an additional 5.9 m long tube-in-tube heat exchanger (Exergy Inc., Model #00528), with a high pressure limit of 31,025 kPa (4500 psi) for the temperature range of $-100 < T < 100$°C, was installed upstream of the shell-and-tube heat exchanger. The inner tube of this heat exchanger has an outer diameter of 12.7 mm (0.5 in.) and a wall thickness of 1.65 mm (0.065 in.), while the outer tube has a diameter of 25.4 mm (1 in.) and a wall thickness of 1.65 mm (0.065 in.). Provisions were made so that the tube-in-tube heat exchanger could be used alone, as well as in series with the shell-and-tube heat

exchanger. This improved the test capabilities in two ways. First, it was possible to go to higher differential pressures (up to 5000 kPa) across the orifice at relatively warm temperatures (10^{o}C and 0^{o}C) where only the tube-in-tube heat exchanger was sufficient to provide the desired cooling. Second, simultaneous use of both the heat exchangers extended the lower temperature that could be achieved down to -30^{o}C (1 mm diameter orifices).

It should be noted that the tube-in-tube heat exchanger has a much higher pressure operating limit, but because of the flow of the oil through only one 12.7 mm tube, incurs larger pressure drops than those of the shell-and-tube heat exchanger. Thus, the additional pressure capability provided by the tube-in-tube heat exchanger is not as large as the difference between the operating pressure limitations of the two heat exchangers would indicate. For example, at a flow rate of 3.682×10^{-5} m^3/s (0.583 gpm) used in the above illustration, the pressure drop through the tube-in-tube heat exchanger was approximately 1585 kPa (230 psi), whereas the corresponding pressure drop through the shell-and-tube heat exchanger was about 99 kPa (15 psi.) It should also be noted that at the higher differential pressure cases, the plumbing losses also increase proportionately, leading to an additional restriction on the differential pressure capabilities offered by the tube-in-tube heat exchanger. These plumbing losses were particularly large at the lower temperatures ($T \leq -20^{o}$C) because of the sharp increase in viscosity, which limited the possible combinations of low temperature, high differential pressure cases.

3.2 Test Section and Orifices

Figure 3.3 shows a test section that consists of an orifice plate mounted between two flanges. The flanges were manufactured by the Anchor Flange Company and mate to the orifice plate using an o-ring seal. The flanges were supplied with 1" NPT female pipe threads machined into the body of the flange. Two one-inch by six-inch long, schedule 160, 316L, stainless steel pipe nipples were threaded into the flanges. The pipe nipples were machined to fit flush with the orifice side of the flange when fully threaded into place.

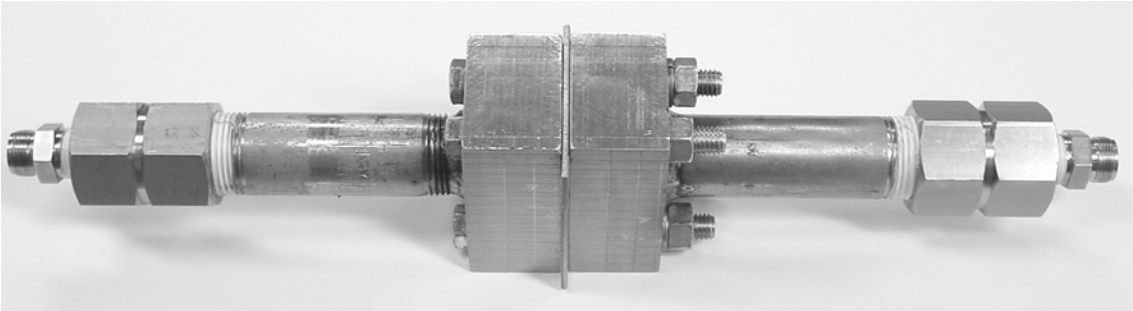

Figure 3.3 Photograph of Test Section (Mincks 2002)

Figure 3.4 shows an expanded view of the test section, and Figure 3.5 shows the orifice-flange interface. To prevent leakage from the threaded joint, the nipples were then welded to the flange, on the sides that were away from the orifice. They were not welded on the sealing side of the flange to allow for expansion and contraction, thus preventing additional stresses.

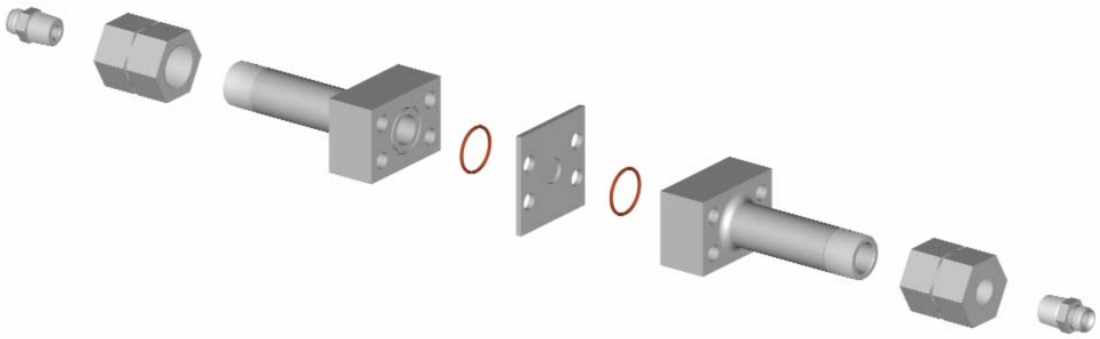

Figure 3.4 Expanded view of the Test Section (Mincks 2002)

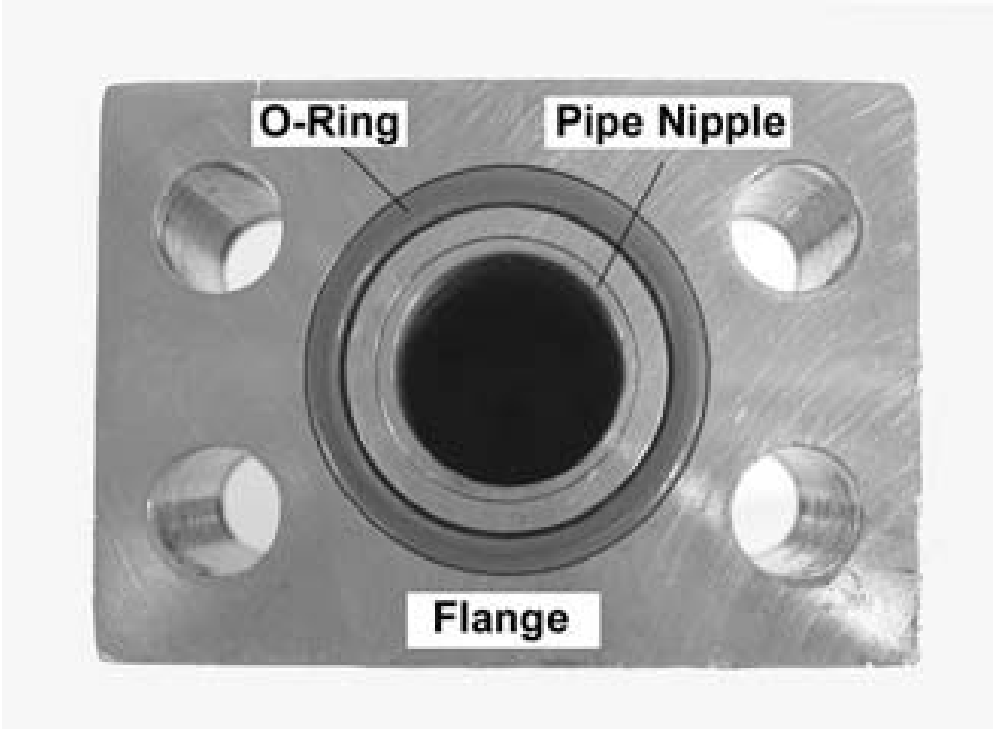

Figure 3.5 Orifice Flange Interface (Mincks 2002)

The one-inch nominal pipe nipple provides a large contraction ratio between the inlet flow passage and the orifice. The six-inch length of the nipple allows flow development and recovery upstream and downstream of the orifice, respectively. The details of this flow geometry are shown in Figure 3.6.

Three 1 mm diameter orifice plates were manufactured from 4.62 mm thick, 316L stainless steel and measured 7.6 cm on each side. Figure 3.7 shows a representative cross-sectional view of these plates while Table 3.1 provides the corresponding dimensions. This overall plate thickness of 4.62 mm was provided to withstand the large pressure drops across the orifice under consideration. The desired orifice thicknesses within these plates were achieved by milling holes of the appropriate depth into the plate on the downstream side. Thus, the 1 mm thick orifice was fabricated by milling a 5.2 mm diameter hole to a depth of 3.62 mm. Similarly, a 19 mm diameter hole was milled to a depth of 2.62 mm to create the 2 mm thick orifice, and a 25 mm diameter hole was milled to a depth of 1.62 mm for the 3 mm thick orifice. Stainless steel tubing of outer diameter of 1.27 mm (0.5 in.) with 2.1 mm (0.083 in.) thick walls (T 316L Seamless/Annealed ASTM-A213/A269) was used in rest of the oil loop. This high thickness provided adequate strength and allowed testing at the large pressures under consideration.

Back-cut dimensions were calculated using Equation 9 (Avallone and Baumeister 1996), along with the ultimate tensile strength of the material and a maximum differential pressure of 20 MPa as follows:

$$S_m = k\frac{wR^2}{t^2} \tag{9}$$

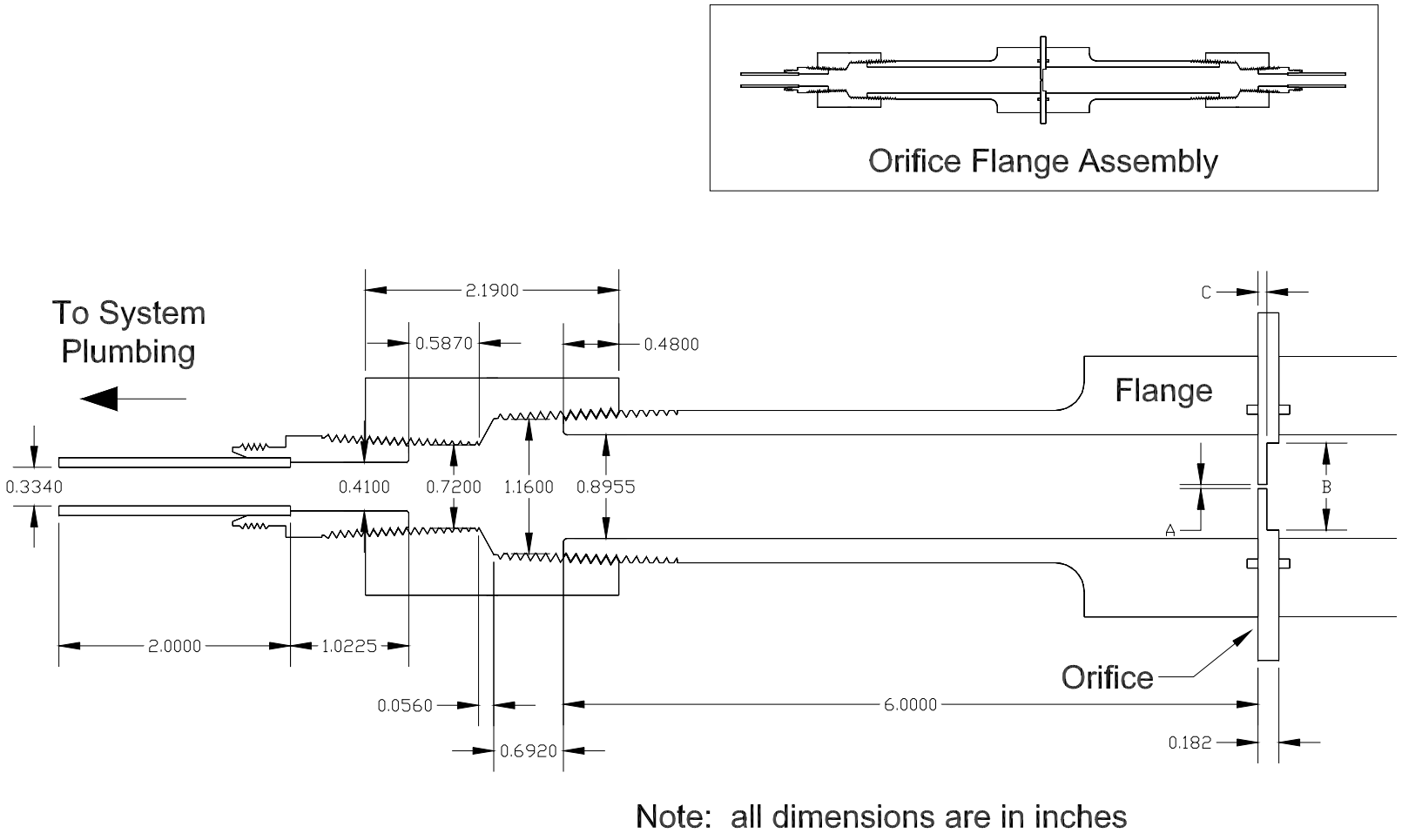

Figure 3.6 Test Section Dimensional Drawing (Mincks 2002)

Here, S_m is the ultimate tensile strength, w is the evenly applied load, t is the thickness of the material, R is the radius and k is a constant based on the ratio of disk radius to orifice radius. Similarly, three 3 mm diameter orifice plates were manufactured from 3.05 mm thick, 316L stainless steel, and three 0.5 mm diameter orifice plates were manufactured from 3.18 mm thick, grade A-2 tool steel. Back-cut and other dimensions for all the orifices are summarized in Table 3.1.

Table 3.1 Orifice Cross Sectional Dimensions

Nominal Thickness	d (mm)	B (mm)	l (mm)	A (mm)	l/d	d/D (D = 22.75)
0.5 mm Orifice Dimensions						
1 mm	0.5244	7.38	0.9952	2.9337	1.8978	0.0231
2 mm	0.5249	21.52	1.9782	2.9479	3.7687	0.0231
3 mm	0.5259	N/A	3.0099	3.0099	5.7233	0.0231
1.0 mm Orifice Dimensions						
1 mm	1.0130	5.18	1.0290	4.423	1.0158	0.0445
2 mm	1.0030	19.05	1.9561	4.623	1.9502	0.0441
3 mm	1.0109	25.40	2.8859	4.623	2.8548	0.0444
3.0 mm Orifice Dimensions						
1 mm	3.1187	7.35	1.0128	3.0068	0.3248	0.1371
2 mm	3.1071	21.60	2.1275	2.9941	0.6847	0.1366
3 mm	3.0792	N/A	2.9972	2.9972	0.9734	0.1353
Overall Range:		***0.3248 < l/d < 5.7233***		***0.0231 < d/D < 0.1371***		

Photographs of the upstream and downstream sides of the 1 mm diameter orifices are shown in Figure 3.8.

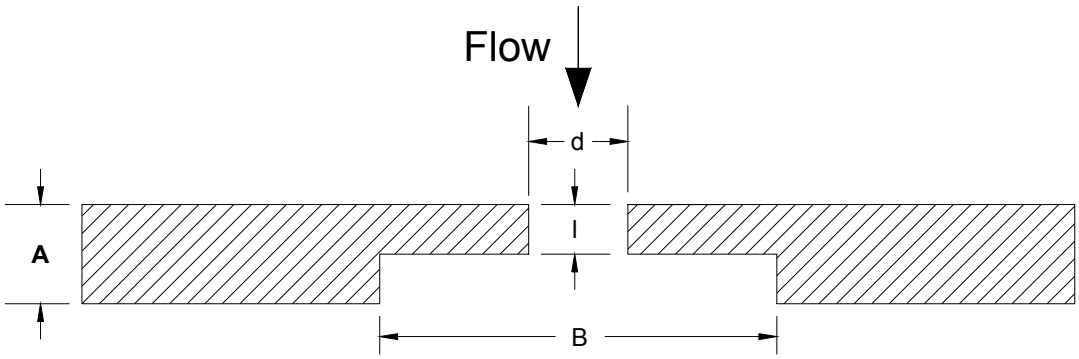

Figure 3.7 Orifice Plate Cross-Sectional Dimensions

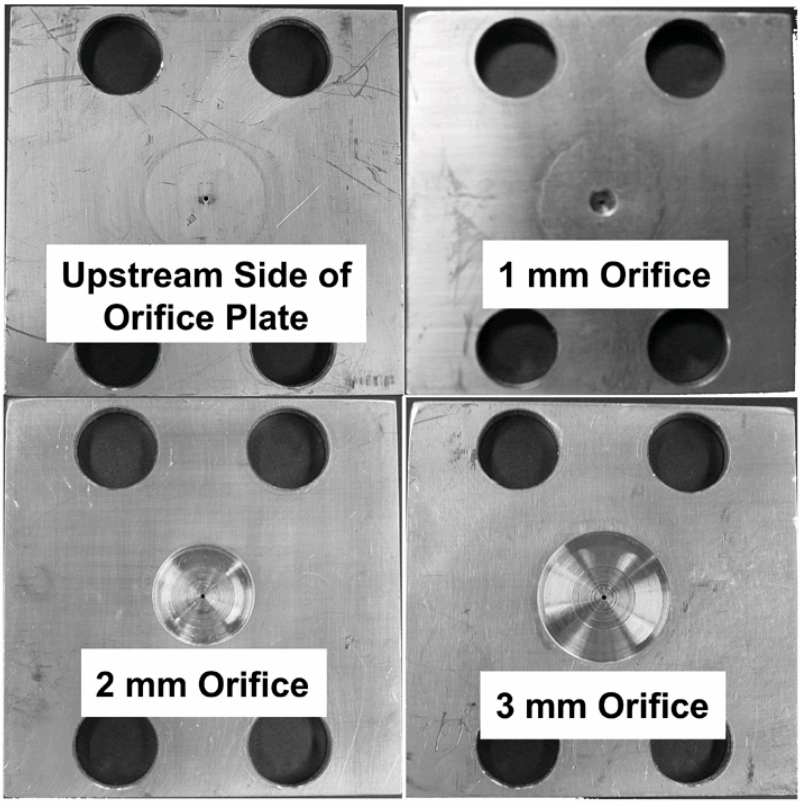

Figure 3.8 Orifice Plate Photograph -1 mm Diameter, Three Thicknesses (Mincks 2002)

3.3 Instrumentation and Controls

Temperatures and absolute pressures at the inlet and outlet of the test section, differential pressure across the orifice, and flow rate through the orifice were measured and recorded for each data point. Inlet and outlet temperatures of the oil were measured using 3-wire RTD's supplied by Omega Engineering, with a nominal accuracy of ± 0.6°C. Flow rates were measured using three different positive displacement flow meters supplied by AW Company, as shown in Table 3.2. Pulses generated by the flow meters were captured by inductive pickups on each meter and sent to a flow monitor. The flow monitor generated a 4-20 mA output signal that was converted to a 1-5 V signal for use by the data acquisition system.

Table 3.2 Flow Meters Specifications

Model	Range	Accuracy
ZHM-01	0.001 - 0.25	±0.5% @ $\nu = 3 \times 10^{-5}$ m^2/s, ±0.3% @ $\nu = 1 \times 10^{-4}$ m^2/s
ZHM-03	0.1 - 5.5	±0.5% @ $\nu = 3 \times 10^{-5}$ m^2/s, ±0.3% @ $\nu = 1 \times 10^{-4}$ m^2/s
JVM-60KL	2 - 20	±0.5% @ $\nu = 3 \times 10^{-5}$ m^2/s

Absolute and differential pressures were measured using Rosemount model 3051 pressure transducers. The absolute pressure transducers were capable of measuring pressures in the range of 0 kPa (0 psia) to 68,948 kPa (10,000 psia), with an accuracy of ±0.075% of span. The differential pressure transducer was capable of measuring pressures in the range of 13790 kPa (±2000 psid), with an accuracy of ±0.075% of span for spans larger than 2758 kPa (400 psid). For smaller spans, the accuracy of the

transducer is ±[0.025 + 10/span] % of span.

A PC-based data acquisition system supplied by IO Tech was used to display and record data during the test. The Tempscan/1000A with expansion unit EXP/11A interfaced with the computer through the program TempView 4.1, which allowed real-time display and recording of the temperatures, pressures, and flow rates.

3.4 Testing Procedures

A strict set of test procedures was established to ensure the collection of repeatable and accurate data for each orifice plate. Whenever the orifice plate was changed, it was necessary to fill the test section with oil and ensure that air was removed from the system. This was accomplished by flooding the test section with oil before the orifice plate was fully bolted into position. With the bolts at the bottom of the flanged slightly tightened, the top of the orifice plate was moved back and forth in the direction of each flange. This created a gap between the O-ring and the orifice plate, which allowed air to escape and the test section to be fully filled with oil. Once the air was removed by this method, the system was run for approximately 15 minutes in the maintenance configuration. For this configuration, the accumulator was isolated and flow was directed through the pressurized reservoir. This allowed any particulates in the line to settle out in the reservoir and any residual gases to be vented out of the system.

In the temperature range of $-30 < T < 10^{o}C$, typically ten data points were taken for each orifice plate, corresponding to a differential pressure range of 100 kPa (14.5 psi.) to 0.5 MPa. (725 psi.) (At the lower temperatures, the maximum differential pressure that could be obtained was about 0.5 MPa. (725 psi.)). The desired oil temperatures were

maintained by controlling the chilled coolant temperature and routing the oil through the appropriate heat exchanger (tube-in-tube, shell-and-tube, or both). The on-screen strip chart function of the data acquisition system was used to monitor the approach to steady state conditions, which for the low pressure data points, could take up to three hours.

Once the test loop reached steady state, the temperatures, absolute pressures, pressure drop, and flow rate were uploaded to the computer. During each test, the data acquisition system constantly monitored each enabled channel over 100 times a second. To get a good sample of the data, the readings were taken at the rate of one reading per second for two minutes. The average value of this set of 120 data points for each test case was then used for subsequent data analysis.

4. EXPERIMENTAL RESULTS

Over the course of this study, pressure drops were measured for various flow rates across the nine orifices under consideration. A description of the analysis of the measured parameters to obtain orifice pressure drops as a function of flow rate and geometry is presented below. In the discussion that follows, all the results obtained in the temperature range $20 \leq T \leq 50^{o}C$ are taken from Mincks (2002), while data for $-30 \leq T \leq 10^{o}C$ were obtained by the present investigator. The high temperature data are included here for completeness of the analysis, and for subsequent model development over the entire comprehensive range of test conditions.

4.1 Data Analysis

The experimentally determined pressure drop for each test case represents the pressure drop due to the orifice and that due to the test section piping located between the taps of the differential pressure transducer. A detailed representation of each segment of the test section is shown in Figure 4.1. To determine the pressure drop due only to the test section, a 3 mm thick orifice plate was constructed with a hole of the same diameter as the inlet pipe. Figure 4.2 shows the flow geometry for the test section with and without the orifice installed. For all temperatures under consideration, data were collected over a wide range of representative flow rates. These data were plotted and curve-fit as a function of flow rate that could be used to subtract these extraneous contributions from the measured pressure drop. The respective curve-fits for the different

cases are reported in Appendix A1. The extraneous contributions were then estimated for each data point using the respective flow rate, and subtracted from the measured differential pressures to obtain the pressure drop solely due to the orifice.

For the purpose of validation, these extraneous contributions were also computed using major and minor loss expressions for pipe flow from the literature. For each segment, the Reynolds number required for calculating these losses was based on the corresponding velocity and diameter. In addition, due to the non-Newtonian behavior, the viscosity μ in the definition of Reynolds number was replaced by μ_{ge} (generalized viscosity).

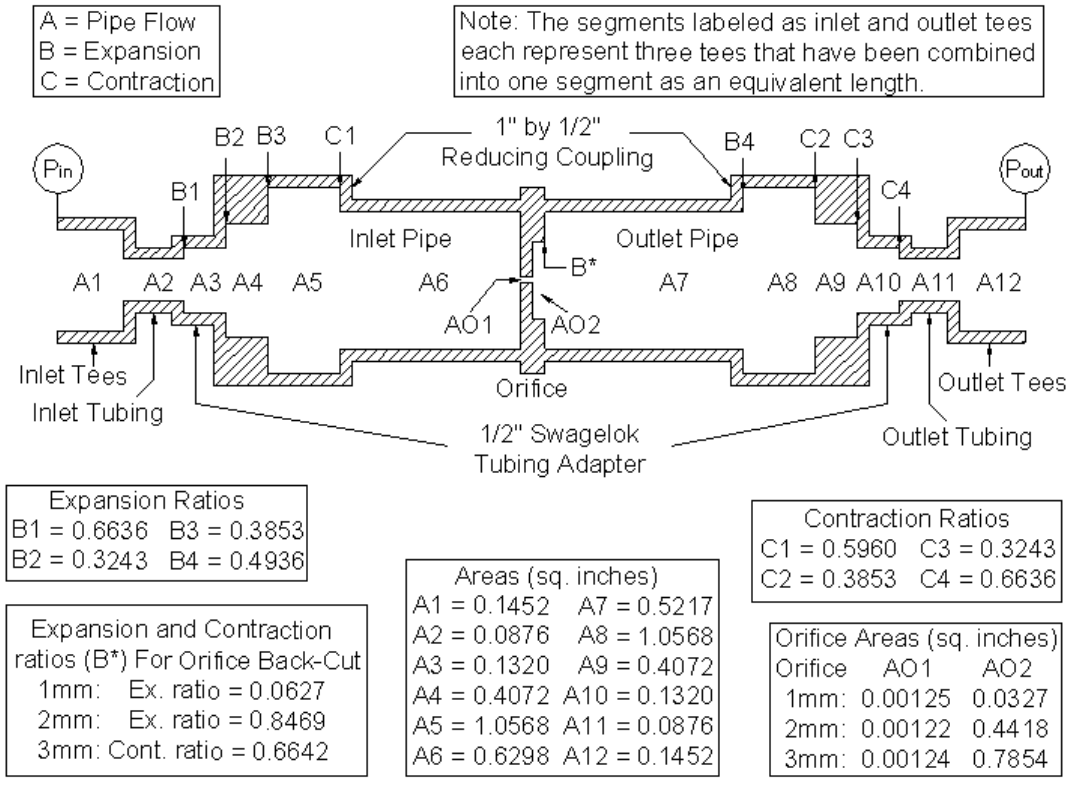

Figure 4.1 Details of the Flow Areas of the Test Section (Mincks 2002)

Density values were provided by the fluid supplier. For non-Newtonian analysis, the viscosity was calculated using the following equation suggested by Sorab et al (1993):

$$\mu_{ge} = a_T \mu_{H,0} + a_T (\mu_{L,0} - \mu_{H,0}) \left[1 + (a_T \lambda_0 \kappa)^2\right]^{\frac{(n-1)}{2}} \tag{4.1}$$

where,

$$a_T = e^{\left[A_2\left(\frac{T_0}{T}-1\right)+A_4\left(\frac{T_0}{T}-1\right)^2\right]} \tag{4.2}$$

In equations (4.1) and (4.2), $\mu_{L,0}$ is the low shear rate viscosity at the reference temperature (which was 40^{o}C for the fluid used in this study), $\mu_{H,0}$ is the high shear rate viscosity at the reference temperature, λ_0 is the inverse shear rate at the inception of shear thinning, n is the power law index (n = 0.383 for the present fluid), A_2 and A_4 are constants (unique for each non-Newtonian fluid) and κ is the shear rate. The values of the reference viscosities and constants A_2, A_4, λ_0 and n were provided by the fluid supplier.

The shear rate required to estimate the non-Newtonian viscosity was calculated using the measured flow rate and the respective segment diameter as follows:

$$\kappa_n = \frac{32Q}{\pi d^3} \tag{4.3}$$

To account for the fact that in non-Newtonian fluids, the velocity distribution deviates from a parabolic profile due to the variation of viscosity with shear rate, the above shear rate κ_n must be corrected as follows in Equation 4.4:

$$\kappa = \frac{(n' + 3)}{4} \kappa_n \tag{4.4}$$

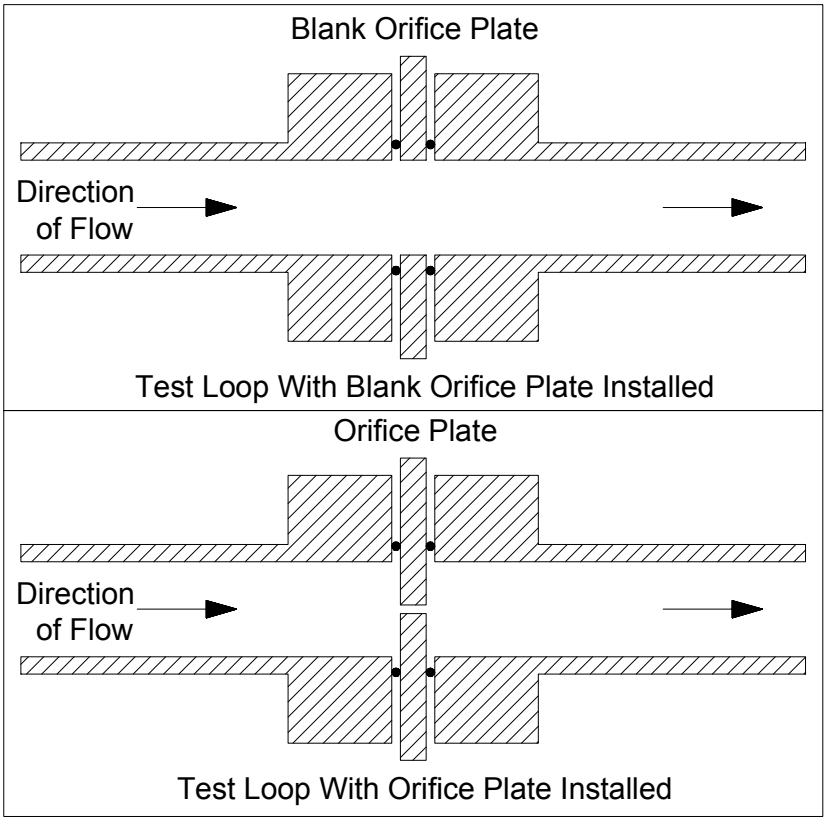

Figure 4.2 Schematic of Test Section With and Without Orifice Installed (Mincks 2002)

Here, the coefficient n′ is the slope of the log-log plot of shear rate vs. shear stress. The shear stress at each segment of the test section was calculated using the following equation:

$$\tau = \frac{\Delta P \times d}{4 \times l} \tag{4.5}$$

Here ΔP is the pressure drop in each segment, and d and l are the diameter and length of the segment, respectively. Since it was not feasible to measure the pressure drop across each segment experimentally, these individual contributions were calculated using frictional and minor loss expressions from the literature (Munson *et al.* 1998). From

these calculations, it was found that n′ was ≅ 1 for the range of shear stresses and shear rates observed in this study. Therefore the correction for κ shown above was deemed unnecessary for these data. Figure 4.3 shows a log-log plot of shear rate vs. shear stress for the 1 mm diameter, 1 mm thick orifice (for the orifice segment). This figure clearly demonstrates that n' is very close to 1 for all the temperatures under consideration. At 40°C and 50°C, a few data points show deviate from this trend; however, since this occurs at very high temperatures, the fluid is perhaps not non-Newtonian for these few data points.

With the viscosity thus established, the Reynolds number at each segment can be calculated. The inlet temperature and pressure were used for the evaluation of the fluid properties for the segments upstream of the orifice, whereas the outlet temperature and pressure were used for the downstream segments. For the frictional loss component of the pressure drop, the Darcy friction factor correlation by Churchill (1977) was used to calculate the friction factor for each segment as follows:

$$f = 8 \cdot \left[\left(\frac{8}{Re} \right)^{12} + \left(\left[2.457 \cdot \ln \left(\frac{1}{\left[\frac{7}{Re} \right]^{0.9} + 0.27 \cdot \frac{\varepsilon}{D}} \right) \right]^{16} + \left[\frac{37530}{Re} \right]^{16} \right)^{-\frac{3}{2}} \right]^{\frac{1}{12}} \quad (4.6)$$

In the above expression, the roughness of drawn tubing (ε = 0.0015 mm) was used for each segment.

The frictional pressure drops due to piping losses were calculated using this friction factor in the familiar manner as follows:

$$\Delta P_{pipe} = \frac{1}{2} f \frac{L}{D} \rho V^2 \tag{4.7}$$

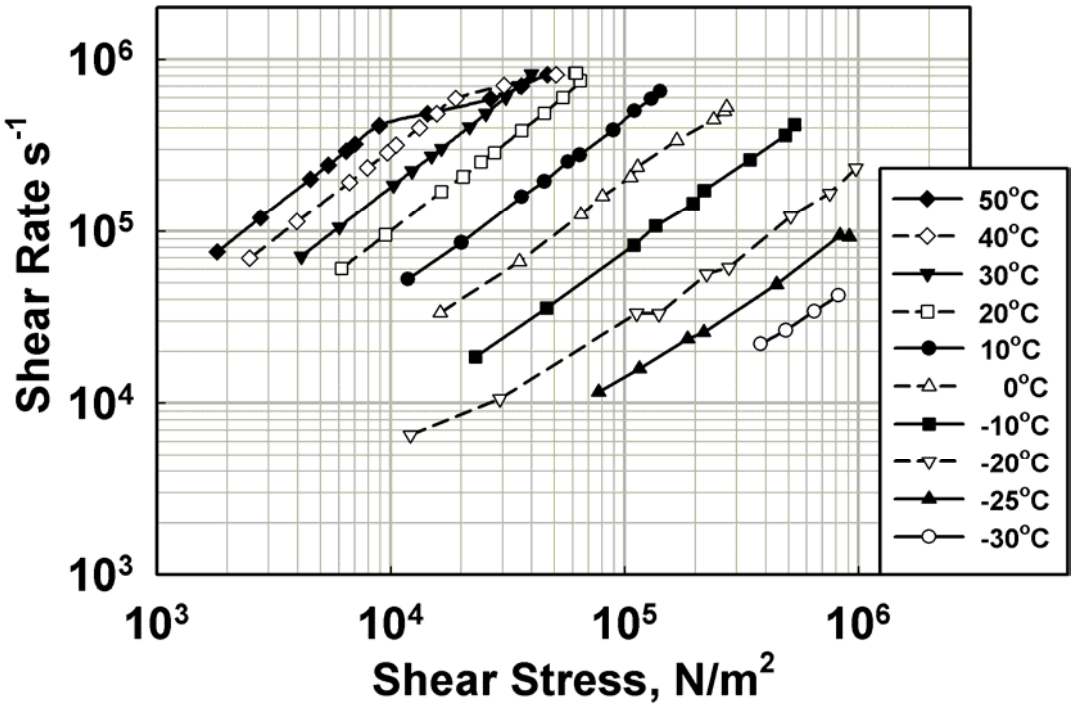

Figure 4.3 Shear Rate vs Shear Stress at the Orifice Segment (1 mm Diameter, 1 mm Thick Orifice)

Mınor losses due to the sudden expansıon and contractıon ın the test sectıon were also taken into account. The loss coefficient for sudden expansion was determined as follows (Munson *et al.* 1998):

$$K_L = \left(1 - \frac{A_1}{A_2}\right)^2 \tag{4.8}$$

The loss coefficient for a sudden contraction was obtained from the following curve-fit to a graph of the loss coefficient versus contraction ratio, which is available in Munson et al. (1998):

$$K_L = -0.021 + 0.585\left[1 + \exp\left(\frac{\frac{A_2}{A_1} - 0.705}{0.233}\right)\right]^{-2.29} \tag{4.9}$$

These loss coefficients were used to compute the "minor" pressure losses as follows:

$$\Delta P_{minor} = \frac{1}{2} K_L \rho V^2 \tag{4.10}$$

It is clear that flow through these segments is not fully developed. However, in the absence of readily available expressions for such flows, correlations for fully developed flow were used to determine these losses. Analyses of the data showed that except for very low temperatures and large flow rates, the extraneous contributions represented a very small fraction of the orifice pressure drop. This is illustrated in Figure 4.4 where the pressure profile along the test section is plotted for two different geometries at different temperatures. Thus, it was deemed that this approximate treatment is adequate. One sample calculation using these pipe and minor loss expressions is shown in Appendix A1.

Figure 4.5 shows the pressure drop across the orifice, as well as the extraneous contributions, for the 1 mm diameter, 3 mm thick orifice. This graph shows the experimental data with the blank plate, the estimates of these same extraneous pressure drops using frictional and minor loss calculations, and the pressure drop data for the orifices for $-20 < T < 10^{o}C$. In these graphs, it can be seen that the extraneous contributions remain a small fraction (2 – 15% over the range of test conditions) of the orifice pressure drop, although the relative contribution is somewhat higher than that seen in the high temperature tests. This is because for similar orifice differential pressures, the flow velocities at higher temperatures are higher, which leads to larger losses in the upstream and downstream parts of the test section. It can also be seen that over the range

of these conditions, the estimates for extraneous pressure drops are on average within 40% of the data obtained with the blank plate. The conditions at which the largest discrepancy occurs are at low flow rate cases, primarily because of difficulties in maintaining a steady flow rate from the pump at extremely small flow rates. As the low temperatures are approached, the agreement improves considerably, to within 14% at the -25 and -30^{o}C cases.

Based on the validation results presented above, for the rest of this study, the orifice pressure drops were obtained from the measured pressure drops using the curve fits obtained from blank data to estimate the extraneous contributions.

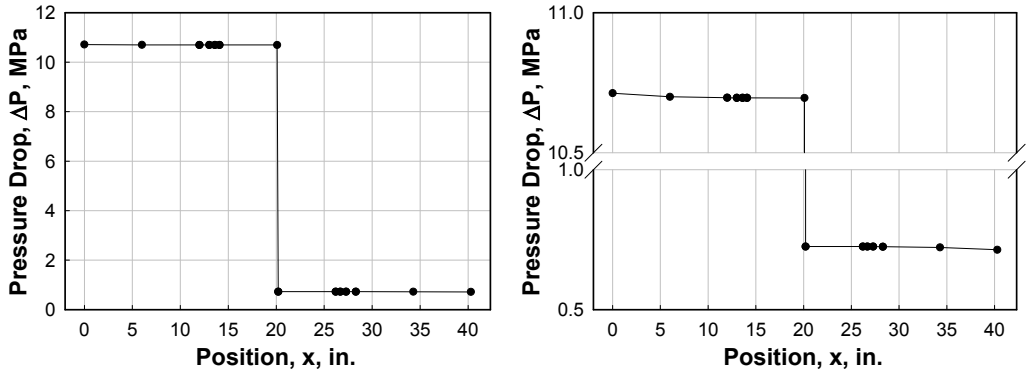

Point 13-100-50 (1 mm Dia., 3 mm Thick, 100 Bar Pressure Drop, 50°C) (Mincks 2002)

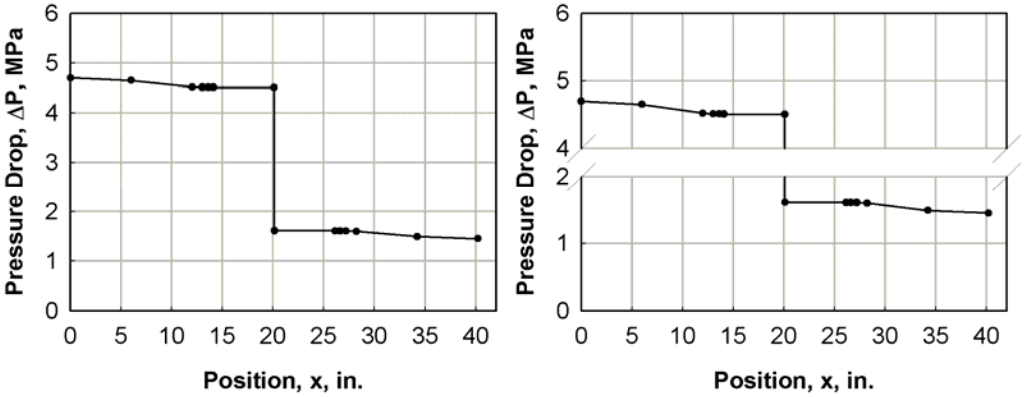

Point 11-35-20 (1 mm Dia., 1 mm Thick, 35 Bar Pressure Drop, -20°C)

Figure 4.4 Pressure Profile along the Test Section

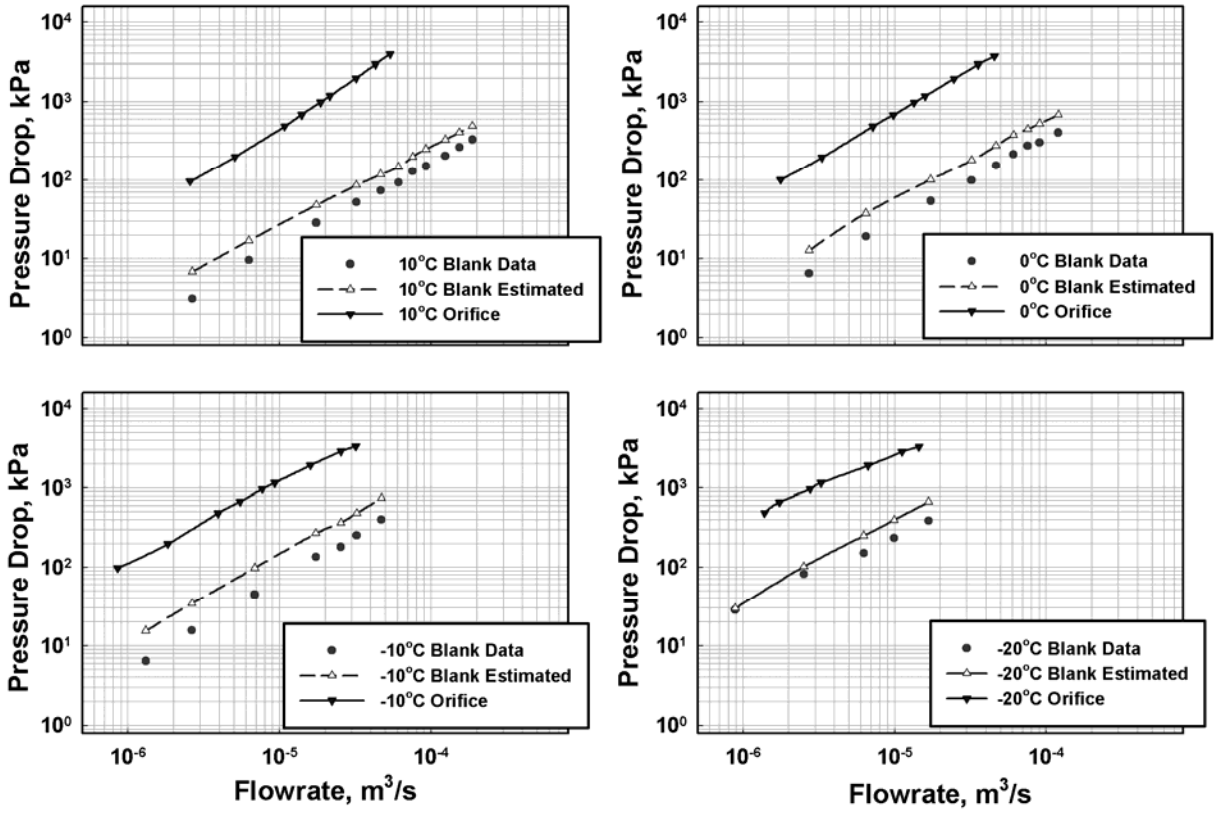

Figure 4.5 Experimental and Calculated Pressure Drops for the Test Section with the Orifice Plates Removed, Shown in Comparison With the 1 mm Diameter, 3 mm Thick Orifice Data (-20 ≤ T ≤ 10°C)

4.2 Discussion of Results

Once the orifice pressure drop was obtained using the techniques described above, the effect of the relevant parameters affecting the pressure-flow characteristics was investigated. Thus, in the following discussion, the variation of orifice pressure drop with flow rate is presented with fluid temperature and orifice geometry as parameters.

4.2.1 Effect of Temperature

Figures 4.6, 4.7 and 4.8 show the variation of pressure drop with flow rate for the 1 mm diameter orifice for 1, 2 and 3 mm thicknesses, respectively for the range of temperatures considered in this study. Similar graphs for the other six orifices are presented in Appendix B.

It can be seen from these three figures that as the temperature decreases, the pressure drop at any given flow rate increases; however, the slope of these curves decreases with temperature. In addition, the effect of temperature diminishes as the higher temperature range is approached, with the plots for the different temperatures merging into each other, especially at the higher flow rates. Thus, the effect of oil properties (primarily viscosity, which is a strong function of temperature) decreases at the higher flow rates. The effect of fluid properties (primarily viscosity) is not significant at higher flow rates, due to the approach to turbulence, which is consistent with the literature on discharge coefficients. These same trends were observed for the 0.5 mm and 3 mm diameter orifices. For the 3-mm diameter orifices, the plots (in Appendix B) at different temperatures are almost superimposed on each other for $T > -10^{o}C$, but as the temperature decreases to $-20^{o}C$ and $-25^{o}C$, there is a substantial effect of temperature on the pressure drop for a given flow rate.

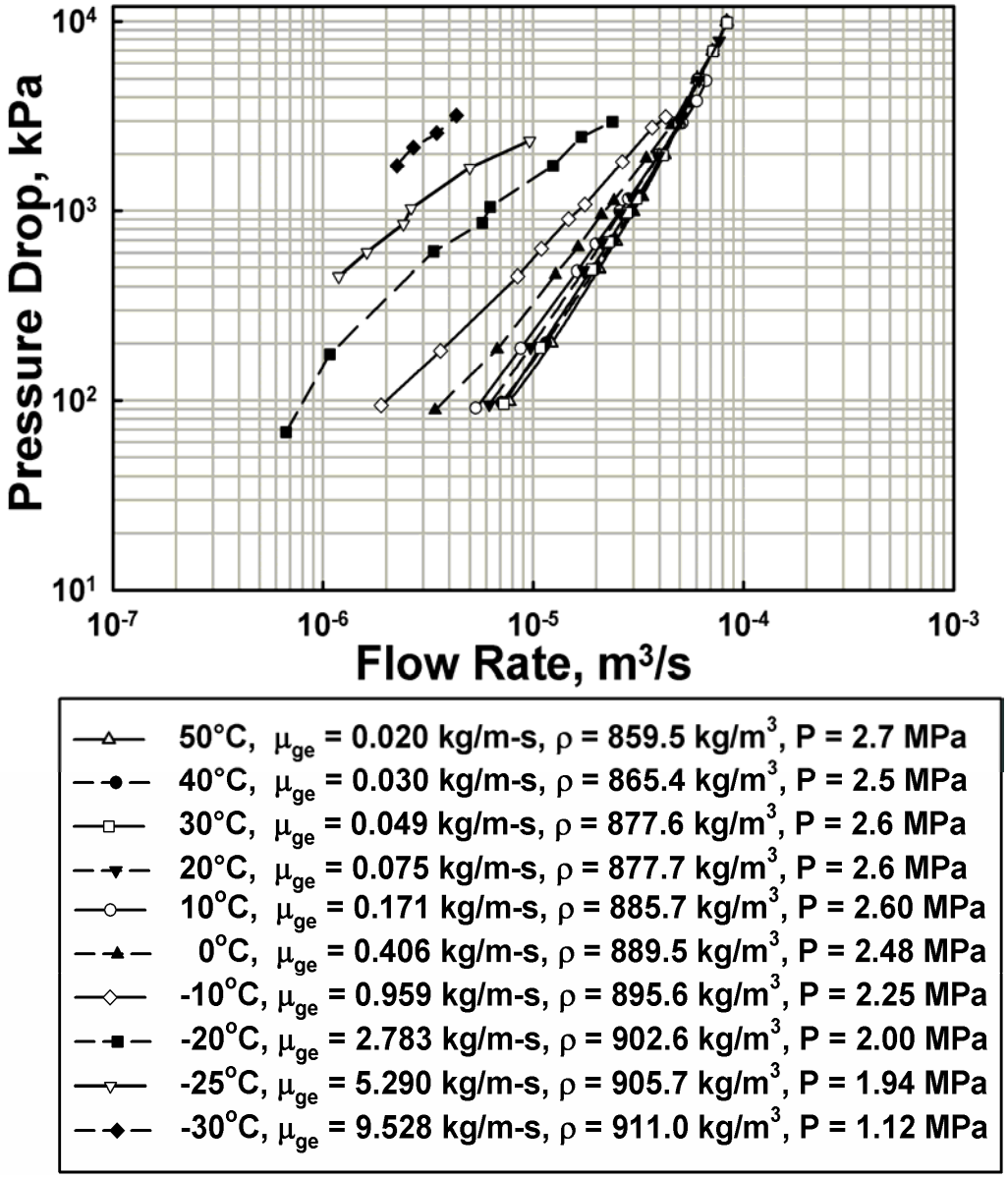

Figure 4.6 Effect of Temperature on Pressure Drop – Flow Rate Characteristics for the 1 mm Diameter, 1 mm Thick Orifice Plate

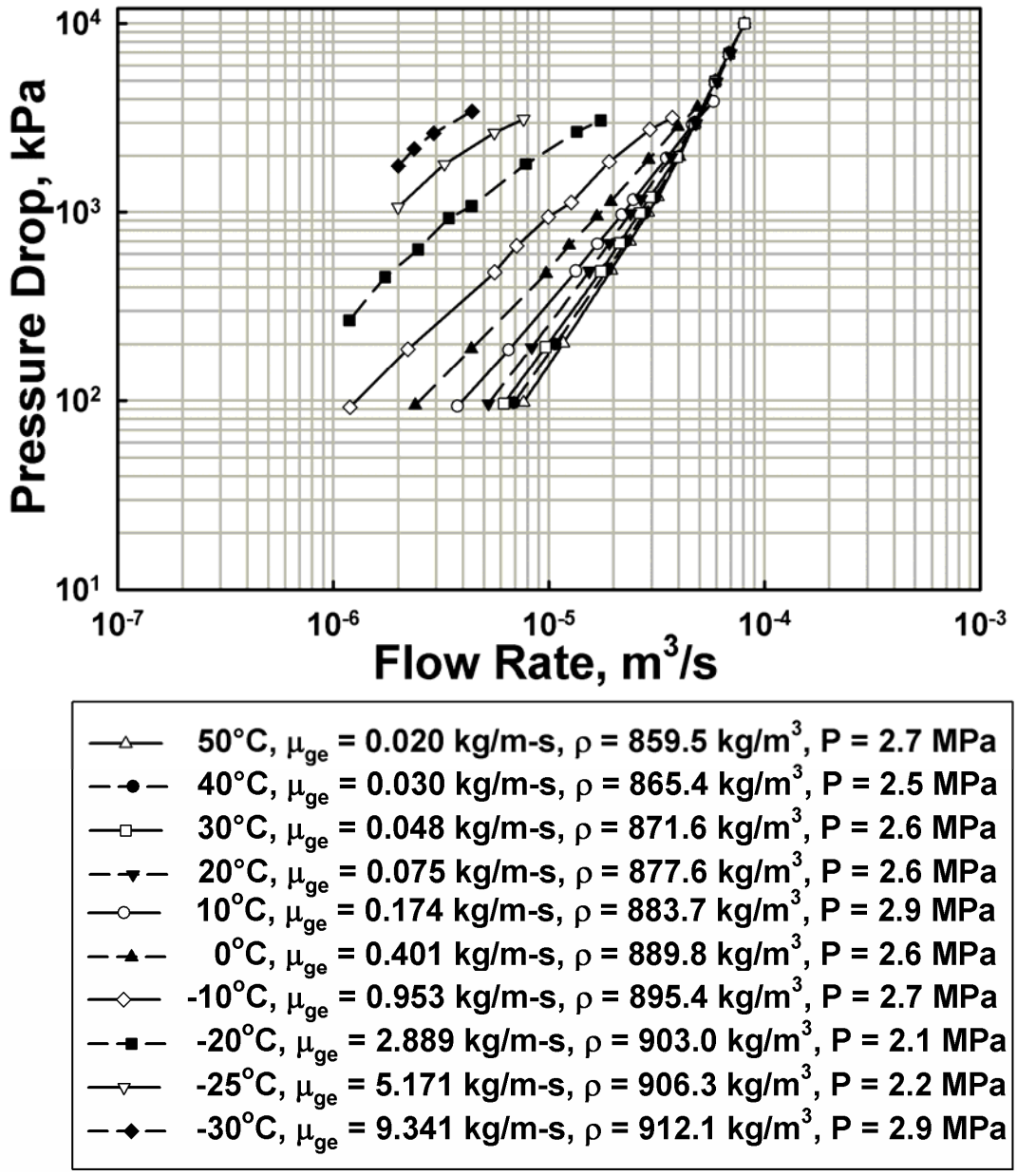

Figure 4.7 Effect of Temperature on Pressure Drop – Flow Rate Characteristics for the 1 mm Diameter, 2 mm Thick Orifice Plate

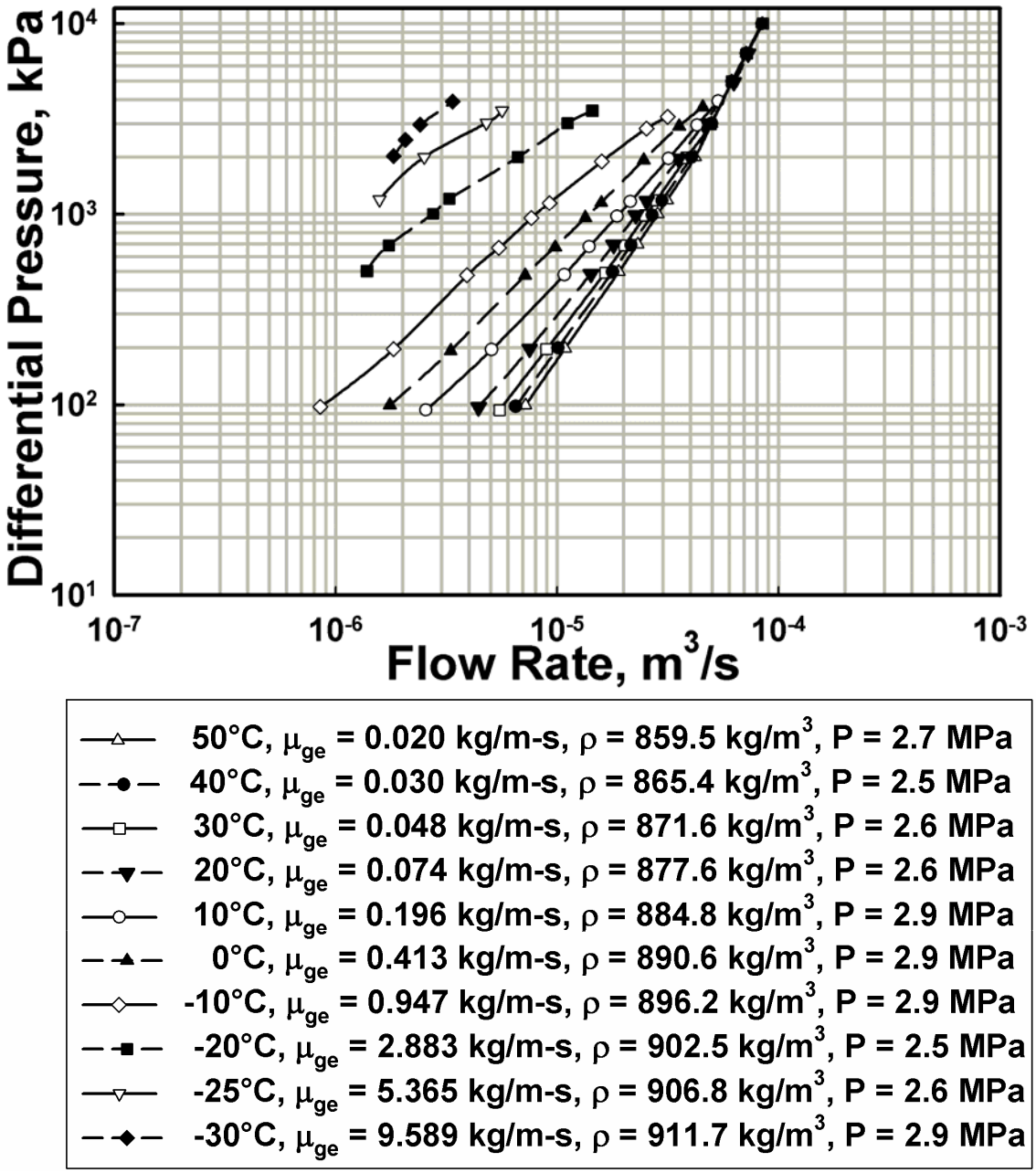

Figure 4.8 Effect of Temperature on Pressure Drop – Flow Rate Characteristics for the 1 mm Diameter, 3 mm Thick Orifice Plate

4.2.2 Effect of Orifice Thickness

Figure 4.9 shows the effect of orifice thickness for the 1 mm diameter orifices at the two extreme temperatures of 50^{o}C (Mincks 2002) and -10^{o}C. Similar graphs for other temperatures and for other orifices are shown in Appendix B. From this figure, it is apparent that as the orifice plate thickness increases, the pressure drop for a given flow rate increases at a given flow rate. The effect of orifice thickness on pressure drop is somewhat lower at the higher flow rates, as can be seen clearly for the 50^{o}C case. Thus, the effect of orifice thickness is more pronounced at lower flow rates and lower temperatures.

Similar trends are also seen for the 0.5 mm diameter orifice. However, in the 0.5 mm diameter case, the flow rates for the three thicknesses never converge to a single graph, independent of thickness, as seen in the 1 mm diameter orifices. This may be attributed to the fact that the flow rates through the 0.5 mm diameter orifices are much lower than those in the 1 mm and 3 mm diameter orifice tests.

For the 3 mm diameter orifices, the effect of orifice thickness is observable only at higher temperatures. Almost over the entire range of the data, the 2 mm and 3 mm thicknesses appear to have almost identical flow rates. The 1 mm thick orifice, however, exhibits a higher pressure drop for the same flow rate than the 2 mm and 3 mm thick orifices, particularly at the higher temperatures. This is the opposite of the trends described above for the 0.5 and 1 mm diameter orifices, where the pressure drop increases with an increase in orifice thickness. This reversal may be explained by the change from predominantly laminar flow in the smaller diameter orifices toward turbulent flow in the 3 mm diameter orifices.

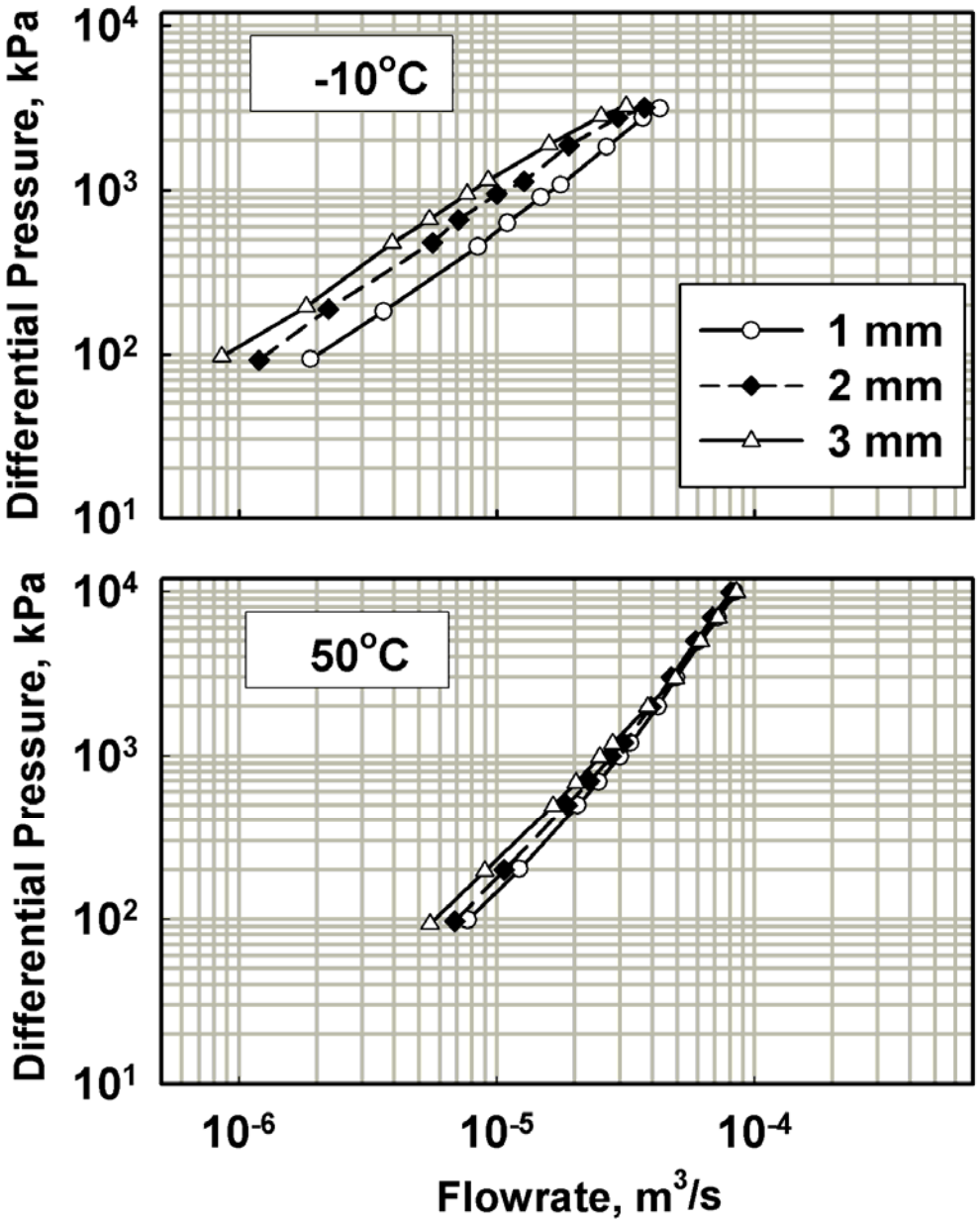

Figure 4.9 Effect of Orifice Thickness on Pressure Drop – Flow Rate Characteristics for the 1 mm Diameter Orifice, T = - 10°C and 50°C

5. NON-DIMENSIONAL ANALYSIS AND MODEL DEVELOPMENT

In this chapter, trends in the data from the present study are discussed in terms of the relevant non-dimensional parameters, and compared with the results from previous studies. Results from the present study are also modeled using regression techniques to obtain an overall orifice flow model for the full range of data.

The Euler number is used to represent the pressure drop in non-dimensional form as follows:

$$Eu = \frac{\Delta P}{1/2\,\rho V^2} \tag{5.1}$$

Here, ΔP is the pressure drop due to the orifice only, and ρ and V are the density and velocity at the orifice, respectively. The generalized Reynolds number is calculated as follows:

$$Re_{ge} = \frac{\rho V d}{\mu_{ge}} \tag{5.2}$$

It should be noted that in the literature on non-Newtonian fluids, the generalized Reynolds number is typically represented explicitly in terms of the consistency coefficient and the power law index. However, since the non-Newtonian viscosity is used to calculate Reynolds number here as described in the previous chapter, this definition of Reynolds number provides an equivalent treatment. With the respective non-dimensional terms calculated in this manner, the pressure-flow characteristics of orifice flow and their variation with geometry and fluid properties are discussed below in non-dimensional form.

5.1 Uncertainty Analysis

Uncertainties in the above mentioned non-dimensional parameters were computed using an error propagation approach (Taylor and Kuyatt 1993). The Reynolds number depends on the flow rate, diameter, and the density and viscosity of the fluid. The uncertainties in the flow rates were calculated from the specifications of the manufacturer (AW Company) of the flow meters, which were ±0.5% of the actual reading for viscosities $< 3\times10^{-3}$ m^2/s and ±0.3% of actual reading for viscosities $\geq 3\times10^{-3}$ m^2/s. The uncertainties in the diameter were taken as ±0.0025 mm for all the orifices. Since the density varies with the temperature and pressure, variations (partial derivatives) in the density with respect to temperature and pressure were calculated. The uncertainty in temperature measurements was ±0.6^oC, while the uncertainty in the pressure measurement (from the transducer specifications) was 10.342 kPa (1.5 psi). Similarly, the viscosity of the fluid varies with the temperature and shear rate; thus, uncertainties in the temperature and shear rate measurement were used to calculate uncertainties in the viscosity. For a representative data point of 35 bar pressure drop at -20^oC in the 1 mm diameter, 1 mm thick orifice, uncertainties in the Reynolds number was found to be 7% of the measured Re of 9.72. For the range of Reynolds numbers investigated in this study, $0.09 < Re_{ge} < 9976$, the uncertainties are in the range of $2.53 < U(Re_{ge}) < 17.6\%$, with the smallest diameter orifice having the largest uncertainties, especially at the very low temperatures, because of difficulties in controlling the temperature to steady values at such low flow rates. Details of these calculations are presented in Appendix A.

Uncertainties in the Euler number were computed to account for the uncertainties in the measurements of the density, flow rate, diameter and pressure drop. The

uncertainties in the orifice pressure drop were due to the uncertainty in the differential pressure transducer measurements, which was ±7.757 kPa (1.12 psi), and uncertainties in the measurement of the extraneous plumbing losses, which were taken to be ±25% of the losses measured using the blank orifice. For the above mentioned representative data point, the uncertainty in the Euler number was found to be 4.77% of the measured Eu of 7.485. The Euler number for the tests under consideration encompasses the range $1.3 < Eu < 2636$. Uncertainties in Eu for 0.5 mm and 1 mm diameter orifices are less 8% for all the data points. The largest Euler number observed for these orifices was 766. However, for the 3 mm diameter orifices, at low temperatures (< 0^oC) uncertainties are of the order of 40% or more (for approximately 8% of the data points), increasing with a decrease in temperature. This is attributed to unsteady pump operation, and also to the fact that the extraneous plumbing losses (in addition to the orifice pressure drop) that are included in the measured pressure drop constitute a larger fraction for this orifice. Thus, the uncertainties in the estimation of these extraneous pressure drops have a larger influence on the uncertainty in the orifice pressure drop for such cases.

5.2 Effect of Aspect Ratio on Euler Number

The Euler number is presented as a function of Reynolds number in Figure 5.1 for -10^oC, 20^oC and 50^oC on a log-log scale. It can be seen that for all orifices, as the Reynolds number increases, Eu first decreases and then assumes constant values (seen at higher temperatures considered). In addition, at low Reynolds numbers, an increase in the aspect ratio (l/d) causes an increase in the Euler number at a given Reynolds number. These effects can be categorized based on three flow regimes that can be seen in Figure 5.1.

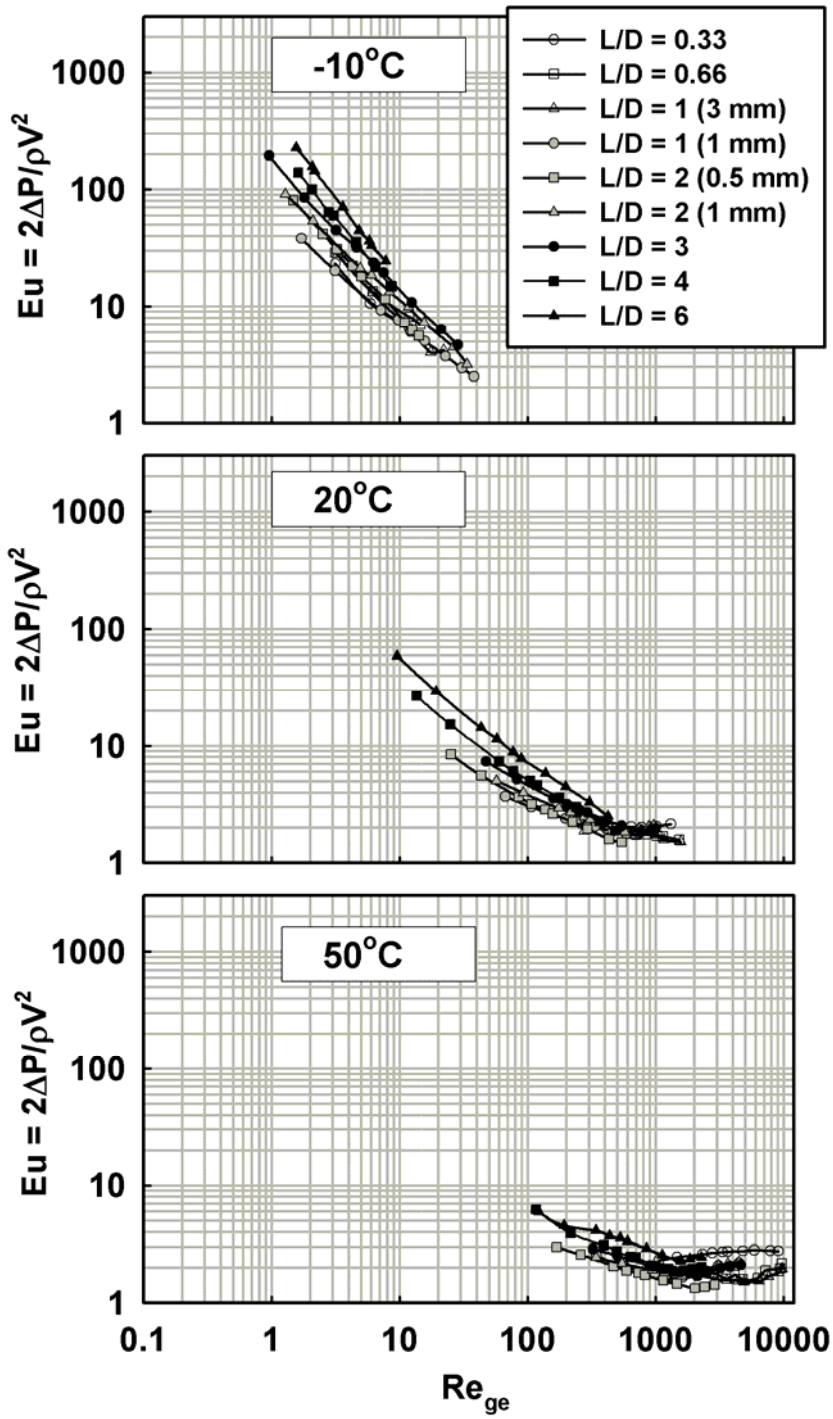

Figure 5.1 Effect of Aspect Ratio on Euler Number (20 and 50°C, Mincks (2002))

The low Re region, where log(Eu) decreases almost linearly with increasing log(Re) is the laminar region, while the region where the Eu- Re curve starts flattening out is the transition region. Based on this distinction, it can be said that at -10^{o}C, all the data are in the laminar region for all the aspect ratios. At higher Reynolds numbers, i.e., the turbulent region, the effect of aspect ratio on Euler number is weaker and in some cases, the Eu is larger for lower aspect ratios (as was also discussed in the previous chapter in terms of the effect of orifice thickness on pressure drop). Also, at these high Re values beyond the minima in Euler number, an increase in Re does not cause any appreciable increase in Eu, and Eu tends to assume a constant value as the Re is increased. At 50^{o}C, most of the data fall in transition region where each curve attains its minima at slightly different Re values based on the aspect ratio. A few turbulent data points are also seen. The other observation from these graphs is the considerable shift in Re and Eu values for similar flow rates as the temperature changes from -10^{o}C to 50^{o}C, primarily because of the change in viscosity.

5.3 Effect of Orifice Diameter on Euler Number

In this study, aspect ratios of 1 and 2 were obtained with 2 orifices for each aspect ratio. For example, the 1 mm diameter orifice of 1 mm thickness, and the 3 mm diameter orifice of 3 mm thickness both have aspect ratios of 1. Similarly the 1 mm diameter orifice of 2 mm thickness and the 0.5 mm diameter orifice of 1 mm thickness both have aspect ratios of 2. In Figure 5.2, Eu is plotted against Re on a log-log scale for aspect ratios of 2 with orifice diameter as a parameter for two temperatures.

In general, it appears that there is a slight increase in Euler number as the diameter is increased, keeping the aspect ratio constant; at the very low Re values, the diameter does not appear to appreciably affect the Euler number.

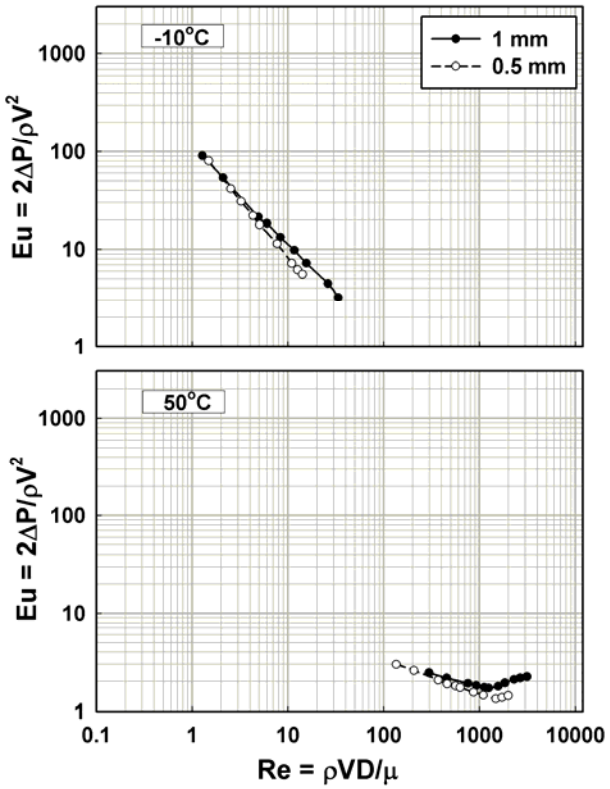

Figure 5.2 Effect of Diameter on Euler Number for l/d=2 (50°C, (Mincks 2002))

5.4 Effect of Fluid Temperature on Euler Number

Figure 5.3 shows the effect of temperature on Eu for an aspect ratio of 1 (1 mm diameter, 1 mm thick orifice) for Re (using a Newtonian treatment) and Re_{ge} (using a non-Newtonian treatment). In all these plots in this figure, the geometry remains constant; hence it can be seen that the variation in temperatures (and flow rates) provides

for a wide range of Reynolds numbers. The Euler number for pipe flow in the laminar region ($Eu = (64/Re)\times(l/d)$), is also plotted in Figure 5.3 for reference. Similarly, the turbulent limit (shown as a dashed line) is also shown in this graph. This limit was calculated using the model of Morris and Garimella (1998) for orifice flows at high Re values. It can be seen that in the laminar region, the Eu-Re curves for these orifices are steeper than the corresponding pipe flow line. The other phenomenon that is visible in these graphs is the increase in Eu with an increase in temperature, keeping the Reynolds number constant. This can be explained as follows. As the temperature increases, the viscosity of the oil decreases. Therefore, to maintain the same Re, the velocity must decrease, because the density is essentially constant, and the orifice diameter remains the same. The lower velocity results in an increase in Eu because of the inverse square dependence of Eu on the velocity. A corollary to this dependence is that as the temperature is increased, a given Eu is obtained at a higher value of Re. This also explains the increase in the extent of the laminar region with an increase in temperature, as evidenced by the movement of the minima in the Eu-Re plot toward higher Re values. Similar graphs for the other aspect ratios investigated in this study are shown in Appendix C.

Figure 5.3 also shows two different sets of Eu-Re plots. The purpose of these graphs is to illustrate the effects of accounting for the non-Newtonian behavior of the fluid. Non-Newtonian behavior at the higher shear rates causes a decrease in the effective viscosity of the fluid. This can be viewed as being similar to the effect of increasing the temperature of a Newtonian fluid, which also decreases the viscosity. This decrease in viscosity causes an increase in the Reynolds number for a given flow rate,

compared to the corresponding Newtonian Re. Stated otherwise, the velocity required to obtain a given Reynolds number is lower when the non-Newtonian viscosity is used, which results in a higher Euler number at that same condition. This phenomenon is clearly visible in Figure 5.3, in which the plots in the laminar region are higher with the use of the non-Newtonian viscosity compared to the plots that use the Newtonian properties.

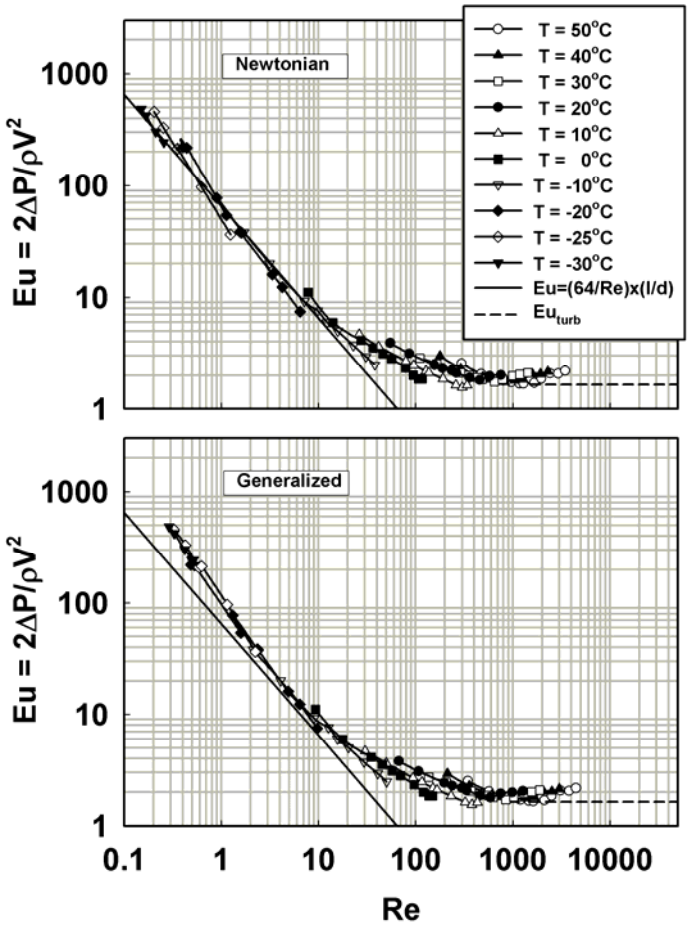

Figure 5.3 Effect of Temperature on Eu for l/d=1 (1mm Diameter, 1 mm Thick Orifice) – Illustration of non-Newtonian Effects

The increase in Eu with an increase in temperature can be seen more clearly in Figure 5.4, where the information presented in Figure 5.3 is plotted again, but without the extreme low temperature cases. This helps illustrate the behavior in the transition region better. In this region, because of the generally positive slope of the Eu-Re graph (in contrast with the laminar region slope), for a given Re, an increase in temperature results in a decrease in Eu. In a similar manner, in the turbulent region, due to an approach to a nearly constant Eu, the effect of temperature is not significant.

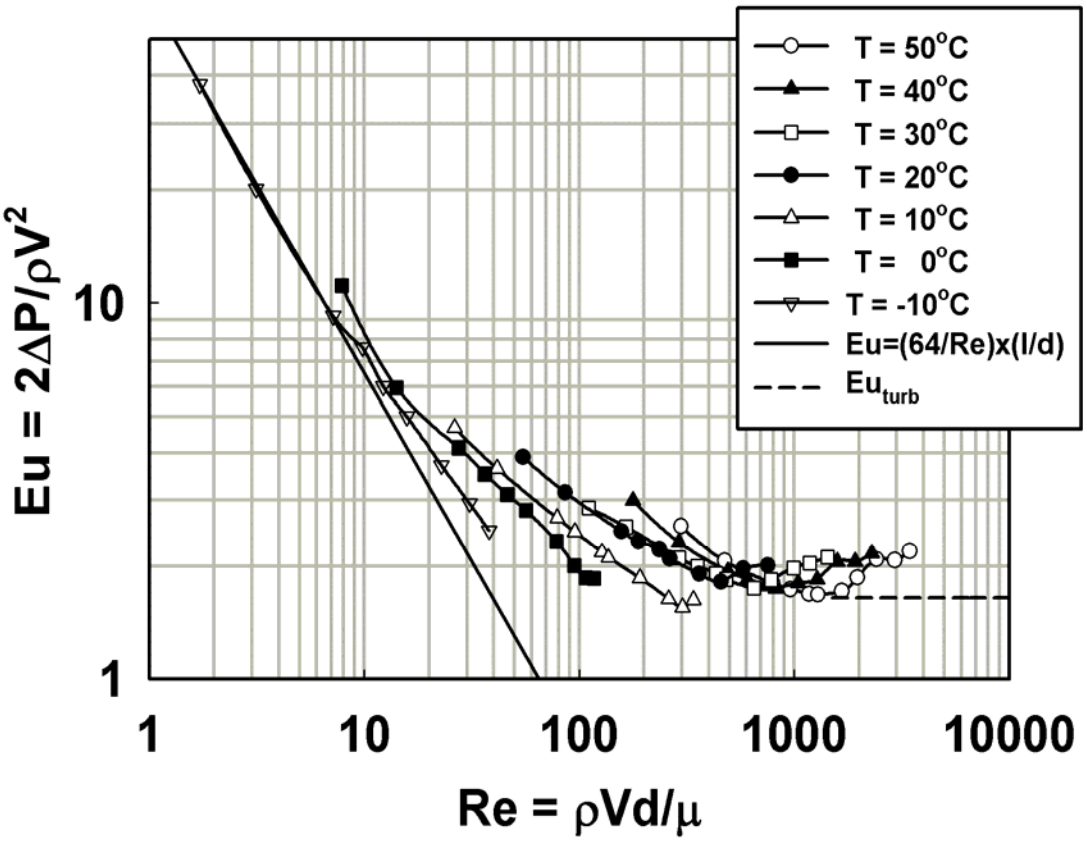

Figure 5.4 Effect of Temperature on Eu for l/d=1 (Expanded), (1 mm Diameter, 1 mm Thick Orifice)

5.4.1 Comparisons with Previous Work

Figures 5.5 to 5.13 show the Eu-Re graphs for each aspect ratio with the fluid temperature as a parameter. In addition, the available values from the literature are also plotted on these graphs. Figure 5.5 for l/d = 0.33 shows good agreement between the data from the current study and those of James (1961) and Kiljanski (1993), although both authors under-predict the current data, especially in the laminar and transition region. Part of this difference may be explained by the fact that their data are for an aspect ratio of 0.5, while the current data are for l/d = 0.33. For moderate and large Reynolds numbers, the data agree well with results of Tuve and Sprenkle (1933).

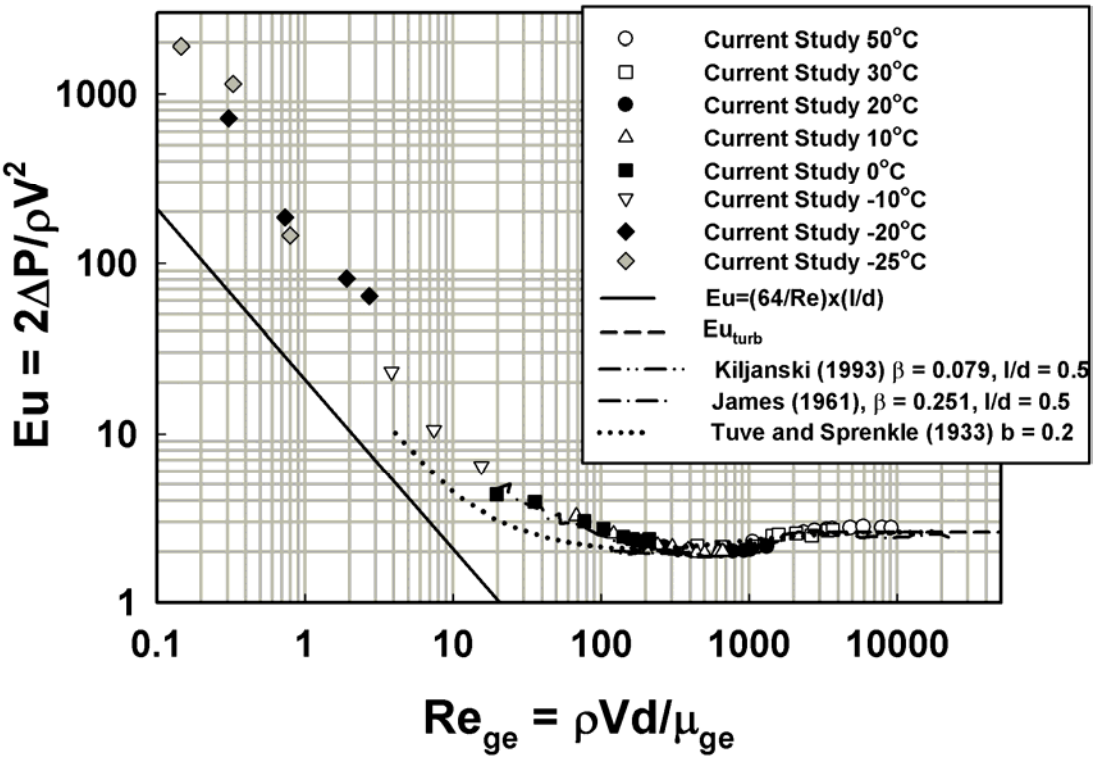

Figure 5.5 Eu versus Re for l/d = 0.33

Data from James (1961) and Kiljanski (1993) agree well with the data from the current study for l/d = 0.66 (Figure 5.6) at moderate Reynolds numbers, but now over-predict the current data at higher Reynolds numbers. However it is seen that at smaller Reynolds numbers, there is good agreement between the data from James (1961) and from the current study. Data from Tuve and Sprenkle (1933) also over-predict the current data at higher Reynolds numbers, but at lower Reynolds numbers, their Euler numbers are lower. Figures 5.7 and 5.8 compare the data for two orifices with an aspect ratio of 1 (1 mm diameter, 1 mm thick; 3 mm diameter, 3 mm thick) with the literature.

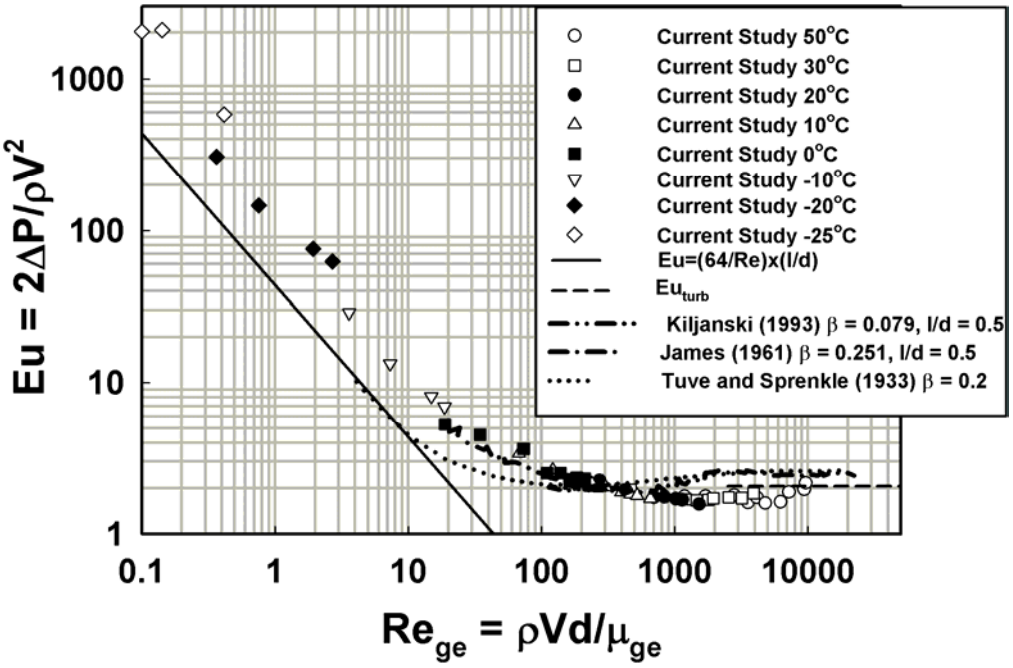

Figure 5.6 Eu versus Re for l/d = 0.66

A very good agreement is seen between the data from the current study and those from James (1961) although his data under-predict the current data at higher Reynolds numbers. Quite interestingly, data from James approach turbulent values calculated from

expression developed by Morris and Garimella (1998). Good agreement is also observed with the data from Sahin and Ceyhan (1996) especially at lower Reynolds numbers, Hasegawa et al. (1997), and Kiljanski (1993). However, now there is considerable deviation from the results of Tuve and Sprenkle (1933).

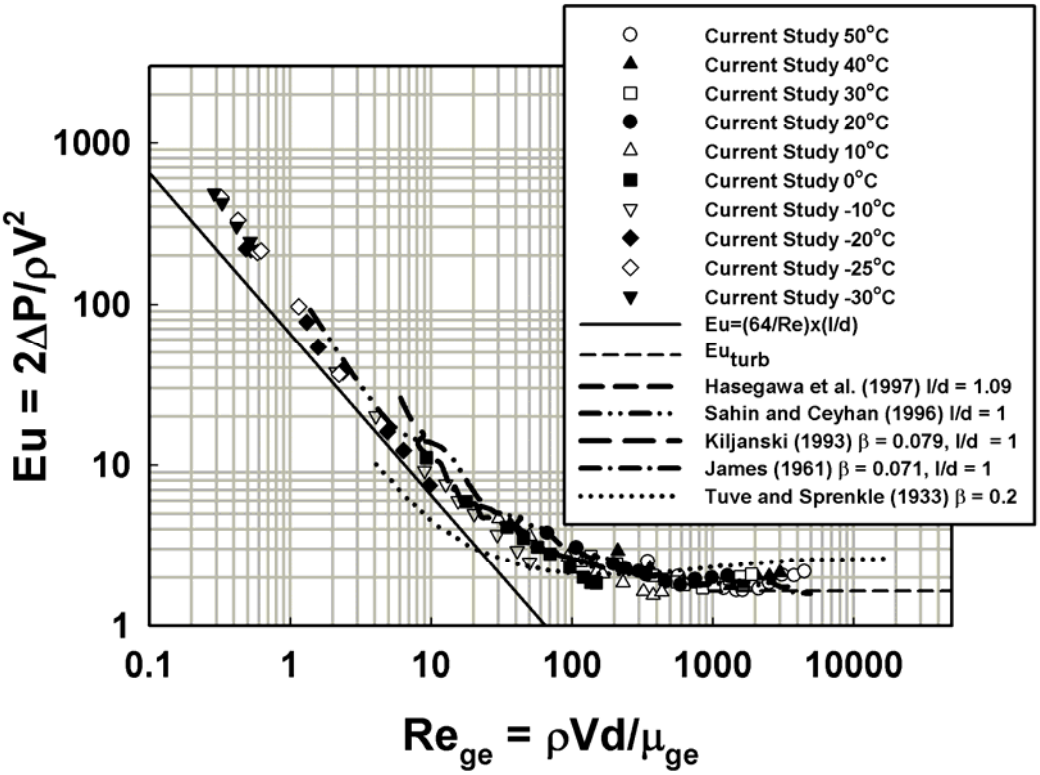

Figure 5.7 Eu versus Re for l/d = 1 (1 mm Diameter, 1 mm Thick Orifice)

From the above discussion of the comparison of the results from the present study for smaller aspect ratios (l/d < 1), it appears that there is good agreement with one or more papers from the literature at moderate Reynolds numbers (transition region). However, at extremes of very small and large Re values, the data differ from those available in the literature.

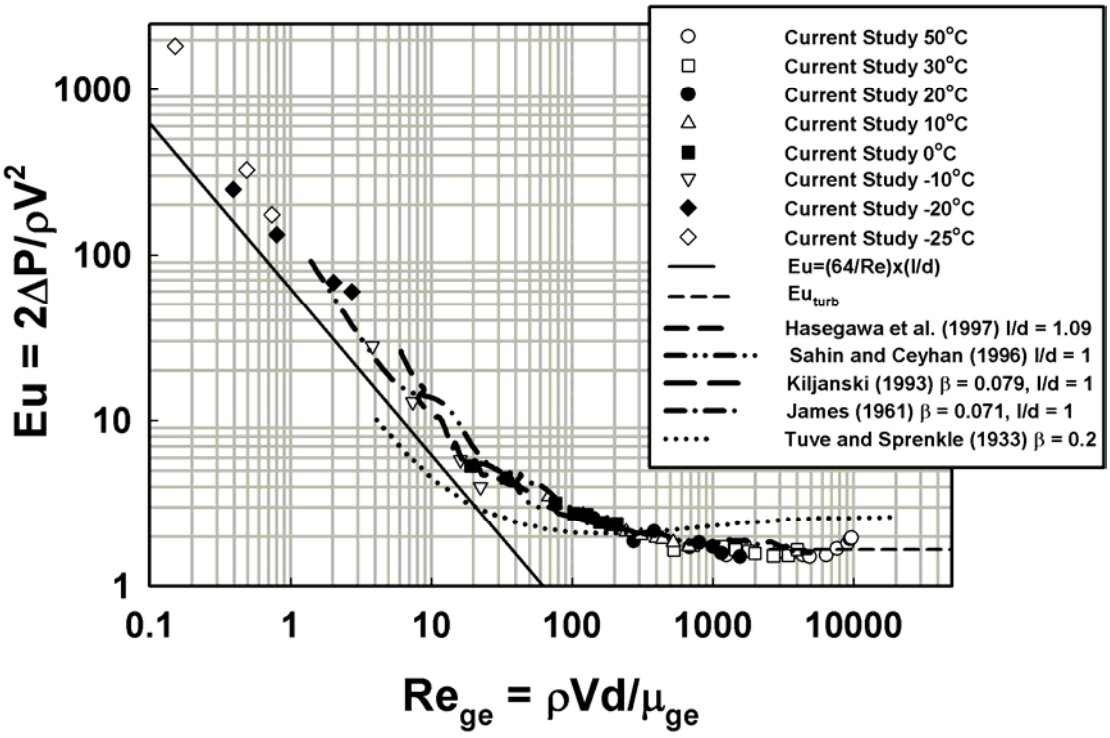

Figure 5.8 Eu versus Re for l/d = 1 (3 mm Diameter, 3 mm Thick Orifice)

Figures 5.9 and 5.10 show similar graphs for an aspect ratio of 2 (1 mm diameter, 1 mm thick; 0.5 mm diameter, 1 mm thick). It can be seen that the Eu number is somewhat higher at a given Reynolds number for the 1 mm diameter orifice (Figure 31) than the data for the 0.5 mm diameter orifice (Figure 5.10). This implies that at the same aspect ratio, a difference in orifice-to-pipe diameter ratio affects the Euler number. Data from Lichtarowicz et al. (1965) show good agreement with the data from the current study in these graphs at moderate Reynolds numbers. However, they severely over-predict the current data at low Re values, while slightly under predicting the data at higher Reynolds numbers for the 1 mm diameter orifice.

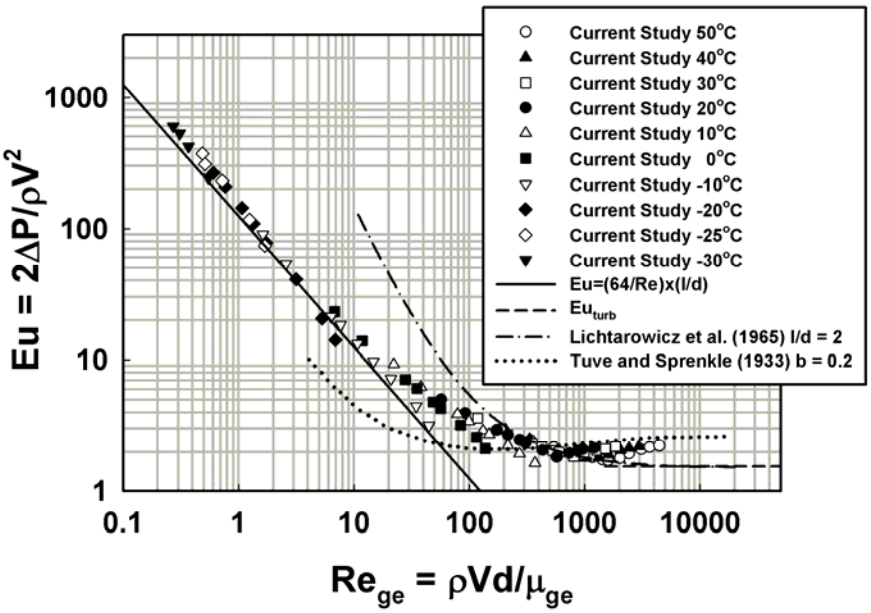

Figure 5.9 Eu versus Re for l/d = 2 (1 mm Diameter, 1mm Thick Orifice)

The Lichtarowicz et al. (1965) curve results from the compilation of data from several studies including those of James (1961). Although the agreement with the 0.5 mm diameter orifice data at higher Re values is slightly better, the prediction at low Re continues to be poor. The data from Tuve and Sprenkle (1933) under-predict at low Re and over-predict for large Re. Between the two orifices, the 1 mm diameter orifice shows better agreement with their results at higher Re.

Similar results are seen for aspect ratios of 3 and more. It is interesting to note that as l/d increases, data in the laminar region approach the Euler number corresponding to the fully developed pipe flow expression given by $(64/\mathrm{Re})\times(\mathrm{l}/\mathrm{d})$. This should be expected: as the aspect ratio increases, the geometry approximates a circular tube. Similar results for l/d =3, 4 and 6 are shown in figures 5.11-5.13, respectively.

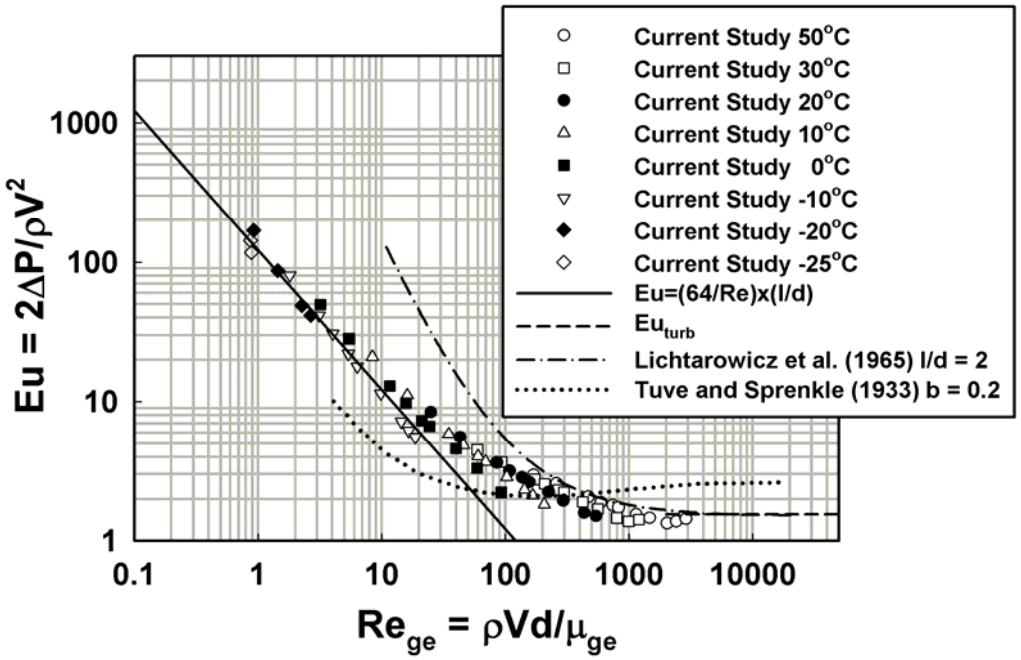

Figure 5.10 Eu versus Re for l/d = 2 (0.5 mm Diameter, 1 mm Thick Orifice)

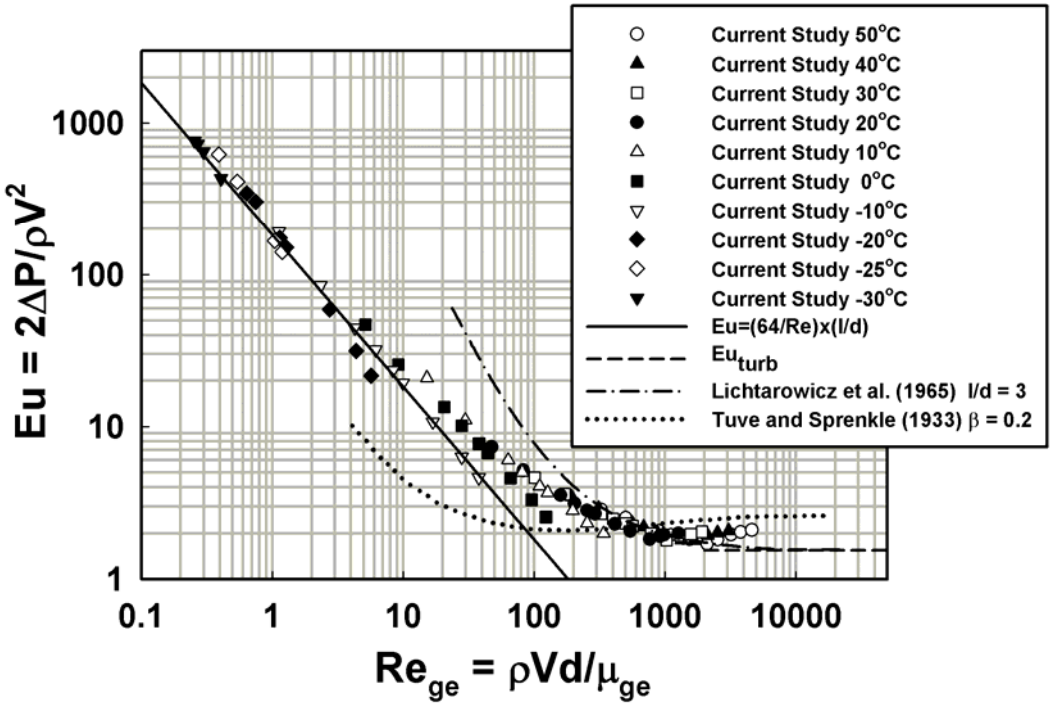

Figure 5.11 Eu versus Re for l/d = 3

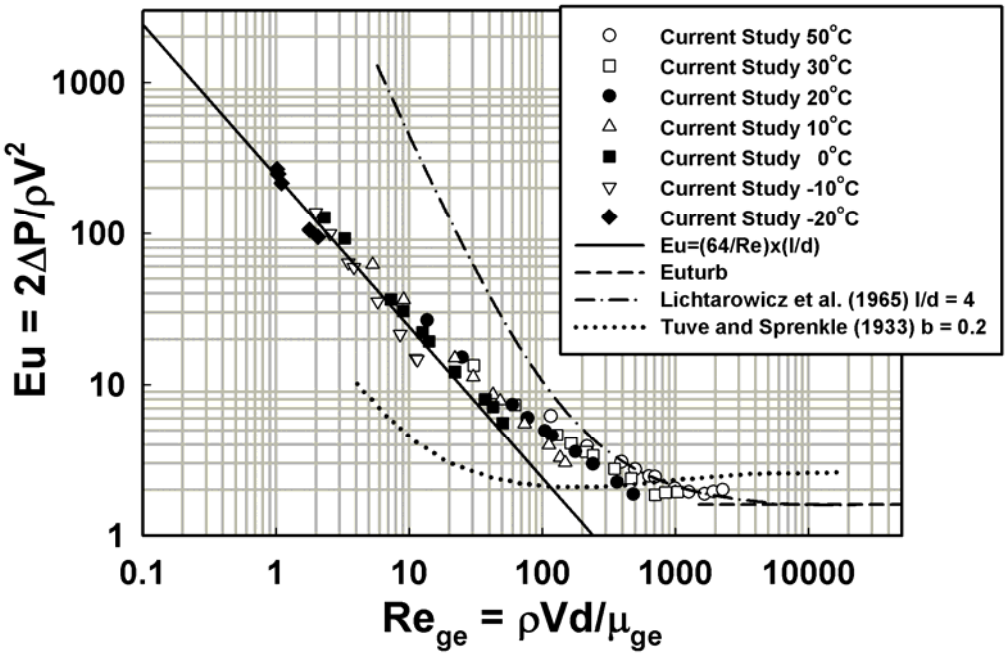

Figure 5.12 Eu versus Re for l/d = 4

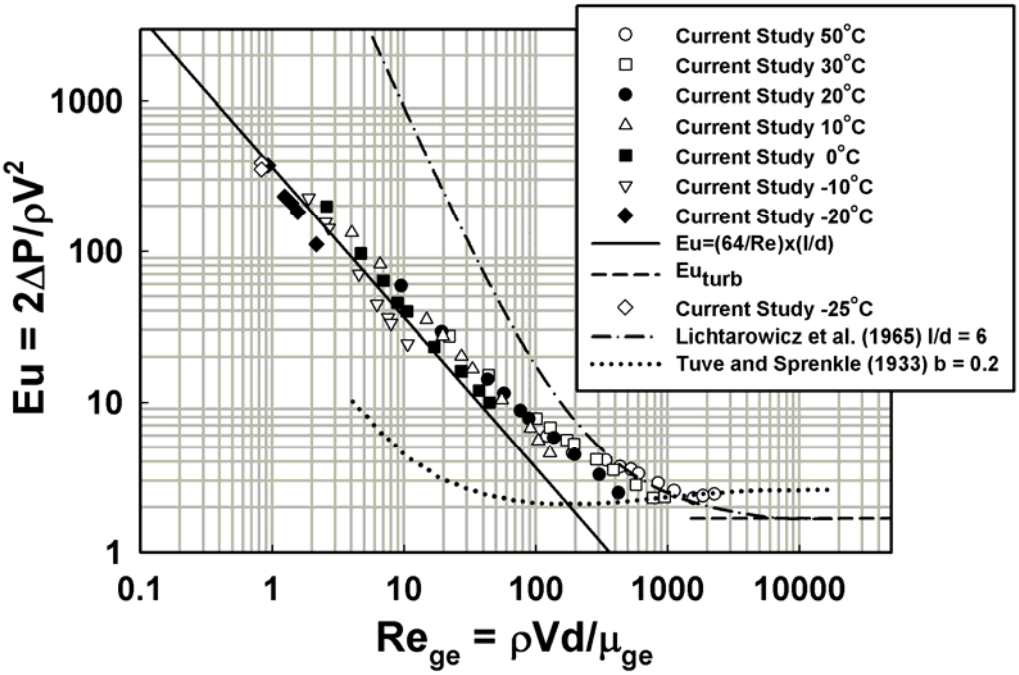

Figure 5.13 Eu versus Re for l/d = 6

5.5 Orifice Model Development

From the above discussion of the results, it can be said that the non-dimensional pressure drop can be represented as a function of the following parameters:

$$Eu = f\left(Re, \beta, l/d, \mu_r\right) \tag{5.3}$$

Based on the large bank of data collected in this study (although fewer points were taken in the fully turbulent regime), an empirical correlation can be developed using the insights discussed above and these non-dimensional parameters.

Several authors (Lichtarowicz *et al.* 1965; Hasegawa *et al.* 1997; Ramamurthi and Nandakumar 1999) have suggested that for laminar flow at low Reynolds numbers, the Euler number is composed of a viscous term and a constant as shown in Equation (5.4). The results from the current study also support this functional relationship between Eu and Re in the low Re, nearly constant slope region.

$$Eu = \frac{64}{Re}\left(l/d\right) + C \tag{5.4}$$

Dagan et al. (1982) also showed that orifice pressure drop and volumetric flow rate can be related as a function of aspect ratio for very small flow rates, as follows:

$$\Delta P = \frac{Q\mu}{r^3}\left[3 + \frac{8 \times \left(l/r\right)}{\pi}\right] \tag{5.5}$$

Equation (5.5) reduces to the solution obtained by Sampson (1891) for a zero thickness orifice. When this equation is non-dimensionalized, the following relationship is obtained between Euler number and Reynolds number:

$$Eu = \frac{1}{Re}\left[64 \times \left(l/d\right) + 12\pi\right] \tag{5.6}$$

In the above formulations, the first term may be viewed as representing viscous losses,

while the constant represents the additional pressure drop resulting from changes in the velocity profile at the entrance and exit to the orifice

It was also observed in the figures 5.5-5.13 that for extremely low Re (Re < ~6), the Eu-Re curve is steeper than the $Eu = 64 \times (l/d)/Re$ line, while for Re > 6, the linear Eu-Re dependence approximates the pipe flow equation. At still higher Re values, i.e., in the region approaching turbulence, Eu assumes a nearly constant value. Based on these observations, the data are divided in two regions for the development of the orifice flow model, with regressions conducted separately for each of the regions. For the data with Re < 6, using equation (5.6) as the basis, the effects of the orifice Reynolds number, aspect ratio, and viscosity ratio were incorporated into a generic equation of the following form:

$$Eu = \left(\frac{1}{Re_{ge}^{a}} \right) \left(64 \times (l/d)^{b} \mu_r{}^{c} + d \times \pi \right) \tag{5.7}$$

Here, constants a, b, c, and d are floating parameters to be determined through the regression analysis. The viscosity ratio was defined as the ratio of the actual viscosity for any data point to the reference viscosity of 0.1 kg/m-s at 20^{o}C.

For Re > 6, two different flow regimes, a linear Eu-Re region, and a constant Eu region, were combined to encompass whole range of the data. For the linear (laminar) region, Eu_{lam} was approximated as shown in equation (5.8).

$$Eu_{lam} = \left(\frac{1}{Re_{ge}^{A}} \right) \left(64 \times (l/d)^{B} \beta^{C} \mu_r{}^{D} + E \times \pi \right) \tag{5.8}$$

Here, A, B, C, D and E are determined through the regression analysis. As Re increases into the fully turbulent regime, the Eu vs. Re plots discussed above suggest that the Euler

number tends to a constant value. For the development of the high Re component of the model, this constant value was estimated by the following equation:

$$Eu_{turb} = \frac{1-\beta^4}{(C_d)^2} \tag{5.9}$$

In the absence of a large number of data points for the fully turbulent region, the work of Morris and Garimella (1998) was used to obtain the turbulent Eu limit in the present study. Thus, their correlations for the data of Ward-Smith (1971) for $\beta < 0.25$ (in this study, $\beta_{max} = 0.137$) were used to compute C_d as follows:

$$0.0 < l/d \leq 0.9: \quad C_d = 0.255\left[1 + (l/d)^{2.195}\right] + \frac{0.356}{(1+(l/d))^{0.140}} \tag{5.10}$$

$$0.9 < l/d \leq 2.5: \quad C_d = 0.876 - 0.0139(l/d) - \frac{0.084}{(l/d)} \tag{5.11}$$

$$2.5 < l/d \leq 9.5: \quad C_d = 0.292\left[1 + (l/d)^{-0.068}\right] + \frac{0.292}{(1+(l/d))^{0.150}} \tag{5.12}$$

Finally, for this range of Re (Re > 6), the laminar and turbulent Euler number equations were combined to yield the following expression:

$$Eu = \left[(Eu_{lam})^3 + (Eu_{turb})^3\right]^{1/3} \tag{5.13}$$

SigmaPlot software by SPSS Inc. (2004) was used to conduct the regression analysis for the two ranges of data and obtain the values of the correlation parameters shown in Tables 5.1 and 5.2.

The resulting correlations for the two different Re ranges are as follows:

- Re < 6

$$Eu = \left(\frac{1}{Re_{ge}^{1.203}}\right)\left(64 \times (l/d)^{1.502}\,\mu_r^{-0.470} + 36 \times \pi\right) \tag{5.14}$$

Table 5.1 Coefficients in Equation (5.7)

Parameter	Value
a	1.203 ± 0.035
b	1.502 ± 0.094
c	-0.470 ± 0.052
d	36 ± 1.626

Table 5.2 Coefficients in Equation (5.8)

Parameter	Value
A	0.882 ± 0.008
B	1.159 ± 0.034
C	0.075 ± 0.017
D	-0.334 ± 0.009
E	17.158 ± 0.086

- $Re > 6$

$$Eu = \left[\left\{ \left(\frac{1}{Re_{ge}^{0.882}} \right) \left(64 \times (l/d)^{1.159} \beta^{0.075} \mu_r^{-0.334} + 17.16 \times \pi \right) \right\}^3 + \left\{ \frac{1-\beta^4}{C_d^2} \right\}^3 \right]^{1/3} \quad (5.15)$$

Equation (5.14) has a correlation coefficient of $R^2 = 0.939$, with an average absolute deviation of 11%. Equation (5.15) has a correlation coefficient of $R^2 = 0.984$, with an average absolute deviation of 14%. As shown in Figure 5.14, the correlations predict 552 of the 642 data points (86%) to within ± 25% of the data obtained in the current study. The range of applicability of this set of correlations is as follows:

- $0.32 < l/d < 5.72$
- $0.02 < \beta < 0.137$
- $0.085 < Re_{ge} < 9677$

- $0.019 < \mu_{ge} < 9.589$ (kg/m-s)
- $0.19 < \mu_r < 95.89$

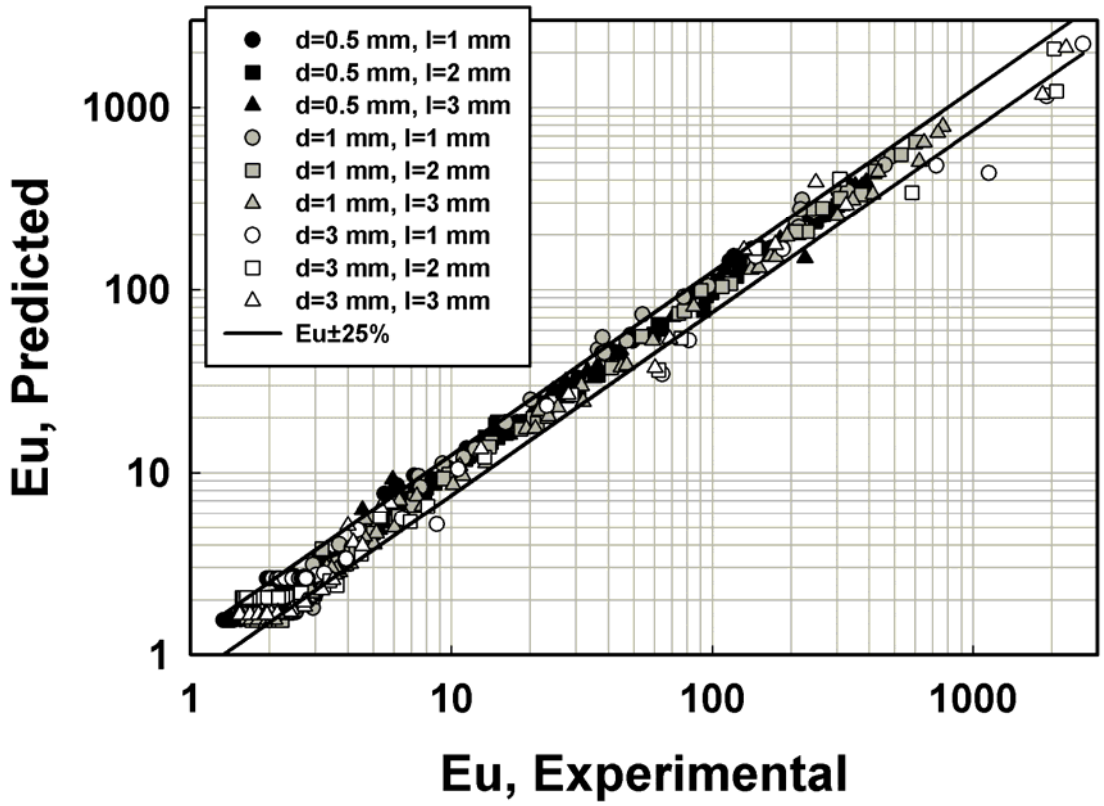

Figure 5.14 Experimental vs Predicted Euler Number

Comparisons between the predicted and experimental Euler numbers for each orifice tested in this study are shown in figures 5.15-5.23. Good agreement is seen between the data and the predictions for a large number of data. For the smaller Re values, very close agreement between the data and predictions can be seen with predictions being better for the larger aspect ratios. The agreement deteriorates to some extent, resulting in an underprediction of the data, in the moderate Re (transition) region, where the flow is

inherently unstable. At higher Re, in the progressively turbulent regime, the model over predicts the data for very small aspect ratios and under predicts the data for large aspect ratios. For smaller aspect ratios ($l/d < 1$), the turbulent limit calculated by Morris and Garimella (1998) is in close agreement with the experimental data. In general the model captures the trends in the experimental data very well.

The predictions of the model are used to demonstrate the effect of aspect ratio on the Eu-Re characteristics in figures 5.24-5.26. It is seen that an increase in aspect ratio increases Eu in the laminar region, whereas in the turbulent region, the effect is very small. It is also observed that the smallest Eu is obtained in the turbulent region at an aspect ratio of 2. The effect of varying viscosity is shown in figure 5.27, where Eu is plotted against Re for various viscosity ratios. For a given Re, an increase in viscosity ratio causes a decrease in Eu. Alternately, at higher viscosity ratios (lower temperatures), a similar Eu is obtained at smaller Re values. The influence of viscosity decreases as the Re increases.

Figures 5.28-5.30 show representative comparisons of experimental and predicted pressure drops in dimensional form. These figures clearly show that the model is successful in capturing the experimentally obtained results, and can be used reliably as a design tool for the analysis and design of fluid loops in practical hydraulic systems.

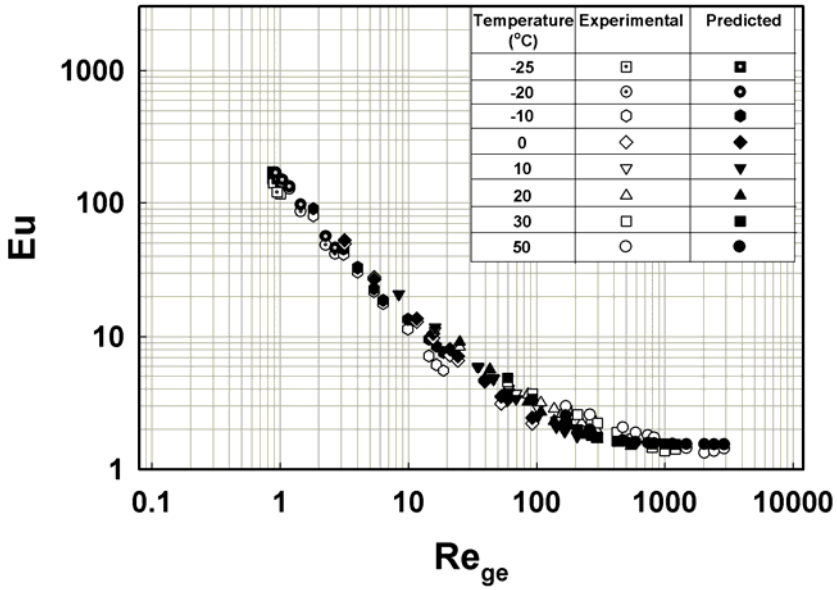

Figure 5.15 Predicted and Experimental Euler Number for 0.5 mm Diameter, 1 mm Thick Orifice

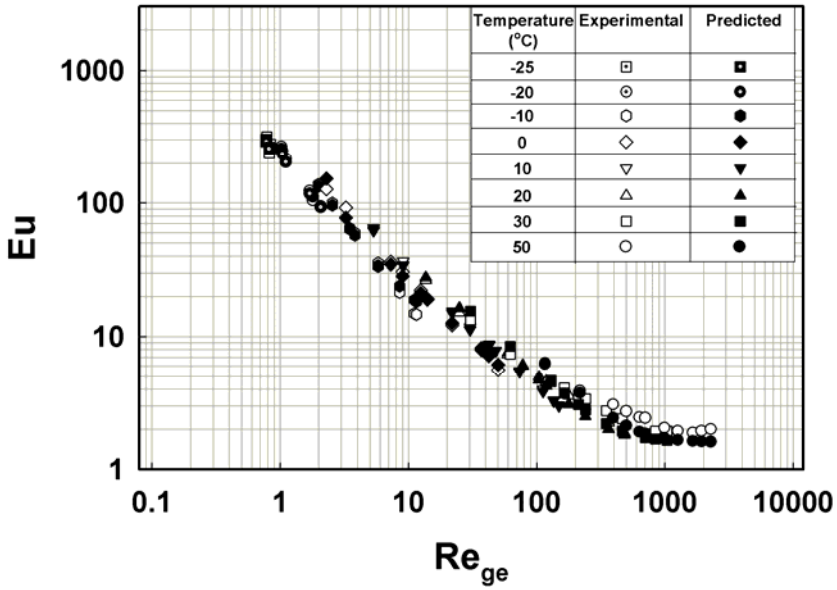

Figure 5.16 Predicted and Experimental Euler Number for 0.5 mm Diameter, 2 mm Thick Orifice

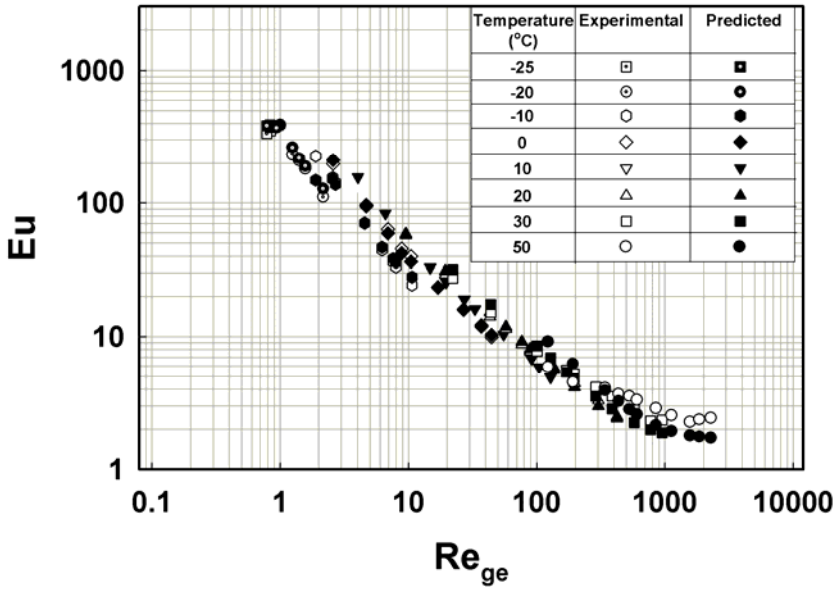

Figure 5.17 Predicted and Experimental Euler Number for 0.5 mm Diameter, 3 mm Thick Orifice

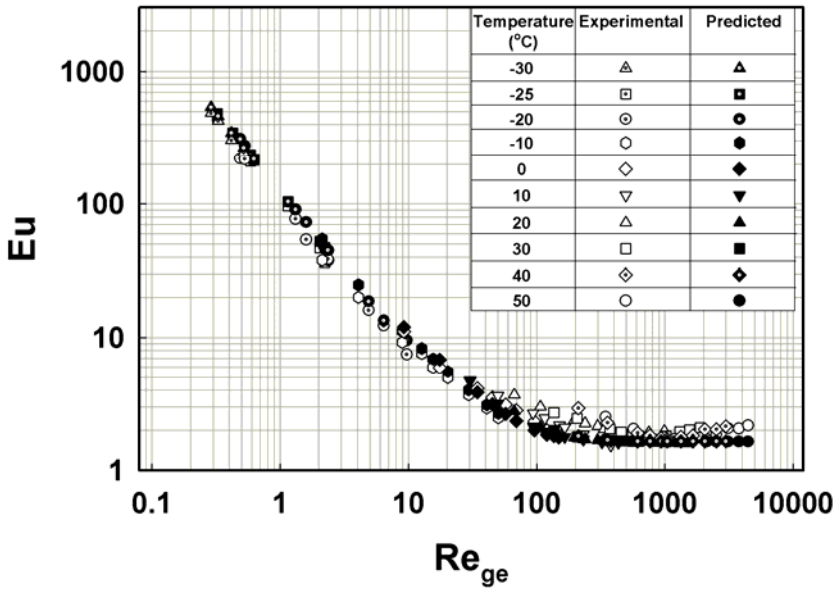

Figure 5.18 Predicted and Experimental Euler Number for 1 mm Diameter, 1 mm Thick Orifice

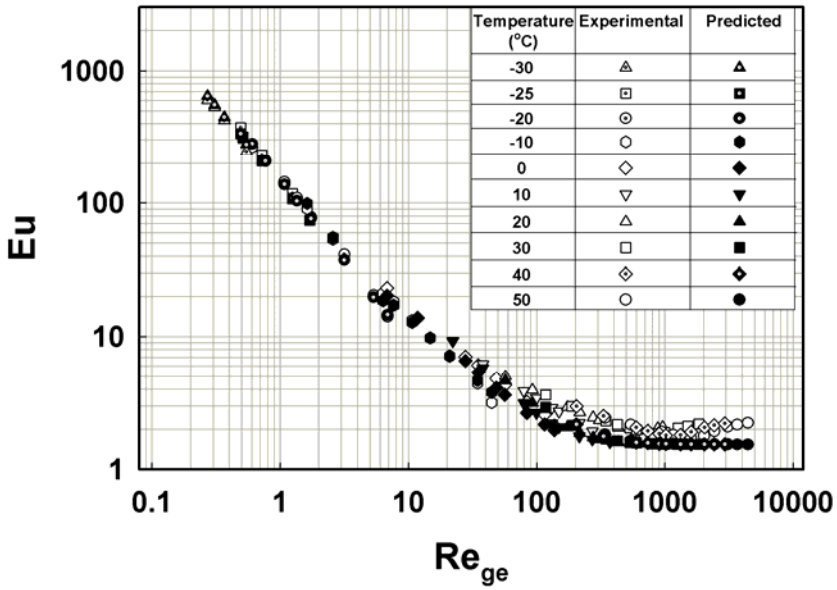

Figure 5.19 Predicted and Experimental Euler Number for 1 mm Diameter, 2 mm Thick Orifice

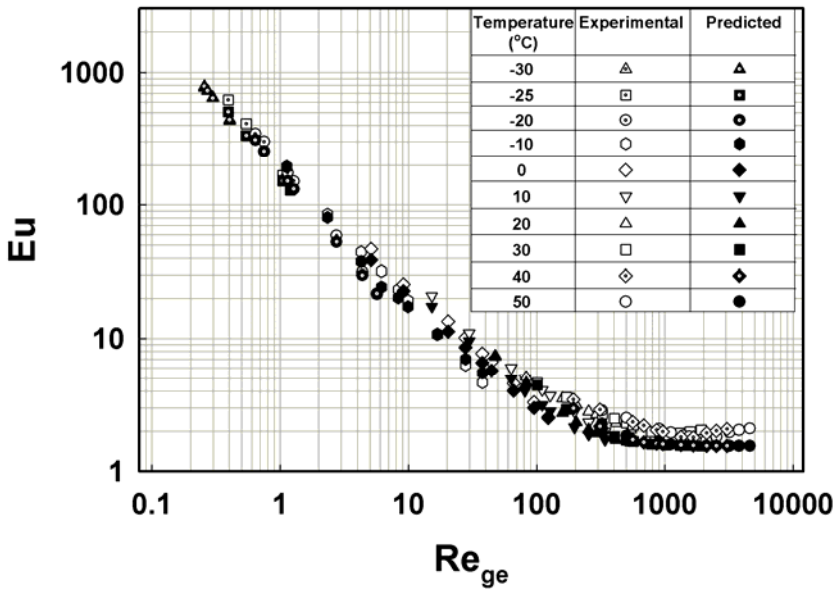

Figure 5.20 Predicted and Experimental Euler Number for 1 mm Diameter, 3 mm Thick Orifice

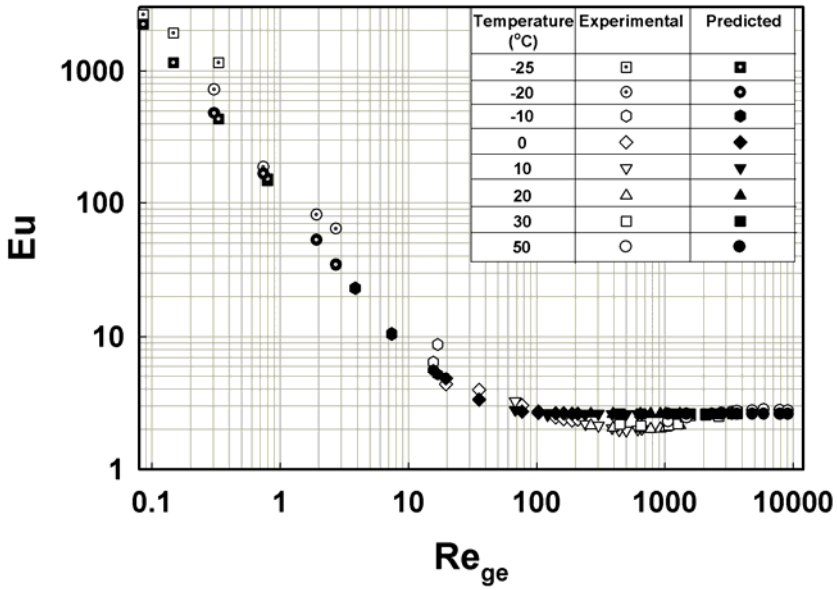

Figure 5.21 Predicted and Experimental Euler Number for 3 mm Diameter, 1 mm Thick Orifice

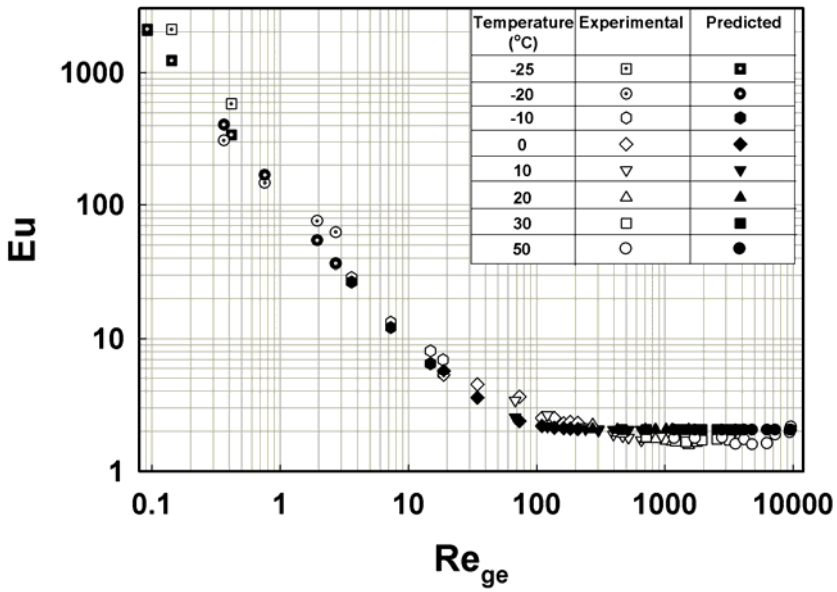

Figure 5.22 Predicted and Experimental Euler Number for 3 mm Diameter, 2 mm Thick Orifice

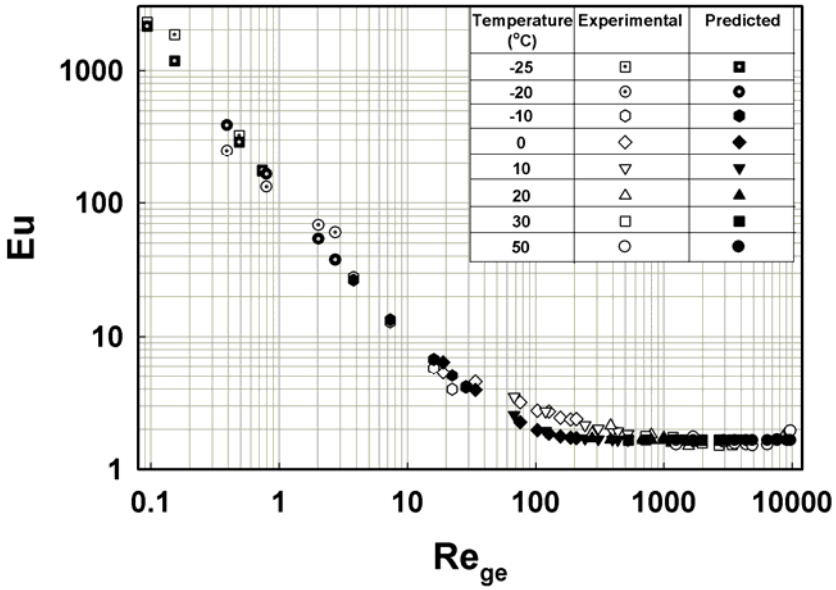

Figure 5.23 Predicted and Experimental Euler Number for 3 mm Diameter, 3 mm Thick Orifice

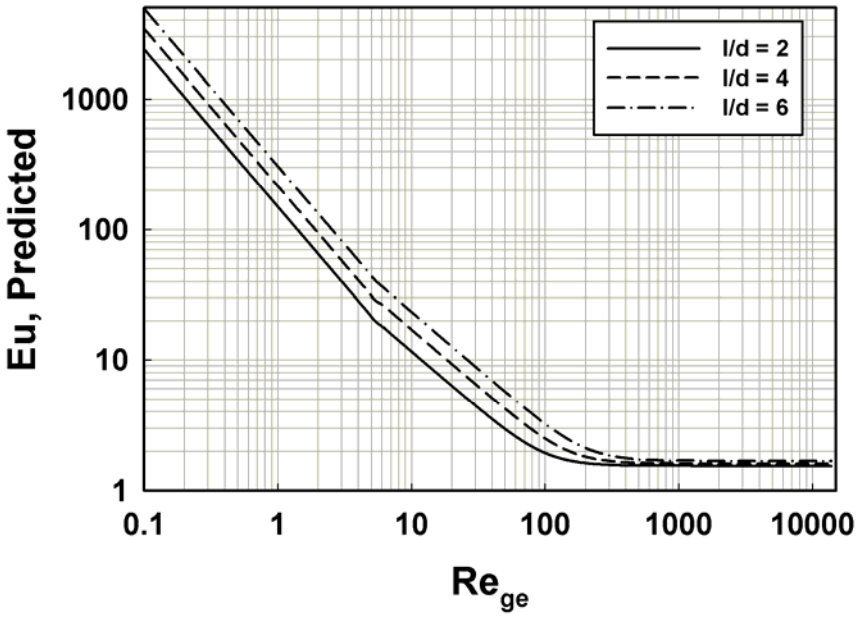

Figure 5.24 Model Predictions for Diameter Ratio of 0.023

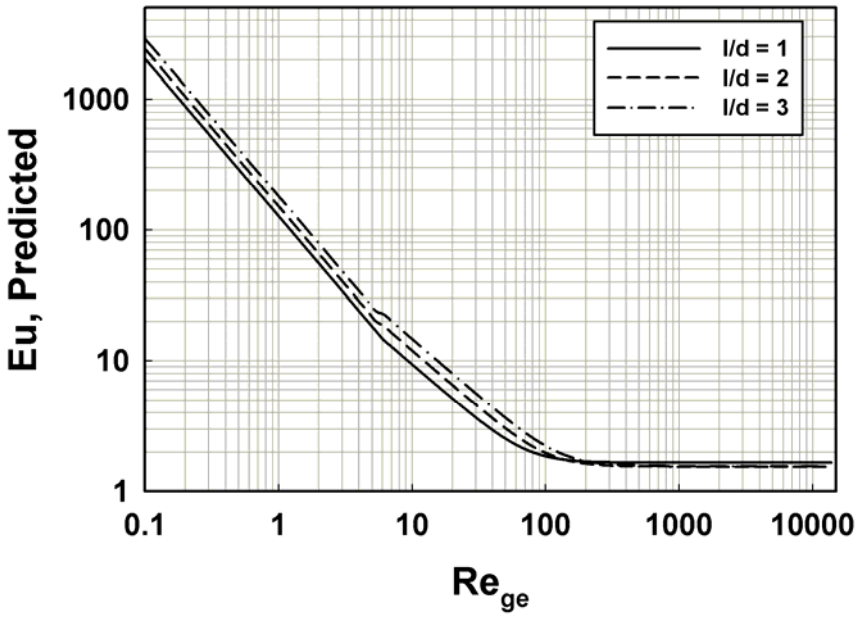

Figure 5.25 Model Predictions for Diameter Ratio of 0.044

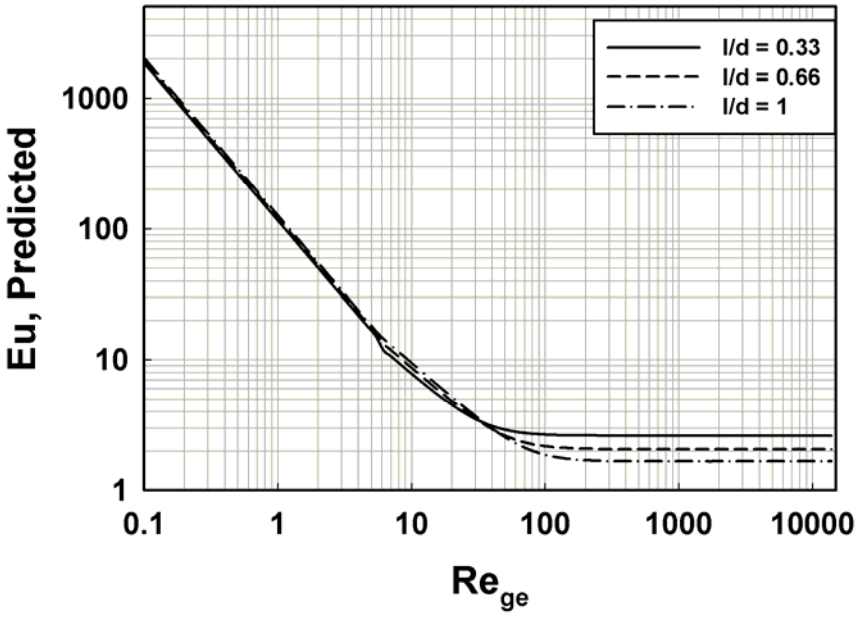

Figure 5.26 Model Predictions for Diameter Ratio of 0.137

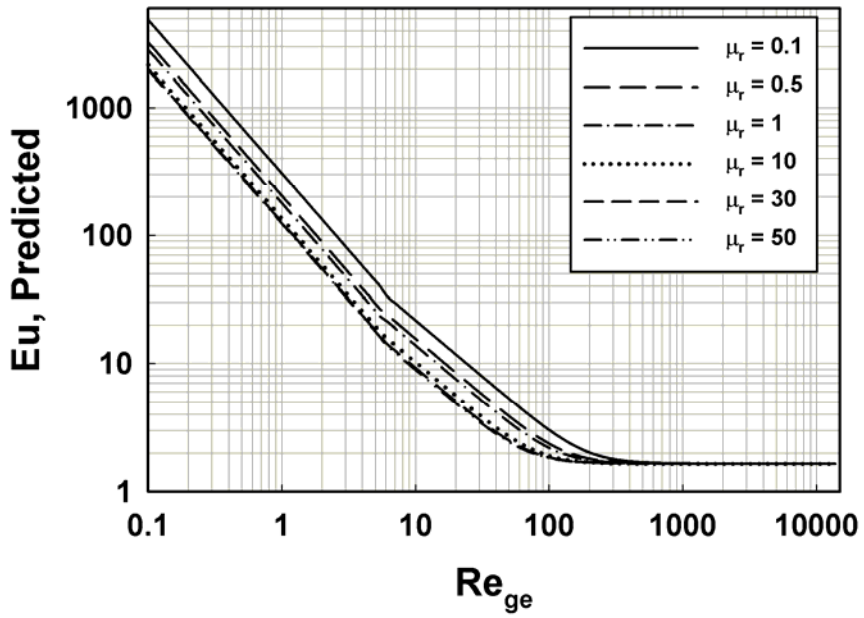

Figure 5.27 Model Predictions for Various Viscosities (1mm Diameter, 1 mm Thick Orifice)

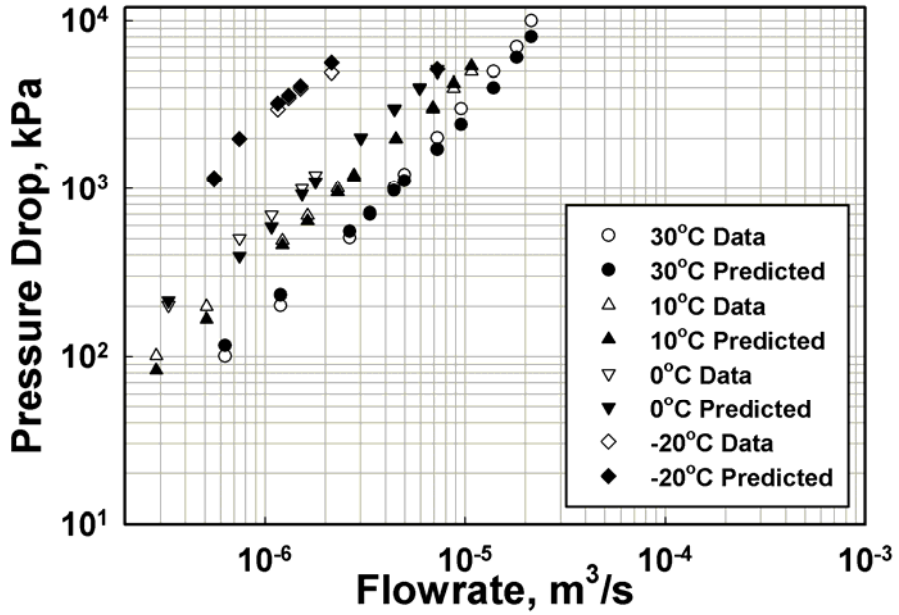

Figure 5.28 Experimental and Predicted Pressure Drops (0.5 mm Diameter, 3 mm Thick; l/d=6)

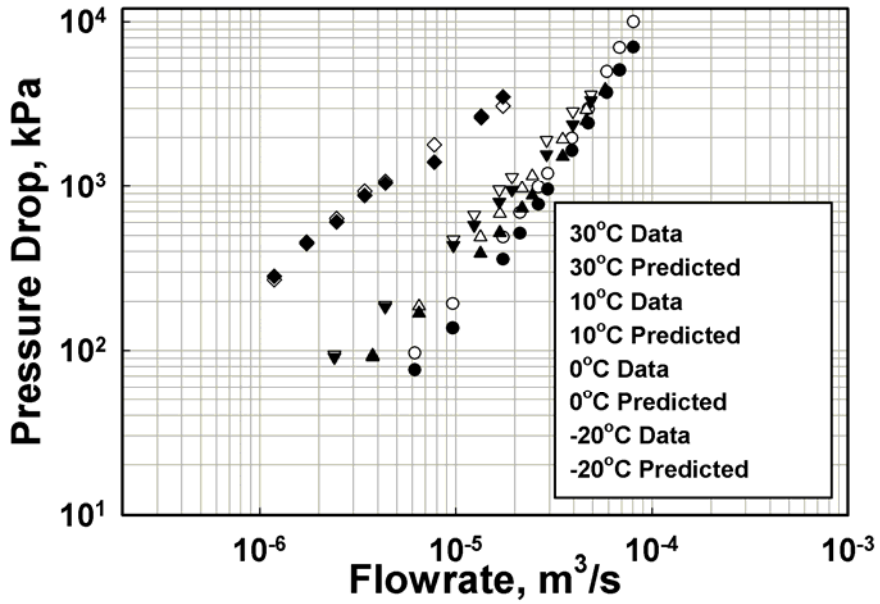

Figure 5.29 Experimental and Predicted Pressure Drops (1 mm Diameter, 2 mm Thick; l/d=2)

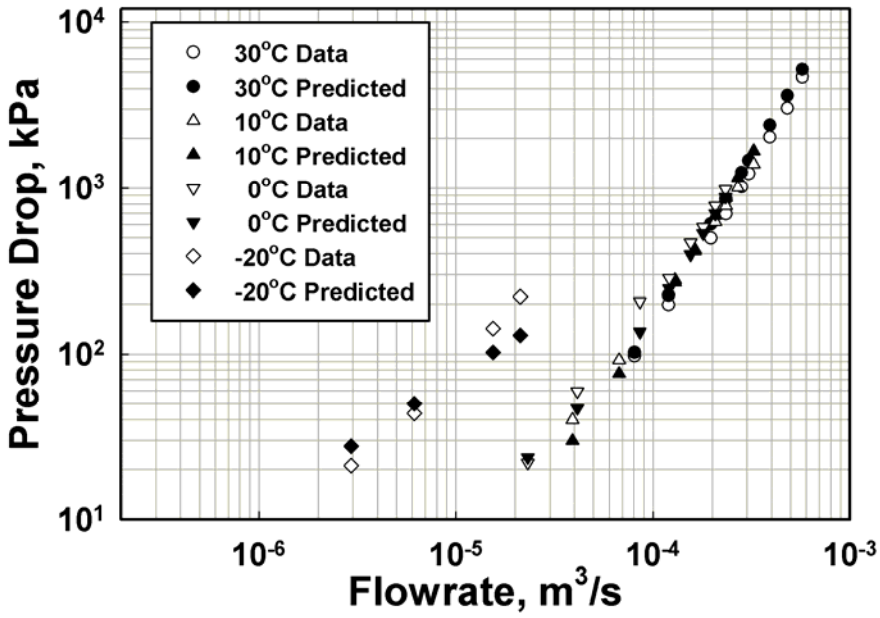

Figure 5.30 Experimental and Predicted Pressure Drops (3 mm Diameter, 2 mm Thick; l/d=0.66)

6. CONCLUSIONS AND RECOMMENDATIONS

6.1 Conclusions

Pressure drop and flow characteristics for 9 small diameter orifices were investigated experimentally in this study. Orifices of three different diameters (0.5, 1, and 3 mm) with three different thicknesses (nominally 1, 2, and 3 mm) each, covered diameter ratios of $0.023 \leq \beta \leq 0.137$ and aspect ratios of $0.33 < l/d < 6$. Tests were conducted for pressure drops ranging from 100 kPa (14.5 psi) to 5,000 kPa (725 psi) for a temperature range of $-30 \leq T \leq 10^{o}C$. The flow rates for these pressure drops covered generalized Reynolds numbers from 0.09 to 677. However, analysis is presented for a much wider range of data including those of Mincks (2002). Therefore the analysis spans an Re range of 0.09 to 9677. This brings continuity and completeness to the analysis.

The fluid investigated here is highly viscous; therefore, most of the data fall in the laminar and transition regions even at very large flow rates. Non-dimensional analysis shows that in the laminar range (where the log(Eu)-log(Re) dependence is linear), an increase in the aspect ratio results in an increase in the Euler number for similar Reynolds numbers. The influence of aspect ratio diminishes as the Re approaches the transition region, and Eu tends to assume a constant value in turbulent region. However, at higher Reynolds numbers, the Euler number exhibits a minima at an aspect ratio of about two. Aspect ratios greater or lesser than this value result in increasing Euler numbers.

Fluid temperature also affects the orifice flow characteristics significantly. As was discussed in section 5.4, increasing temperature in the laminar region results in an increase in the Euler number for similar Reynolds numbers. In other words, similar Eu

values are obtained at higher Re as temperature increases. The extent of the laminar region increases with an increase in the temperature, as evidenced by the location of the minima in the Eu-Re plots. This is explained in terms of fluid viscosity. As temperature increases, the viscosity of the fluid decreases. Thus, to maintain the same Reynolds number at a higher temperature, the velocity must also decrease where the density of the fluid remains almost constant. This lower velocity, through its inverse square effect on Euler number ($Eu \propto 1/V^2$), will result in an increased Euler number. However, due to the aforementioned increase in the extent of the laminar region at higher temperatures, this effect is coupled with transition to turbulent behavior at increasing Re values, where the trends are not as clear. Additional data at higher Reynolds numbers are needed for a better understanding of the corresponding dependence on temperature (and therefore properties).

The test fluid also shows non-Newtonian behavior at extremely low temperatures. The fluid viscosity now depends on shear rate as well as temperature. It was found that both the shear rate and temperature affect the viscosity in similar manner. The shear rates observed at the orifice were large for the tests conducted. The net effect of these large shear rates is to lower viscosities. Since other properties were independent of shear rate, this decrease in viscosity resulted in increased Re for similar flow rates.

From the insight gained from these experimental results, a two-region empirical model to predict non-dimensional pressure drop given the orifice geometry and flow conditions was developed using regression analysis. The model predicts 552 of 642 data points within ±25%. The model developed in non-dimensional form can be used to

predict pressure drops for the analysis and design of hydraulic systems over a wide range of flow rates, temperatures and orifice geometries.

6.2 Recommendations

Although this study covered a wide range of viscosities, to understand the effect of fluid properties on flow behavior in a comprehensive manner, more data are needed, especially at higher Reynolds numbers and also at very low temperatures. It is apparent from this study that highly viscous fluids do not behave as predicted by conventional theories of orifice flow. The influence of non-Newtonian behavior and varying properties could be better understood by extending the test conditions to more combinations of geometry, flow rate and temperature. This would require substantially upgraded test facilities that would address the much higher pumping power, viscous fluid cooling, and system pressure requirements. Flow instabilities at very low flow rates was another challenge in this study, leading to difficulties in maintaining steady flows at the very low temperature, small pressure drop cases. In a few instances, the operating conditions were also out of the optimal accuracy ranges of the high precision pressure transducers and flow meters.

Viscous heating may play an important role in determining the pressure drop characteristics, especially at very low temperatures where a small increase in temperature can cause a significant variation in viscosity of the fluid. It was observed in certain instances that the temperature increased by up to 10^{o}C along the test section – suggesting that a model that incorporates viscous heating, substantiated by localized measurements could yield more improvement in the model.

The results also depend heavily on the understanding and accuracy of the fluid properties, particularly at conditions where the fluid becomes non-Newtonian. More studies on properties such as power law and consistency index will improve the modeling of non-Newtonian behavior and yield commensurate benefits in the prediction of the pressure-flow characteristics.

APPENDIX A

A1 Curve-Fits for Blank Orifice Data

Experimentally measured pressure drops across the test section also included pressure drops due to the test section plumbing. To account for these, experiments were conducted with an orifice of diameter equal to the pipe diameter. Pressure drops were measured for a wide range of flow rates at each temperature across this blank orifice. These measured pressure drops in the test section plumbing were then used to generate a curve fit for the estimation of pressure drop for any given flow rate as shown in Equation (A.1):

$$\Delta P = aQ^b \qquad \text{(A.1)}$$

Where:

Q = flow rate through the orifice, m^3/s

ΔP = pressure drop, kPa

Table A.1 shows values of these coefficients for various temperatures under consideration in this study ($T \geq 20^oC$, Mincks (2002)).

Table A.1 Coefficients in Equation (A.1)

Temperature (°C)	A	B
50	5.768×10^6	1.314
40	5.808×10^6	1.267
30	3.679×10^5	0.947
20	2.892×10^6	1.100
10	3.332×10^6	1.075
0	3.709×10^6	1.009
-10	4.627×10^6	1.170
-20	7.916×10^6	0.903
-25	1.981×10^6	0.905
-30	5.660×10^6	0.940

A polynomial curve fit was used for the larger 3 mm diameter orifice for the warm temperature cases as shown below. (This was necessary due to modifications to test facility that enabled testing at higher flow rates.)

$$T = 20^{o}C : \Delta P = -3.65 + \left(1.01\times10^{6}\right)Q - \left(8.25\times10^{8}\right)Q^{2} + \left(5.10\times10^{12}\right)Q^{3} + \left(-3.83\times10^{15}\right)Q^{4} \quad \text{(A.2)}$$

$$T = 30^{o}C : \Delta P = -1.98 + \left(3.99\times10^{5}\right)Q - \left(8.78\times10^{8}\right)Q^{2} + \left(1.78\times10^{12}\right)Q^{3} + \left(-2.28\times10^{15}\right)Q^{4} \quad \text{(A.3)}$$

$$T = 50^{o}C : \Delta P = \left(4.59\times10^{7}\right)Q^{1.56} \quad \text{(A.4)}$$

A2 Test Section Plumbing Loss Estimation

The extraneous pressure losses due to test section plumbing were also computed using frictional and minor loss expressions from the literature. The data point used for this demonstration is labeled 11-35_20, which represents data for the 1 mm diameter, 1 mm thick orifice plate, with an imposed pressure drop of 35 bar and an inlet temperature of -20°C. 120 readings were taken for each data point over a two-minute time period (one per second). Table A.2 shows the average values for this data point while Table A.3 shows the same values as in Table A.2, but in S. I. units.

Table A.2 Raw Data Used in Calculations for Data Point 11-35_20

Temperature In	Temperature Out	Pressure In	Pressure Out	Differential Pressure	Flow Rate
(°C)	(°C)	(psia)	(psia)	(psid)	(gpm)
-20.07	-19.47	468.32	197.14	294.2	0.378

Table A.3 Raw Data used in Calculations for Point 11-35_20 (S.I. Units)

Temperature In	Temperature Out	Pressure In	Pressure Out	Differential Pressure	Flow Rate
(°K)	(°K)	(kPa)	(kPa)	(kPa)	(m^3/s)
253.08	253.68	4701	1450	3495	2.383E-05

The velocity through each segment was calculated by dividing the volumetric flow rate by the cross-sectional area, as follows:

$$V_{seg} = \frac{Q}{A_{seg}} \tag{A.5}$$

The dimensions for each segment of Figure 3.4 and the resulting velocities are shown in Table A.4 while the oil properties for this test condition are shown in Table A.5. The properties for the inlet and outlet segments were calculated at the inlet and outlet temperatures and pressures, respectively. The properties at the orifice were calculated at the average pressure and temperature. The calculation of the viscosity accounted for the shear rate at each segment. Details of viscosity calculation were presented in section 4.1. The Reynolds numbers for each segment were then calculated as follows:

$$Re_{seg,ge} = \frac{\rho V_{seg} d_{seg}}{\mu_{ge}} \tag{A.6}$$

Density was provided by the fluid supplier. (In Table A.5, the viscosity at the orifice is lower than that at the outlet despite the lower temperature because the shear rate at the orifice is much higher than at any other segment of the test section.)

The total measured pressure drop therefore consists of the pressure drop due to the orifice, pressure drops in small straight sections of upstream and downstream piping

(between the pressure taps), and losses due to expansions and/or contractions into and out of these individual segments.

Table A.4 Test Section Dimensions and Frictional Pressure Drop Results (1 mm Diameter, 1 mm Thick Orifice)

Segment	Length (m)	Diameter (m)	Area (m^2)	Velocity (m/s)	Re_{eg}	f	ΔP_f (kPa)
1	0.152	.0109	9.369E-05	0.255	0.708	90.42	37.25
2	0.152	.0085	5.653E-05	0.419	0.951	67.28	95.86
3	0.026	.0104	8.518E-05	0.281	0.747	85.66	7.61
4	0.015	.0183	2.627E-04	0.091	0.410	156.3	0.47
5	0.019	.0295	6.818E-04	0.035	0.254	252.3	0.09
6	0.152	.0228	4.063E-04	0.058	0.328	194.9	2.00
O1	0.001	.0010	8.059E-07	29.56	9.72	6.584	**2639**
O2	0.004	.0052	2.109E-05	1.131	1.772	36.12	13.65
7	0.152	.0207	3.366E-04	0.071	0.386	165.7	2.75
8	0.019	.0295	6.818E-04	0.035	0.271	236.3	0.08
9	0.015	.0183	2.627E-04	0.091	0.437	146.4	0.45
10	0.026	.0104	8.518E-05	0.281	0.795	80.52	7.14
11	0.152	.0085	5.653E-05	0.419	1.011	63.33	90.00
12	0.152	.0109	9.369E-05	0.255	0.753	84.95	34.92

Note: Segment O1 refers to the orifice while segment O2 refers to the back-cut in the orifice plate.

Table A.5 Fluid Properties at Temperatures and Pressures Listed

	Temperatures (^oC)	Pressure (kPa)	Density (kg/m^3)	Viscosity (kg/m-s)
Inlet	-20.07	4701	904	3.266
Orifice	-19.77	3075.5	903	2.782
Outlet	-19.47	1450	902	3.423

It should be noted that the flow through these small segments of piping is not fully developed, as the length of these segments is very small. However, since there are no readily available expressions for pressure drops in such segments, the corresponding friction factor for fully developed flow through straight circular tubes was used to provide an estimate of these losses. The accuracy of these estimates is not very significant, because as will be shown later, the pressure drops in these segments are extremely small fractions of the orifice pressure drop for most of the data.

The Darcy form of the friction factor correlation by Churchill (1977) was used to calculate the friction factor for each pipe segment. As explained in section 4.1, expressions from Munson et. al. (1998) were used to calculated minor loss coefficients as necessary. Thus friction losses were computed for each segment using equation A.7.

$$\Delta P_{f,seg} = \frac{1}{2} f_{seg} \rho V_{seg}^2 \frac{L_{seg}}{d_{seg}} \tag{A.7}$$

And minor losses were computed as:

$$\Delta P_{minor} = \frac{1}{2} K_L \rho V^2 \tag{A.8}$$

Table A.6 shows the area ratios used to calculate the loss coefficients and the resulting pressure drops.

Once the frictional and minor losses were calculated for each segment, the total estimated pressure drop due to the test section piping was calculated by summing the frictional losses with the minor losses (excluding the pressure drop due to the orifice itself, $\Delta P_{f,O1}$). It should be noted that the pressure drops due to the orifice back-cut ($\Delta P_{f,O2}$ and $\Delta P_{minor,B}^{*}$) are considered to be part of the system piping when calculating the pressure drop only due to the orifice. For this case, the estimated value for the test section pressure drop was found to be 293 kPa while the experimental value was found to be 528 kPa (including estimates for the back-cut losses.) Extraneous losses (measured as well as estimated) for the whole range of conditions tested are available in Chapter 4 (Figure 4.5), and show good agreement between these values.

To determine the pressure drop across the orifice, the experimentally determined pressure loss of 528 kPa was subtracted from the measured differential pressure drop of 3495 kPa to yield a value of 2967 kPa. Thus, in this case, the extraneous pressure drop is 15.1 % of the measured pressure drop. It should be noted that such large extraneous pressure drops were observed only for low temperatures. For the higher temperature cases, the extraneous pressure losses were very small (of the order of 1-2%) of the orifice pressure drop.

The Euler number for the orifice was calculated, as shown below, to be 7.485:

$$Eu = \frac{\Delta P}{\frac{1}{2}\rho V_O^2}. \qquad (A.9)$$

Table A.6 Dimensions and Results for Minor Losses

Sudden Change	Area Ratio	K_L	Segment Velocity (m/s)	ΔP_{minor} (kPa)
B1	0.664	0.11	0.280	0.009
B2	0.324	0.46	0.091	0.016
B3	0.385	0.38	0.034	0.001
C1	0.596	0.17	0.058	0.0003
B*	0.063	0.88	2.911	0.506
B4	0.494	0.26	0.182	0.001
C2	0.385	0.33	0.231	0.001
C3	0.324	0.37	0.721	0.013
C4	0.664	0.12	1.093	0.009

Note 1: B stands for a sudden expansion and C stands for a sudden contraction.
Note 2: B^* is for the orifice plate back-cut and represents either a sudden contraction (1 mm diameter, 3 mm thick orifice) or a sudden expansion (all other orifices) into the downstream piping. For this example, it represents a sudden expansion.

A3 Error Analysis

Uncertainties in the dimensionless variables discussed in the previous section were computed using an error-propagation approach (Taylor and Kuyatt 1993). Equations for the Reynolds and Euler numbers in terms of measured parameters and properties are shown below:

$$\mathrm{Re} = \frac{4Q\rho}{\pi D \mu_{ge}} \tag{A.10}$$

$$Eu = \frac{\pi^2 D^4 \Delta P}{8\rho Q^2} \tag{A.11}$$

The uncertainties are demonstrated below using the same data point that was discussed above for the evaluation of orifice pressure drop. The uncertainty in the Reynolds number for the orifice is given by:

$$U_{Re}^2 = \left(\frac{\partial Re}{\partial Q} U_Q\right)^2 + \left(\frac{\partial Re}{\partial D} U_D\right)^2 + \left(\frac{\partial Re}{\partial \rho} U_\rho\right)^2 + \left(\frac{\partial Re}{\partial \mu} U_{\mu_{ge}}\right)^2 \tag{A.12}$$

$$\frac{\partial Re}{\partial Q} = \frac{4\rho}{\pi D \mu_{ge}} = \frac{4(903)}{\pi(.001)(.2.782)} = 4.08\times10^5 \frac{s}{m^3} \tag{A.13}$$

$$\frac{\partial Re}{\partial D} = -\frac{4Q\rho}{\pi D^2 \mu_{ge}} = -\frac{4\left(2.383\,x\,10^{-5}\right)(903)}{\pi(.001)^2(2.782)} = -9.59\times10^3\ m^{-1} \tag{A.14}$$

$$\frac{\partial Re}{\partial \rho} = \frac{4Q}{\pi D \mu_{ge}} = \frac{4\left(2.383x10^{-5}\right)}{\pi(.001)(2.782)} = 1.08\times10^{-2} \frac{m^3}{kg} \tag{A.15}$$

$$\frac{\partial Re}{\partial \mu_{ge}} = -\frac{4Q\rho}{\pi D \mu_{ge}^{\ 2}} = -\frac{4\left(2.383\,x\,10^{-5}\right)(903)}{\pi(.001)(2.782)^2} = -3.494 \frac{m\cdot s}{kg} \tag{A.16}$$

The measurement uncertainties for temperature, pressure, and flow rate are given in Table A.7. For the data point 11-35_20, the flow rate uncertainty was 7.148×10^{-8} m^3/s.

Table A.7 Uncertainties in Temperature, Pressure, and Flow Rate Measurements

U_D	± 0.0025 mm for each orifice plate	
U_T	± 0.6°C for all cases	
U_{AP} (Absolute Pressure)	± 10.342 kPa for all readings	
$U_{DP,m}$ (Differential Pressure)	1 and 2 bar cases	5 bar and greater
	± 0.948 kPa	± 7.757 kPa
U_Q	-30°C < T < 20°C	30°C < T < 50°C
	0.3% of reading	0.5% of reading

Details of the calculation of uncertainties in density and viscosity are provided in the Appendix A4 and A5 respectively. The resulting uncertainties, U_ρ (based on temperature and pressure measurement uncertainties and the uncertainties in the property calculation from given conditions) and U_μ (based on shear rate and temperature) for this data point were:

$$U_\rho = \sqrt{(0.624)^2 + ((0.005)(903))^2} = \pm 4.558 \frac{kg}{m^3} \quad (A.17)$$

$$U_{\mu_{ge}} = \sqrt{(0.195)^2 + \left(\left(3.3\times10^{-6}\right)\times(350.2)\right)^2} = \pm 0.196 \frac{kg}{m-s} \quad (A.18)$$

Thus, the uncertainties in properties are ± 0.50% for density and ± 7.0% for viscosity. The other two uncertainties in the Reynolds number equation were:

$$U_Q = 0.003(2.383E-05) = \pm 7.148\times10^{-8} \frac{m^3}{s} \quad (A.19)$$

$$U_D = \pm 2.54\times10^{-6}\ m \quad (A.20)$$

The resulting uncertainty in the Reynolds number (Re = 9.72) is given by:

$$U_{Re} = \sqrt{(0.0291)^2 + (-0.024)^2 + (0.049)^2 + (-0.6823)^2} = \pm 0.685 \quad (A.21)$$

Thus, the uncertainty in the Reynolds number is 7.06 %.

The uncertainty in the Euler number for the orifice is calculated as follows:

$$U_{Eu}^2 = \left(\frac{\partial Eu}{\partial Q}U_Q\right)^2 + \left(\frac{\partial Eu}{\partial D}U_D\right)^2 + \left(\frac{\partial Eu}{\partial \rho}U_\rho\right)^2 + \left(\frac{\partial Eu}{\partial \Delta P}U_{DP}\right)^2 \quad (A.22)$$

$$\frac{\partial Eu}{\partial Q} = -\frac{\pi^2 D^4 \Delta P}{4\rho Q^3} = -\frac{\pi^2 (.001)^4 (2953\times10^3)}{4(903)(2.383\times10^{-5})^3} = -6.28\times10^5 \frac{s}{m^3} \quad (A.23)$$

$$\frac{\partial Eu}{\partial D} = \frac{\pi^2 D^3 \Delta P}{2\rho Q^2} = \frac{\pi^2 (.001)^3 (2953\times10^3)}{2(903)(2.383\times10^{-5})^2} = 2.95\times10^4\ m^{-1} \quad (A.24)$$

$$\frac{\partial Eu}{\partial \rho} = -\frac{\pi^2 D^4 \Delta P}{8\rho^2 Q^2} = -\frac{\pi^2 (.001)^4 (2953\times10^3)}{8(903)^2 (2.383\times10^{-5})^2} = -8.29\times10^{-3}\ \frac{m^3}{kg} \quad (A.25)$$

$$\frac{\partial Eu}{\partial \Delta P} = \frac{\pi^2 D^4}{8\rho Q^2} = \frac{\pi^2 (.001)^4}{8(903)(2.383\times10^{-5})^2} = 2.53\times10^{-6}\ Pa^{-1} \quad (A.26)$$

For the uncertainty in differential pressure, it was necessary to also account for the uncertainty in the extraneous plumbing losses that are subtracted from the measured differential pressure to obtain the orifice pressure drop. Because these losses were measured using a blank orifice in place of an orifice plate, it is possible that the system losses without the orifice plate would be somewhat different from the losses in the presence of the orifice plate due to differences in the flow mechanisms caused by the orifice plate. To account for these potential differences, a conservative estimate of ± 25% was used for the uncertainty in the plumbing losses. Therefore, the uncertainty in the differential pressure was found as follows:

$$U_{\Delta P} = \sqrt{U_{\Delta P,m}^2 + U_{\Delta P,sys}^2} = \sqrt{(7.757)^2 + ((0.25)(527.9))^2} = \pm 135.6\ \text{kPa or } 4.50\ \% \quad (A.27)$$

Combining all these uncertainties results in the following uncertainty in Euler number:

$$U_{Eu} = \sqrt{(-0.045)^2 + (0.075)^2 + (-0.034)^2 + (0.34)^2} = 3.57\times10^{-1} \quad (A.28)$$

The resulting uncertainty in the Euler number is 4.77 %.

Table A.8 gives the range of the Reynolds and Euler number uncertainties for the current study including those obtained by Mincks (2002). It should be noted here that Reynolds number uncertainties were less than 10% for more than 95% of data points. Uncertainties greater than 10% were observed at the extreme points where either temperature or flow rate control was difficult. For the 3 mm orifice, the uncertainties in Euler number at low

temperatures are very high, in some cases even more than 100%. At these low temperatures and relatively high flow rates, the pump operation was not steady. This results in a large uncertainty in the plumbing loss which accounts for a much larger portion of the measured pressure drop in these cases, and in turn causes large uncertainties in Euler number.

Table A.8 Range of Reynolds Number and Euler Number Uncertainties for the Three Orifice Diameters in the Current Study

Re Range	Uncertainty in Re	Eu Range	Uncertainty in Eu
0.5 mm Diameter			
$0.78 < Re_{ge} < 2892$	$2.66 < U_{Re} < 17.67\%$	$1.3 < Eu < 391$	$2.09 < U_{Eu} < 2.72\%$
1 mm Diameter			
$0.26 < Re_{eg} < 4602$	$2.69 < U_{Re} < 12.69\%$	$1.7 < Eu < 766$	$1.30 < U_{Eu} < 8.0\%$
3 mm Diameter			
$0.09 < Re_{eg} < 9677$	$2.53 < U_{Re} < 8.392\%$	$1.5 < Eu < 2636$	$1.88 < U_{Eu} < 129.5\%$

A4 Uncertainties in Density

The density of the test fluid depended on the temperature and pressure. Figure A.1 shows effect of temperature and pressure on the density. From this figure, it can be seen that the density decreases as temperature increases for a constant pressure. For a constant temperature, an increase in pressure results in an increase in the density. The fluid density was determined using a FORTRAN subroutine provided by the fluid supplier. To determine the uncertainty in the density values provided by this program, the uncertainty

in the measured pressure and temperature must be taken into account. This was accomplished by creating two representative data sets with pressure and temperature values that spanned the entire range of recorded values. Both data sets contained ten pressures for each of the temperatures measured ($-30 \leq T \leq 50°C$). The first data set was used to determine the uncertainty due to measured temperature. To do this, the program was first run-with the temperature uncertainty (0.6°C) subtracted from the temperatures. Next, the program was run with the temperature uncertainty added to the temperatures. Finally, the change in density with respect to temperature was determined as shown in equation A.29.

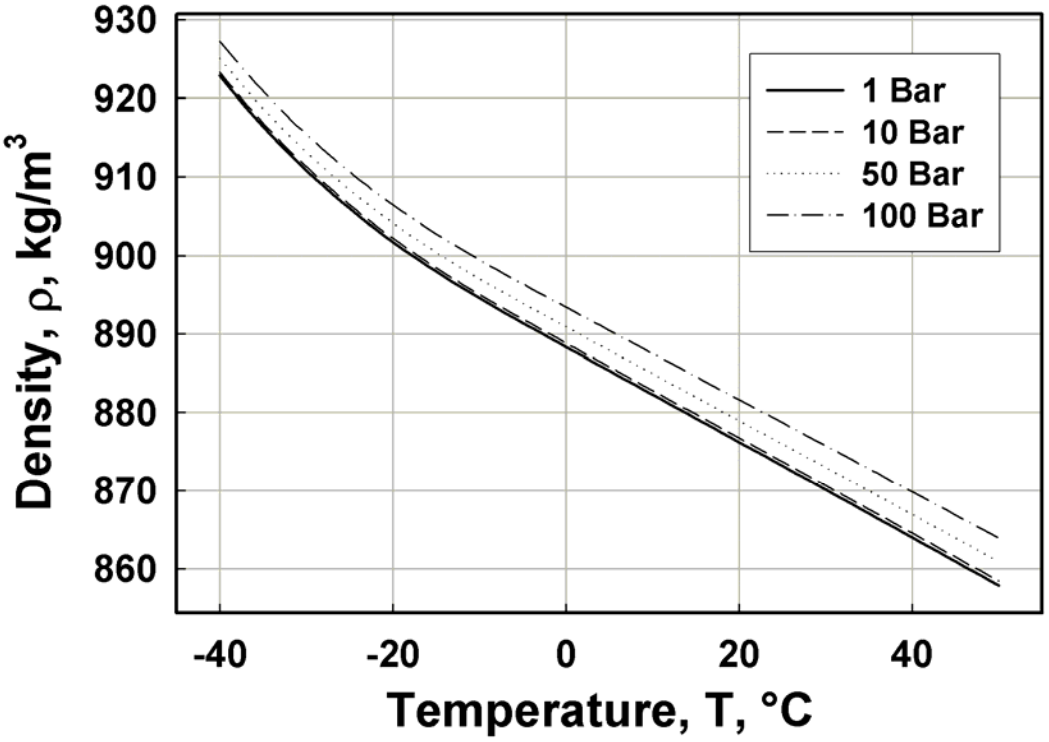

Figure A.1 Effect of Pressure and Temperature on ρ

$$\frac{\partial \rho}{\partial T} = \frac{\rho_{T+\Delta T,P} - \rho_{T-\Delta T,P}}{2U_T} \tag{A.29}$$

Similarly, the second data set was used to determine the uncertainty due to the measured pressure. In this case the value of the uncertainty in the pressure (10.342 kPa) was first added and then subtracted from the pressures in the data set and the resulting change in density with respect to pressure calculated as shown in equation A.30.

$$\frac{\partial \rho}{\partial P} = \frac{\rho_{P+\Delta P,T} - \rho_{P-\Delta P,T}}{2U_P} \tag{A.30}$$

These calculations were conducted at all temperatures in the data set.

Finally, the uncertainty in the density due to the uncertainty in measured pressure and temperature was found using equation A.31.

$$U_{\rho,m} = \sqrt{\left(\frac{\partial \rho}{\partial T} U_T\right)^2 + \left(\frac{\partial \rho}{\partial P} U_P\right)^2} \tag{A31}$$

The changes in density with respect to pressure and temperature were then plotted as shown in Figures A.2 and A.3.

As is seen in Figures A.2 and A.3, the change in density with respect to both temperature and pressure remains fairly constant over the range of values covered. Furthermore, for $T > 0^oC$ the uncertainty in the density does not vary appreciably with temperature. The maximum absolute values of both $\partial\rho/\partial T$ and $\partial\rho/\partial P$ were used to determine a conservative overall uncertainty in density ($U_{\rho,m}$) due to measurement uncertainties in temperature and pressure, which was then used to calculate the uncertainty in density for every data point. The values used for this uncertainty are shown below in Equations A.32, A.33, and A.34:

$$\frac{\partial \rho}{\partial T} = 1.04 \text{ kg/m}^3\text{-K} \tag{A.32}$$

$$\frac{\partial \rho}{\partial P} = 6.285 \times 10^{-7} \text{ kg/m}^3\text{-Pa} \tag{A.33}$$

$$U_{\rho,m} = \sqrt{[(1.04)(0.6)]^2 + [(6.285\times10^{-7})(10342)]^2} = 0.624\,\text{kg/m}^3 \tag{A.34}$$

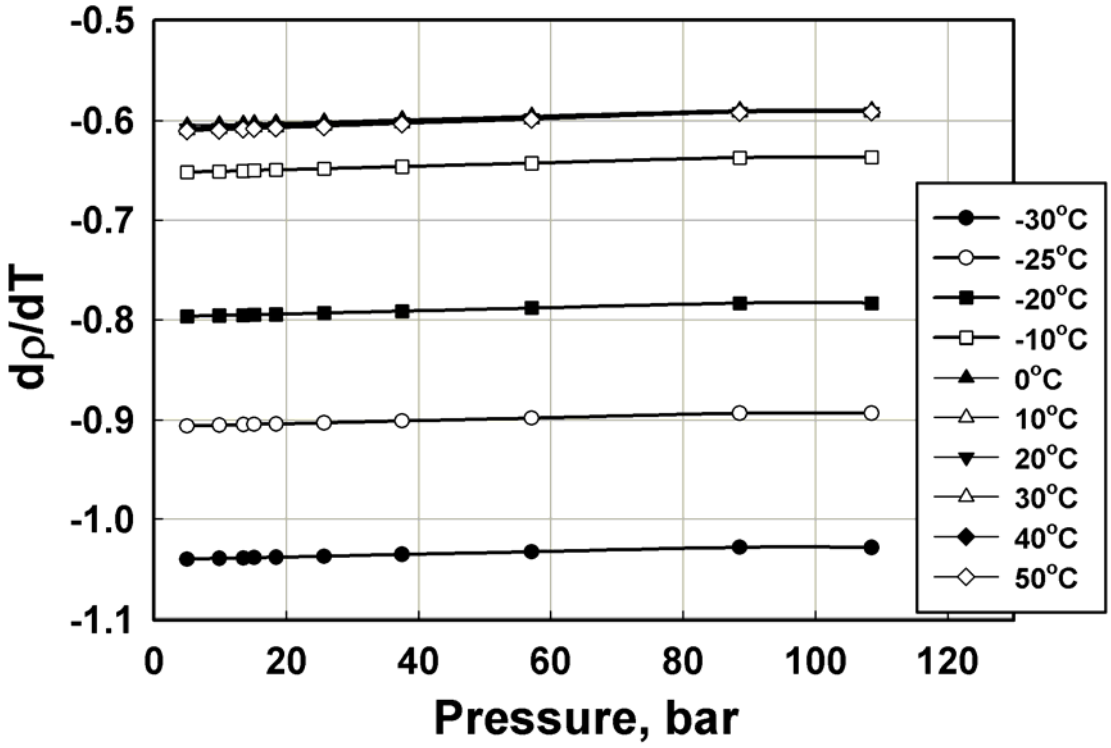

Figure A.2 Effect of Pressure and Temperature on $\partial\rho/\partial T$

A4-1 Uncertainties in the FORTRAN Subroutine Property Data

Property information returned by the FORTRAN subroutine was based on test data supplied by the fluid supplier. The density data supplied included an uncertainty of 0.5% of actual values for density.

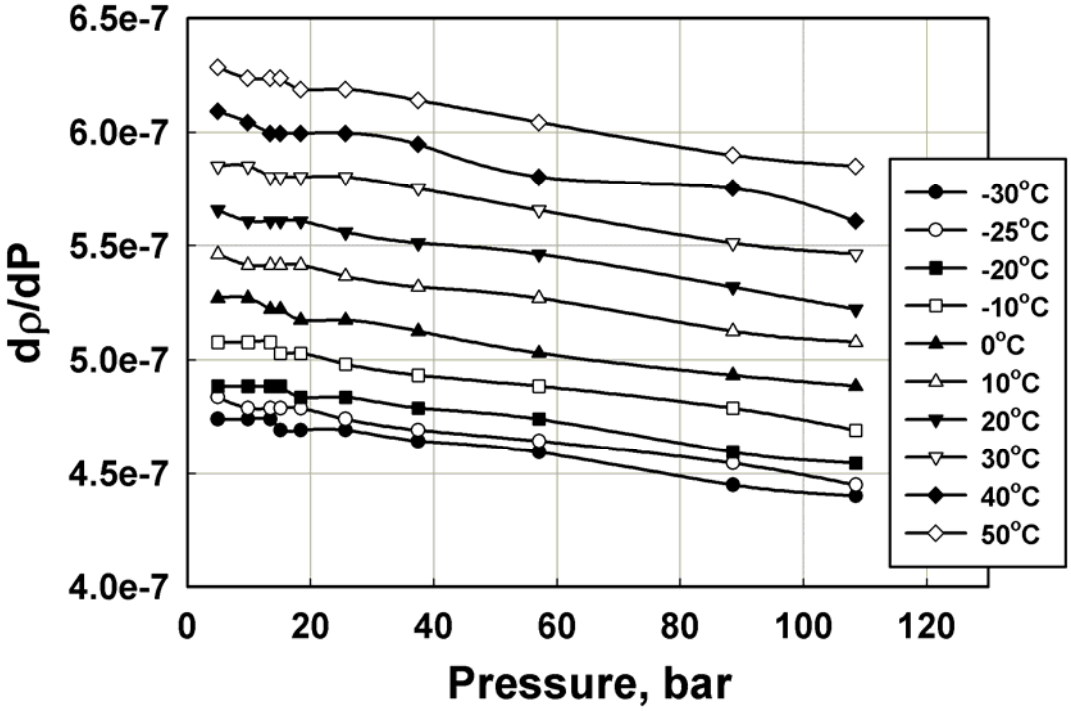

Figure A.3 Effect of Pressure and Temperature on ∂ρ/∂P

A4-2 Overall Uncertainty Calculation for Density

The overall uncertainty in the density was calculated by combining the uncertainties in the properties due to measured uncertainties in temperature and pressure, and the uncertainties in the calculation of (knowledge of) properties at any given condition as follows:

$$U_{\rho} = \sqrt{\left(U_{\rho,m}\right)^2 + \left(U_{\rho,s}\right)^2} \qquad \text{(A.35)}$$

A5 Uncertainties in Viscosity

The generalized viscosity in this study was calculated using equation B36, as suggested by Sorab et al.(1993):

$$\mu_{ge} = a_T \mu_{H,0} + a_T (\mu_{L,0} - \mu_{H,0}) \left[1 + (a_T \lambda_0 \kappa)^2\right]^{\frac{(n-1)}{2}} \quad \text{(A.36)}$$

Where,

$$a_T = e^{\left[A_2\left(\frac{T_0}{T}-1\right)+A_4\left(\frac{T_0}{T}-1\right)^2\right]} \quad \text{(A.37)}$$

The viscosity depends on temperature and shear rate. Figure A.4 shows the variation of viscosity with temperature and shear rate.

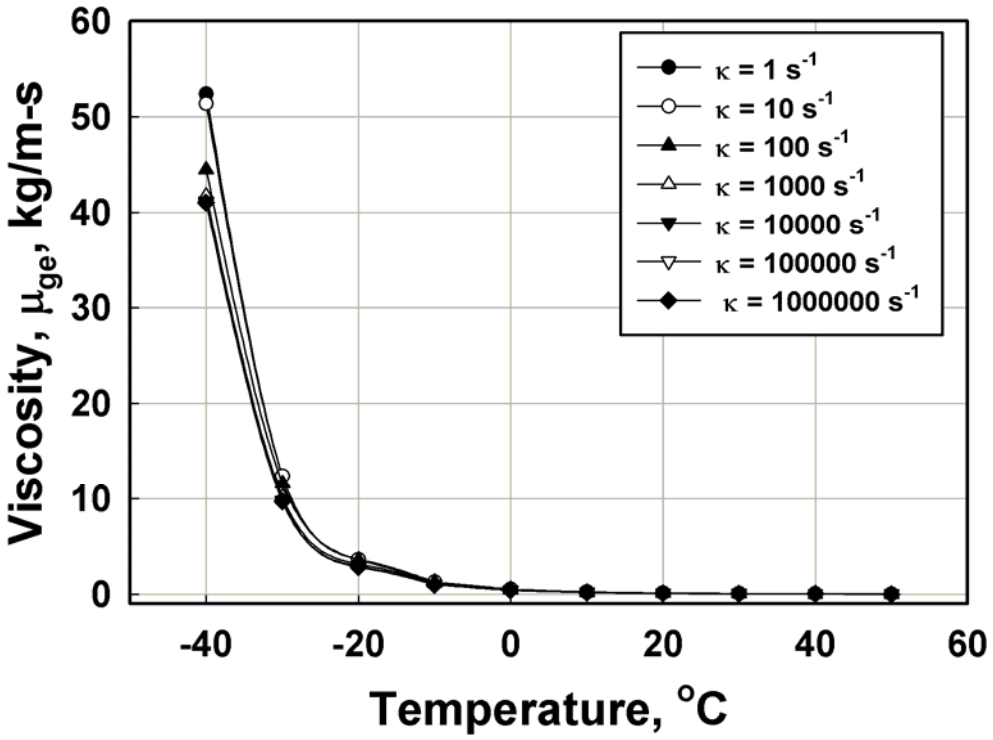

Figure A.4 Effect of Temperature and Shear Rate on μ_{ge}

It is clearly seen from the Figure A.4 that temperature strongly affects the viscosity for T < 0^oC. The viscosity decreases sharply as the temperature increase up to 0^oC. At higher temperatures, the decrease is very small. However, shear rate does not affect the viscosity significantly, particularly for T > -20^oC. The shear rate is calculated as follows:

$$\kappa = \frac{32Q}{\pi d^3} \tag{A.38}$$

The respective derivatives are:

$$\frac{\partial \kappa}{\partial Q} = \frac{32}{\pi D^3} \tag{A.39}$$

$$\frac{\partial \kappa}{\partial Q} = -\frac{96Q}{\pi D^4} \tag{A.40}$$

Therefore uncertainties in shear rate measurement were calculated accounting for uncertainties in flow rate and diameter measurement as follows:

$$U_\kappa^2 = \left(\frac{\partial \kappa}{\partial Q} U_Q\right)^2 + \left(\frac{\partial \kappa}{\partial D} U_D\right)^2 \tag{A.41}$$

To determine the uncertainty in the viscosity values calculated by the equation A.36, the uncertainty in the measured temperature and shear rate must be taken into account. This was accomplished by creating two representative data sets with temperature and shear rate values that spanned the entire range of recorded values. Both data sets contained ten shear rates for each of the temperatures measured (-30°C ≤ T ≤ 50°C). The first data set was used to determine the uncertainty due to measured temperature. To do this, the program was first run with the temperature uncertainty (0.6°C) subtracted from the temperatures. Next, the program was run with the temperature uncertainty added to the

temperatures. Finally, the change in viscosity with respect to temperature was determined as shown in equation A.42.

$$\frac{\partial \mu_{ge}}{\partial T} = \frac{\mu_{ge_{T+\Delta T,\kappa}} - \mu_{ge_{T-\Delta T,\kappa}}}{2U_T} \tag{A.42}$$

Similarly, the second data set was used to determine the uncertainty due to the measured shear rate. In this case an approximate shear rate increment of 5000 s^{-1} was first added and then subtracted from the shear rate in the data set and the resulting change in viscosity with respect to shear rate was calculated as shown in equations A.43.

$$\frac{\partial \mu_{ge}}{\partial \kappa} = \frac{\mu_{ge_{\kappa+\Delta\kappa,T}} - \mu_{ge_{\kappa-\Delta\kappa,T}}}{2\Delta\kappa} \tag{A.43}$$

These calculations were conducted at all temperatures in the data set. Finally, the uncertainty in the viscosity due to uncertainties in measured temperature and shear rate was found using equations A.44.

$$U_{\mu_{ge}} = \sqrt{\left(\frac{\partial \mu_{ge}}{\partial T} U_T\right)^2 + \left(\frac{\partial \mu_{ge}}{\partial \kappa} U_\kappa\right)^2} \tag{A.44}$$

The respective changes in viscosity with respect to temperature and shear rate are shown in Figures A.5 and A.6. It is clear from Figure A.5 that $d\mu_{ge}/dT$ remains fairly constant with shear rate. From Figure A.6 it is seen that shear rate influences the $d\mu_{ge}/d\kappa$ only at the smaller shear rates. At higher shear rates, $d\mu_{ge}/d\kappa$ is essentially zero. However it should be noted that this may be due to the relatively small $\Delta\kappa$ at higher shear rates. The maximum absolute values of $d\mu_{ge}/dT$ and $d\mu_{ge}/d\kappa$ were used for the error analysis to obtain conservative estimates. Table A.9 shows these values for each temperature.

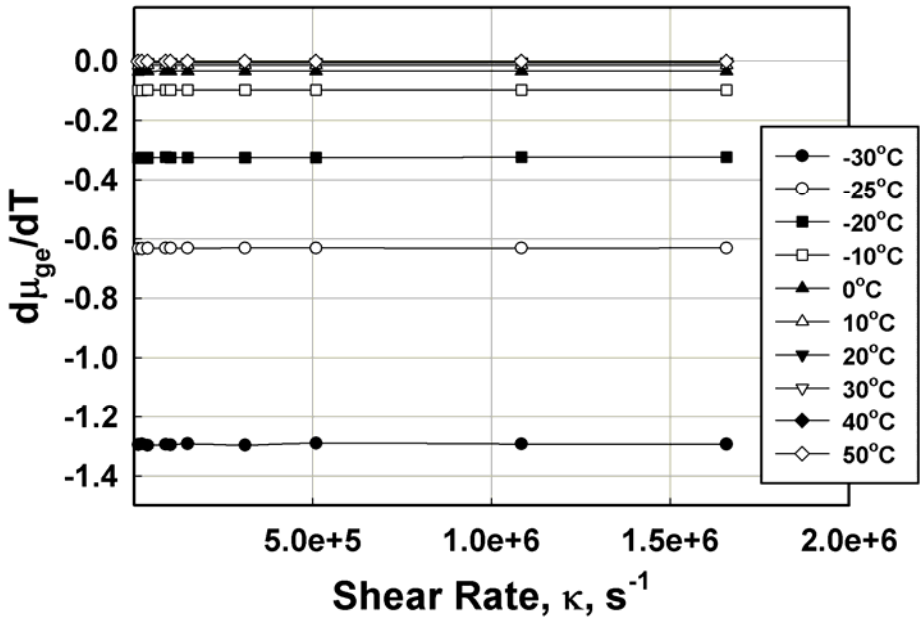

Figure A.5 Effect of Temperature and Shear Rate on $d\mu_{ge}/dT$

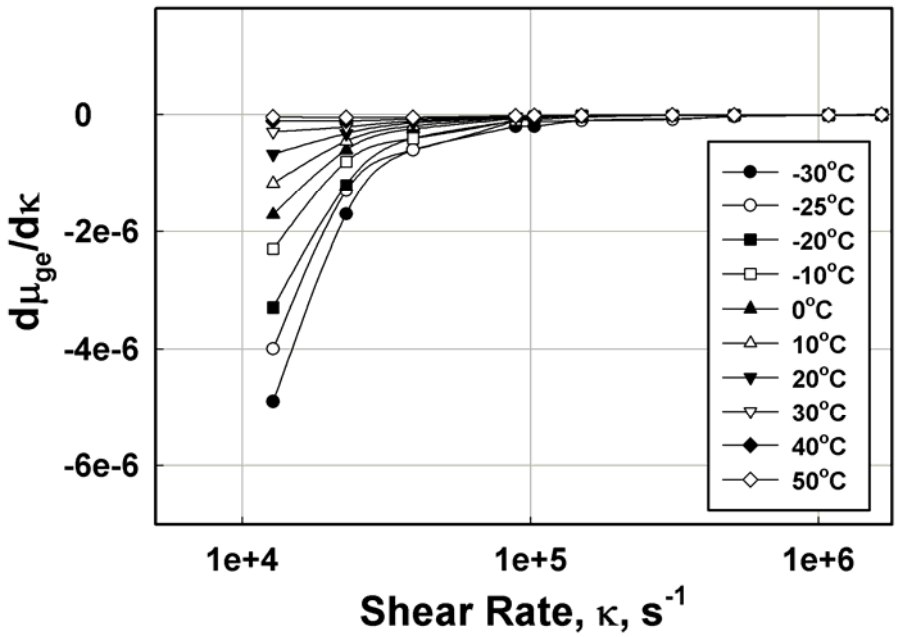

Figure A.6 Effect of Temperature and Shear Rate on $d\mu_{ge}/d\kappa$

Table A.9 Uncertainty in Viscosity based on Temperature and Shear Rate Measurements

Temperature (^{o}C)	$d\mu_{ge}/dT$ (kg/m-s-K)	$d\mu_{ge}/d\kappa$ (kg/m)
-30	-1.2975	4.90E-6
-25	-0.6308	4.00E-6
-20	-0.3233	3.30E-6
-10	-0.0965	2.30E-6
0	-0.0338	1.71E-6
10	-0.0134	1.17E-6
20	-0.0059	6.7E-7
30	-0.0029	2.9E-7
40	-0.0015	1.06E-7
50	-0.0008	4.7E-8

APPENDIX B

B1 Effect of Temperature on Pressure Drop -Flow Rate Characteristics

In these figures, data for T ≥ 20°C are taken from Mincks (2002).

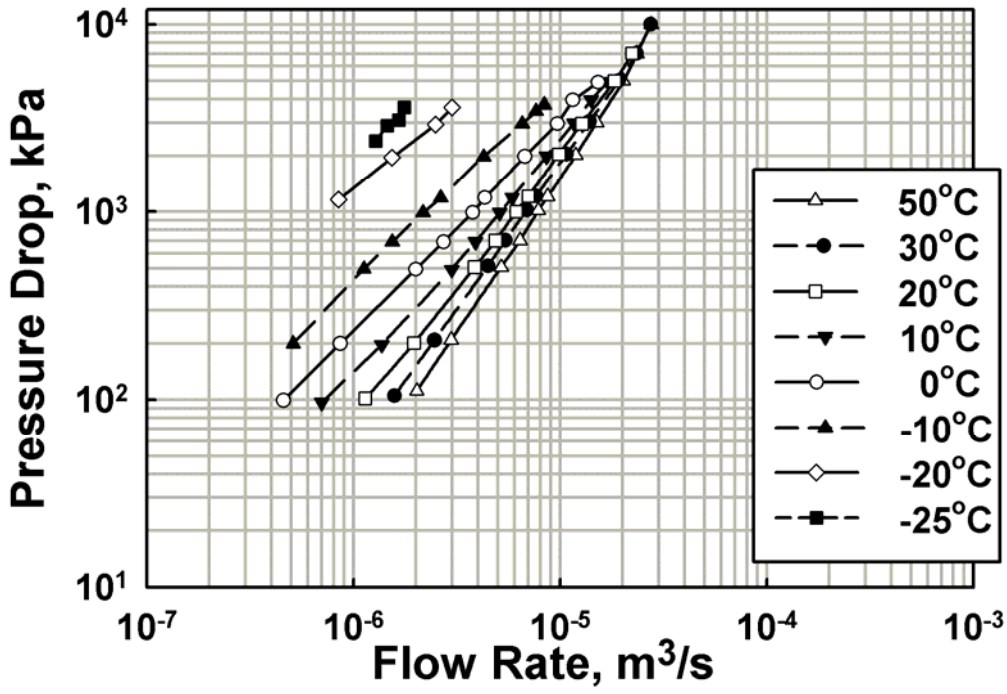

Figure B.1 Pressure Drop -Flow Rate Characteristics for 0.5 mm Diameter, 1 mm Thick Orifice

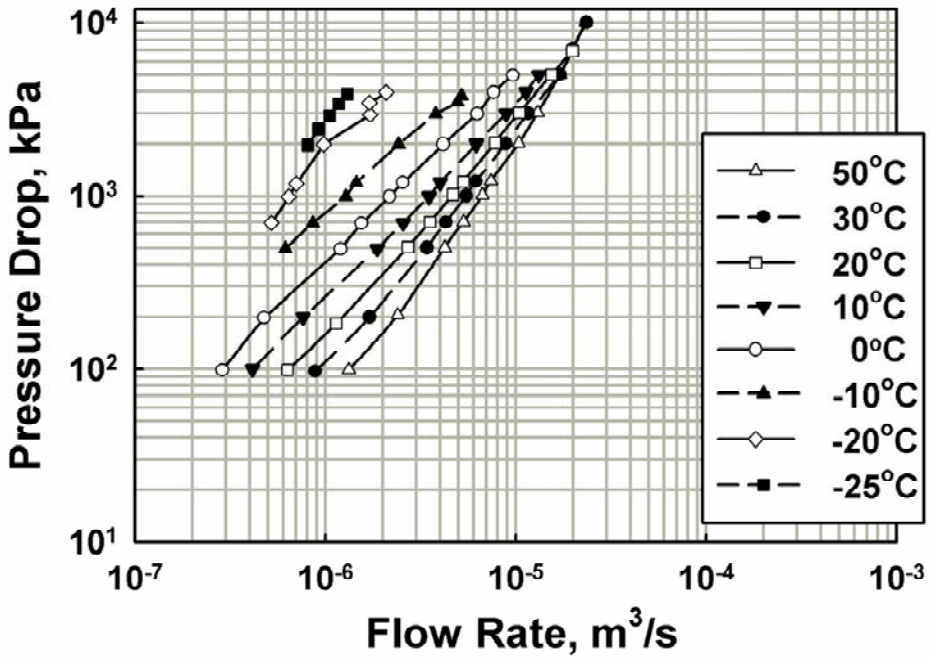

Figure B.2 Pressure Drop -Flow Rate Characteristics for 0.5 mm Diameter, 2 mm Thick Orifice

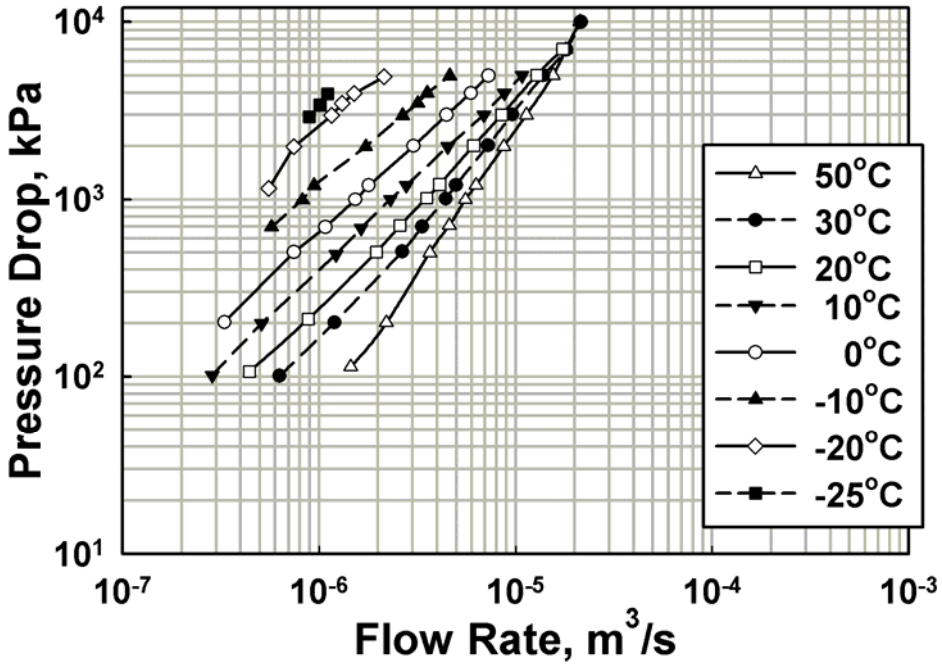

Figure B.3 Pressure Drop-Flow Rate Characteristics for 0.5 mm Diameter, 3 mm Thick Orifice

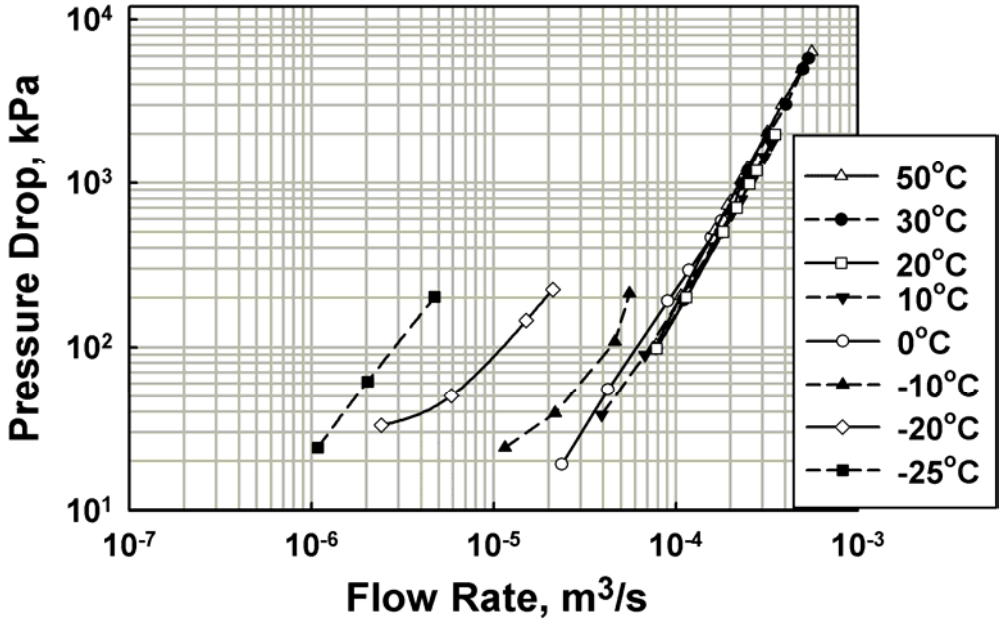

Figure B.4 Pressure Drop -Flow Rate Characteristics for 3 mm Diameter, 1 mm Thick Orifice

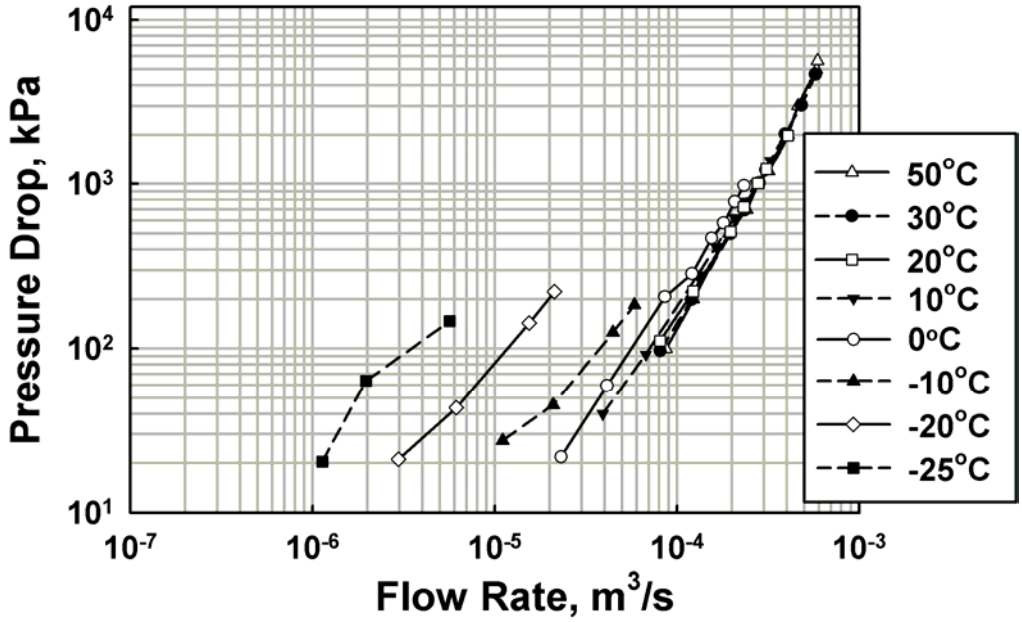

Figure B.5 Pressure Drop -Flow Rate Characteristics for 3 mm Diameter, 2 mm Thick Orifice

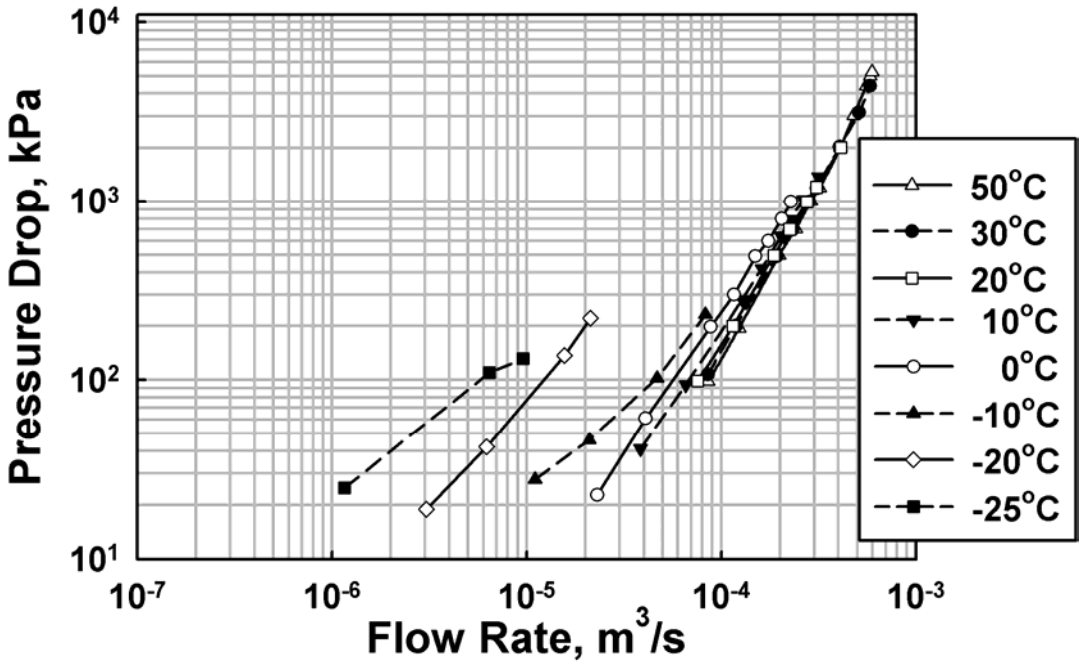

Figure B.6 Pressure Drop -Flow Rate Characteristics for 3 mm Diameter, 3 mm Thick Orifice

B2 Effect of Thickness on Pressure Drop –Flow Rate Characteristics

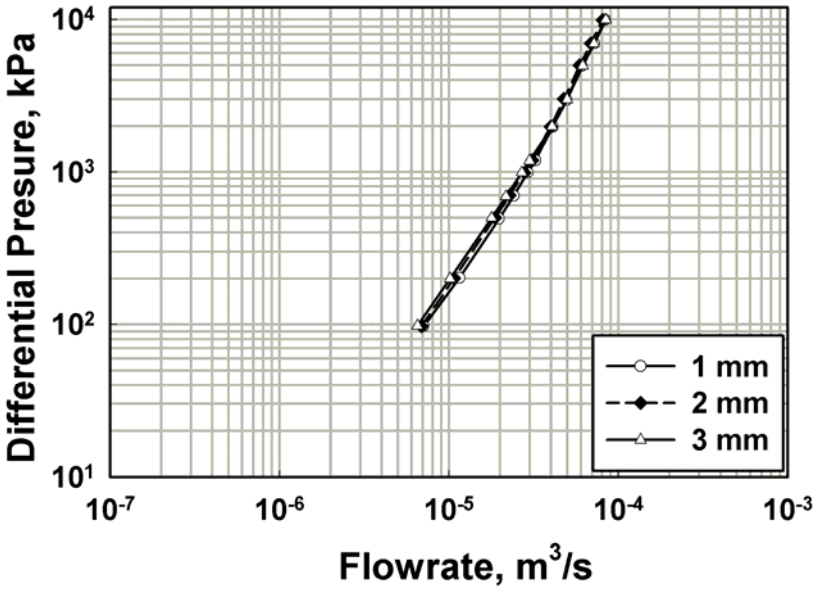

Figure B.7 Effect of Thickness on Pressure Drop -Flow Rate Characteristics for 1 mm Diameter Orifices at T ~ 40°C (Mincks 2002)

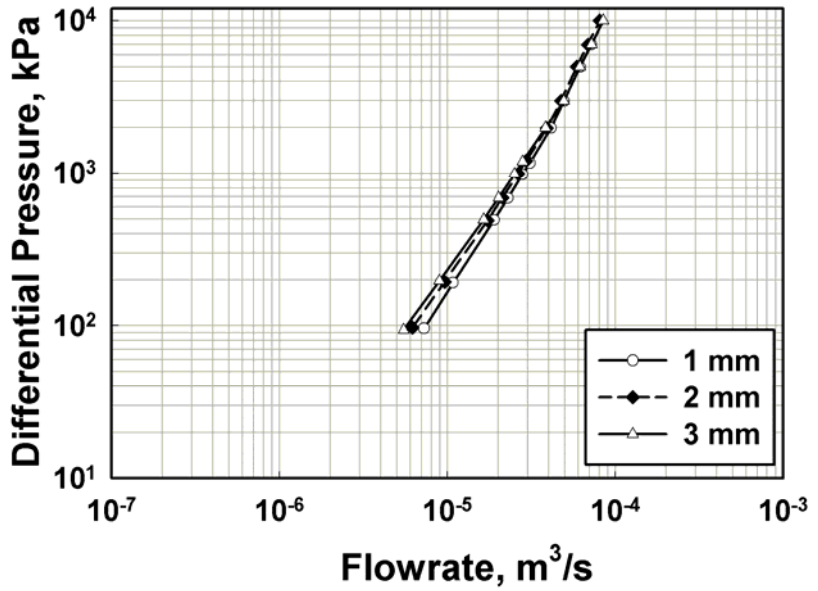

Figure B.8 Effect of Thickness on Pressure Drop -Flow Rate Characteristics for 1 mm Diameter Orifices at T ~ 30°C (Mincks 2002)

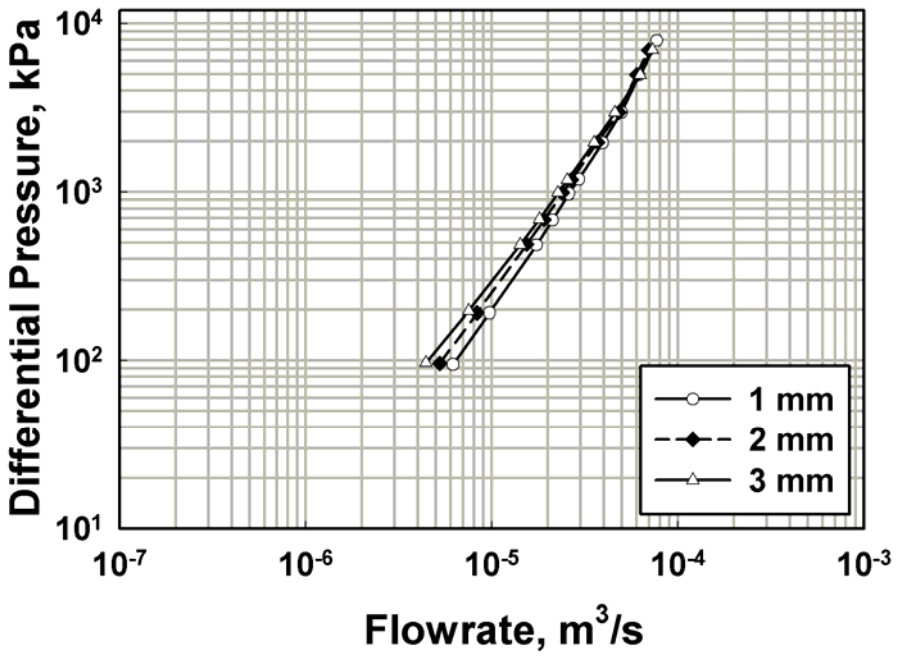

Figure B.9 Effect of Thickness on Pressure Drop -Flow Rate Characteristics for 1 mm Diameter Orifices at T ~ 20°C (Mincks 2002)

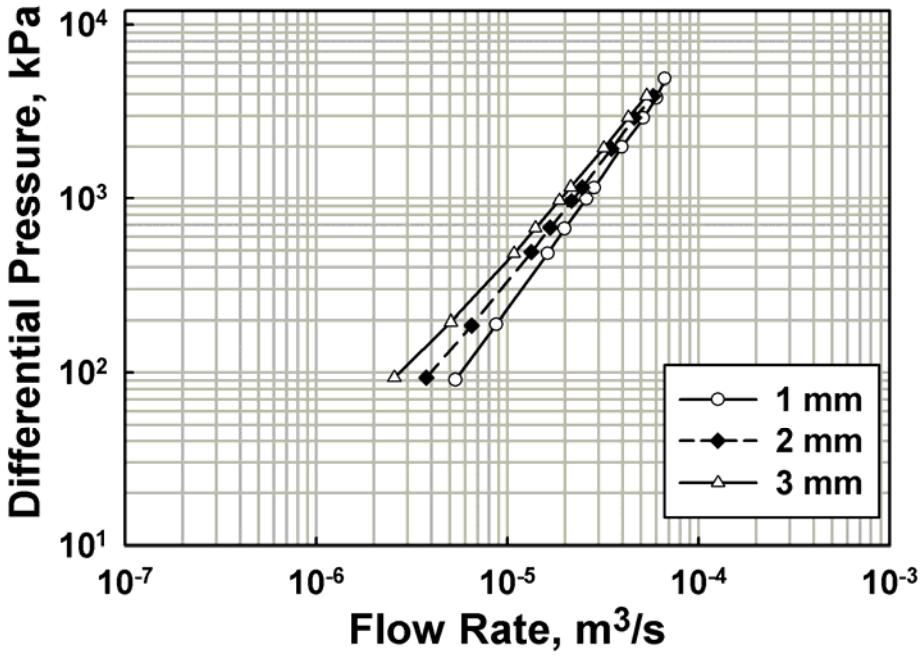

Figure B.10 Effect of Thickness on Pressure Drop -Flow Rate Characteristics for 1 mm Diameter Orifices at T ~ 10°C

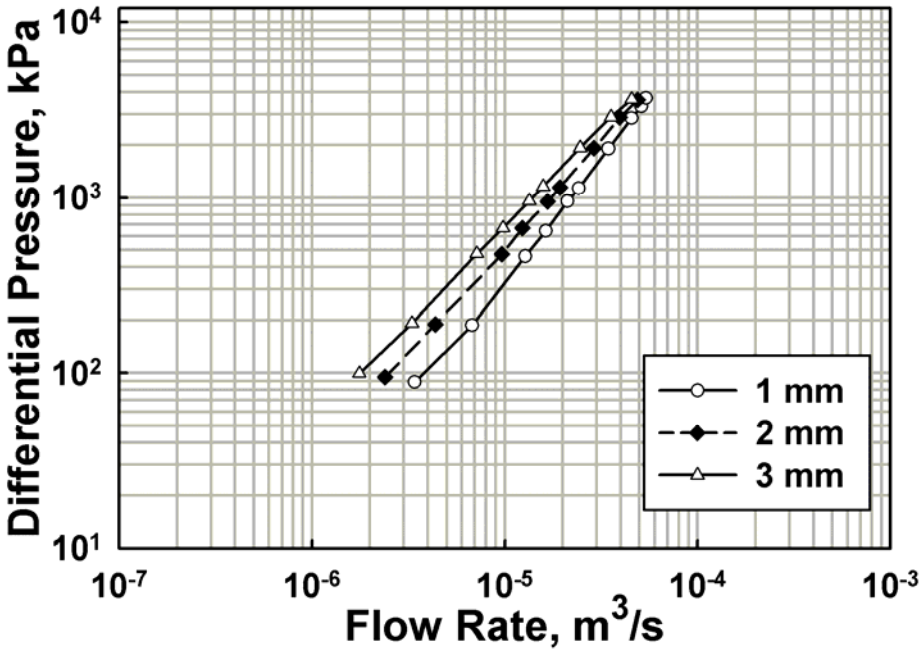

Figure B.11 Effect of Thickness on Pressure Drop -Flow Rate Characteristics for 1 mm Diameter Orifices at T ~ 0°C

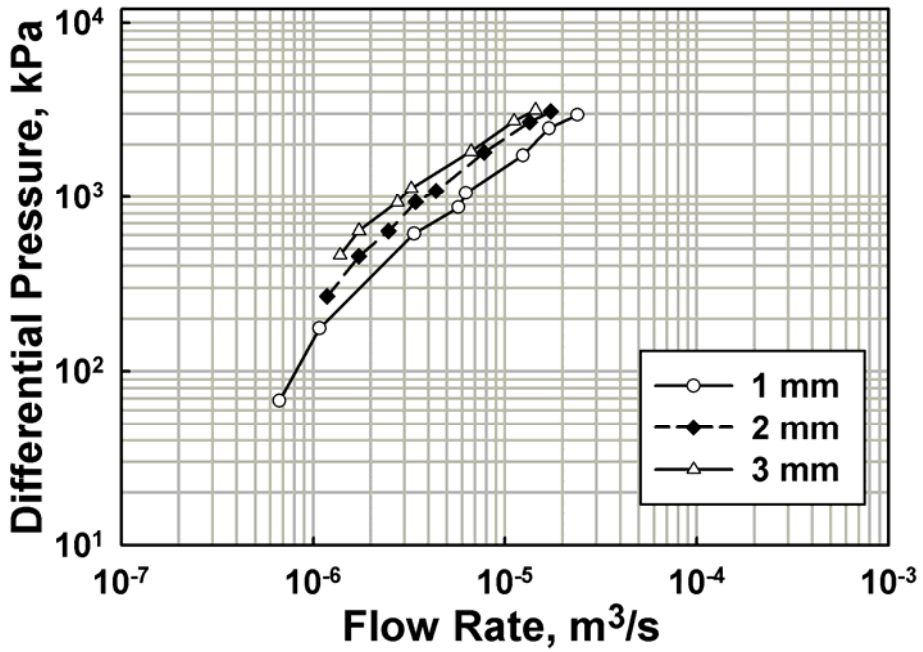

Figure B.12 Effect of Thickness on Pressure Drop -Flow Rate Characteristics for 1 mm Diameter Orifices at T ~ -20°C

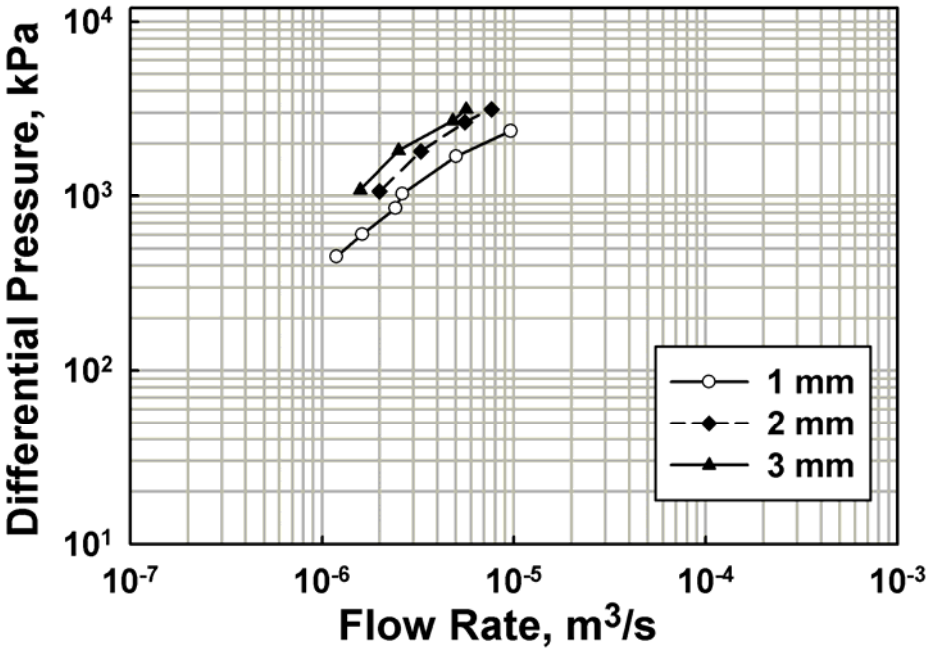

Figure B.13 Effect of Thickness on Pressure Drop -Flow Rate Characteristics for 1 mm Diameter, Orifices at T ~ -25°C

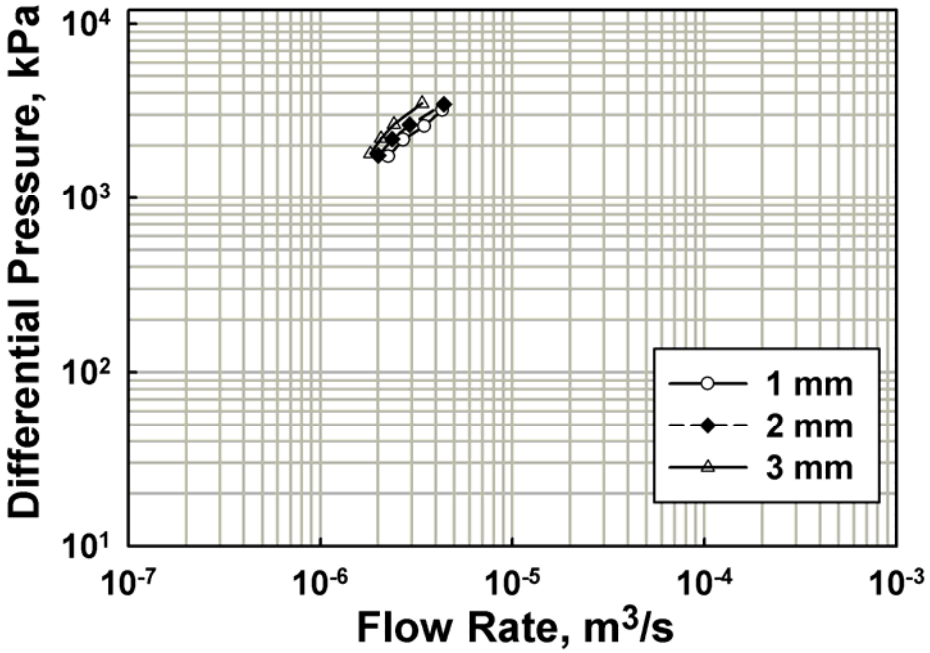

Figure B.14 Effect of Thickness on Pressure Drop -Flow Rate Characteristics for 1 mm Diameter Orifices at T ~ -30°C

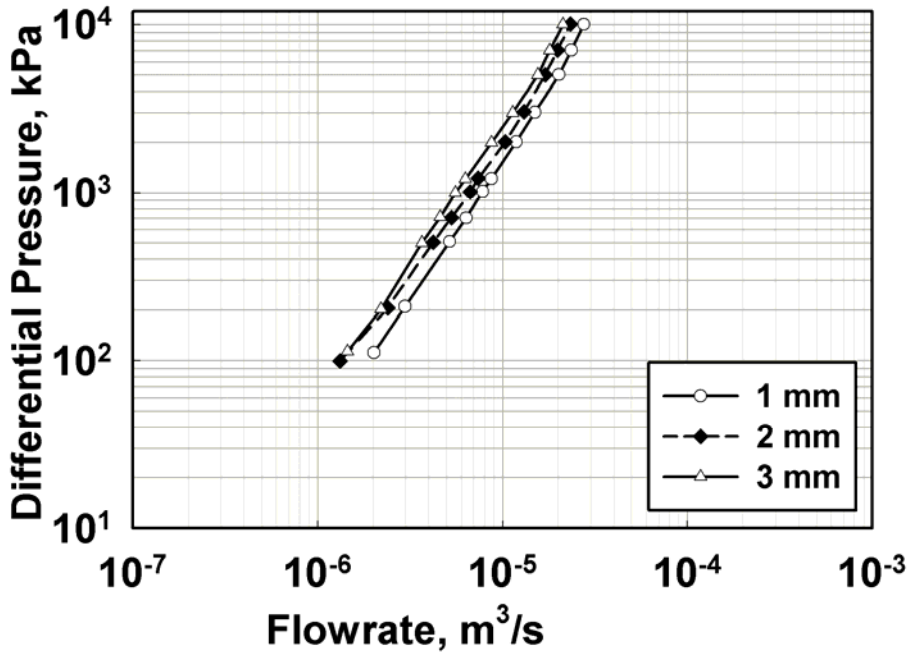

Figure B.15 Effect of Thickness on Pressure Drop -Flow Rate Characteristics for 0.5 mm Diameter Orifices at T ~ 50°C (Mincks 2002)

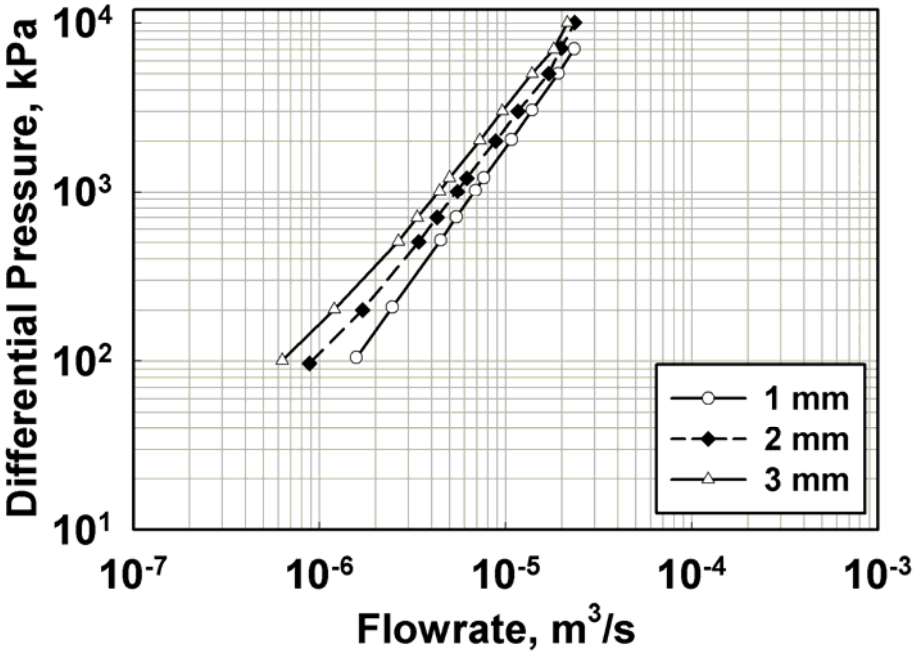

Figure B.16 Effect of Thickness on Pressure Drop -Flow Rate Characteristics for 0.5 mm Diameter Orifices at T ~ 30°C (Mincks 2002)

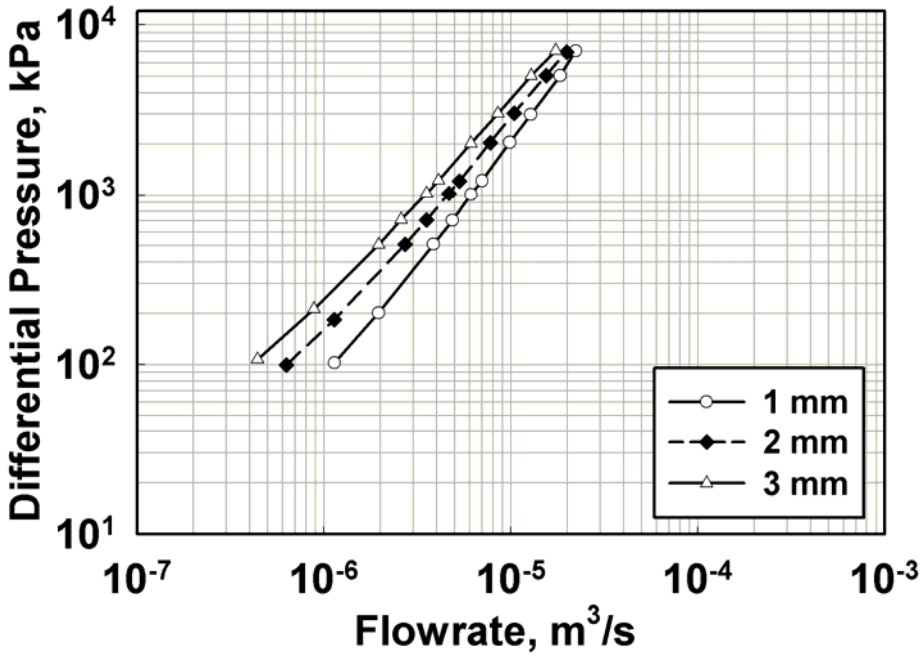

Figure B.17 Effect of Thickness on Pressure Drop -Flow Rate Characteristics for 0.5 mm Diameter Orifices at T ~ 20°C (Mincks 2002)

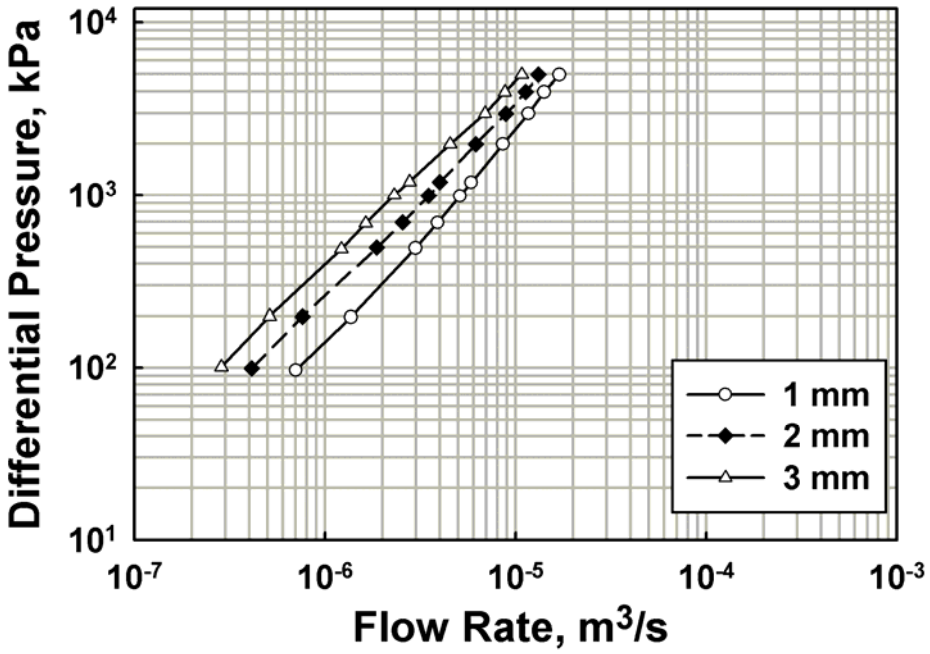

Figure B.18 Effect of Thickness on Pressure Drop -Flow Rate Characteristics for 0.5 mm Diameter Orifices at T ~ 10°C

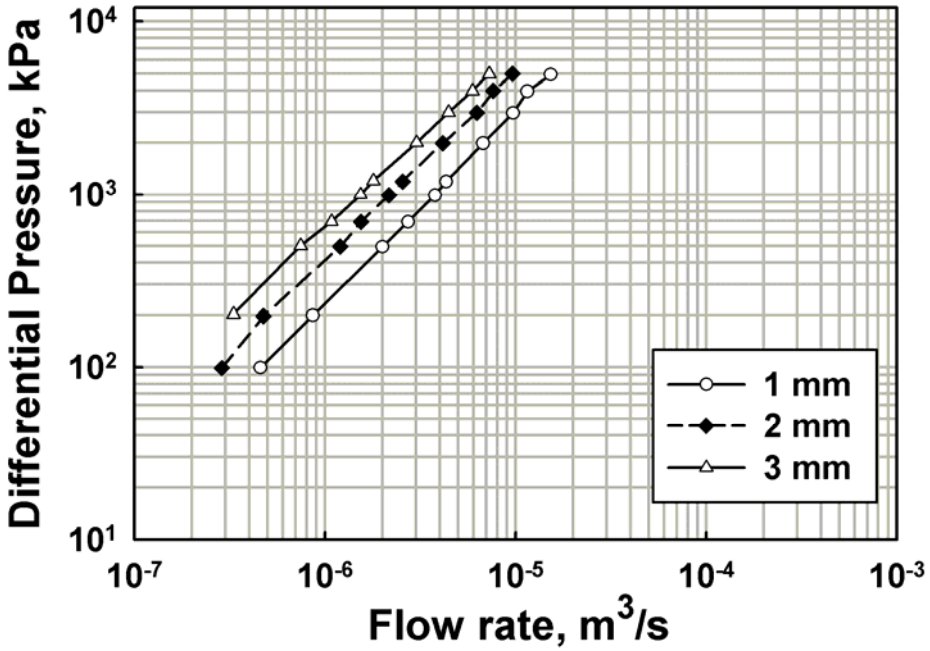

Figure B.19 Effect of Thickness on Pressure Drop -Flow Rate Characteristics for 0.5 mm Diameter Orifices at T ~ 0°C

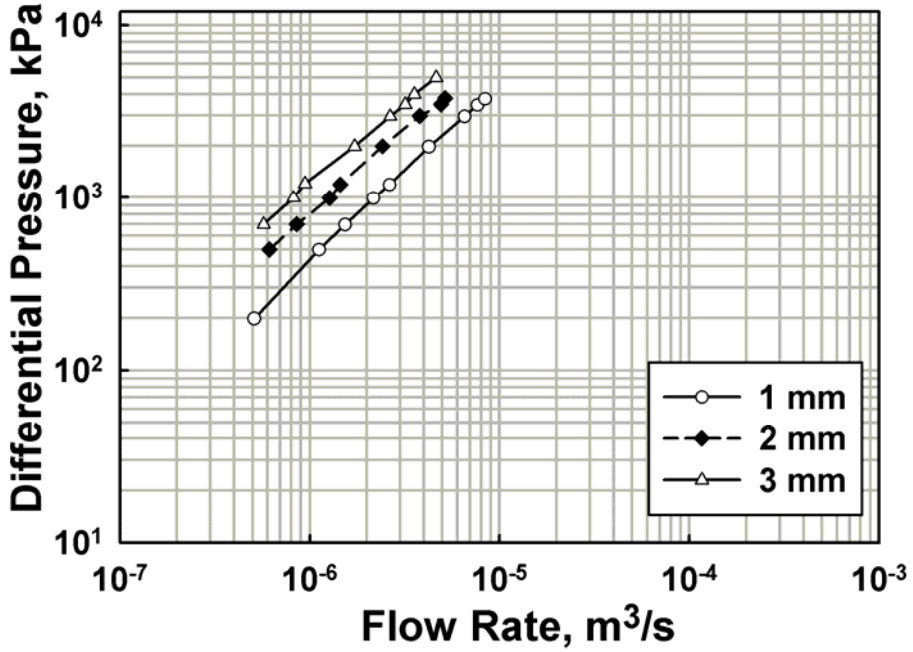

Figure B.20 Effect of Thickness on Pressure Drop -Flow Rate Characteristics for 0.5 mm Diameter Orifices at T ~ -10°C

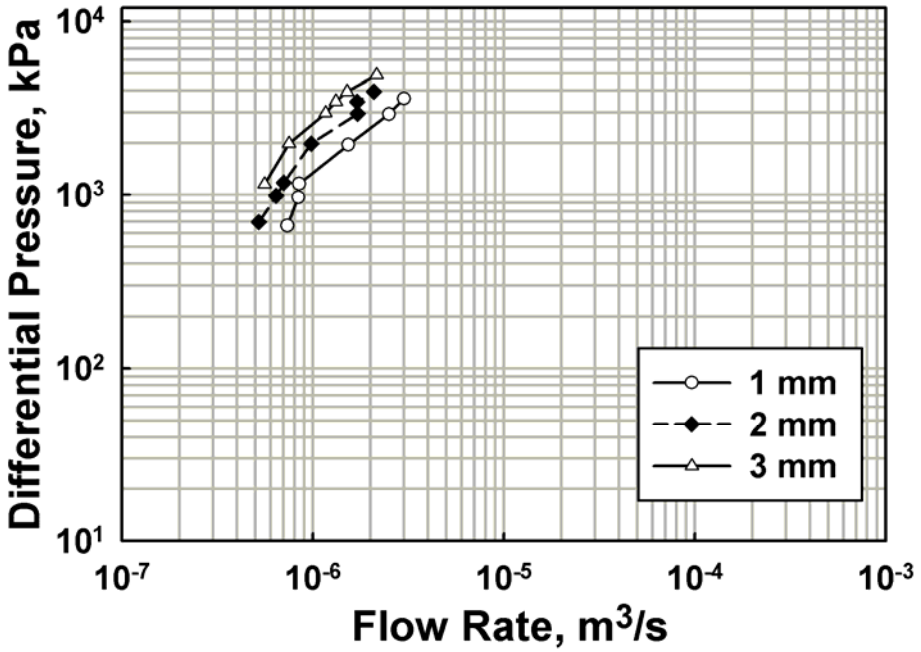

Figure B.21 Effect of Thickness on Pressure Drop -Flow Rate Characteristics for 0.5 mm Diameter Orifices at T ~ -20°C

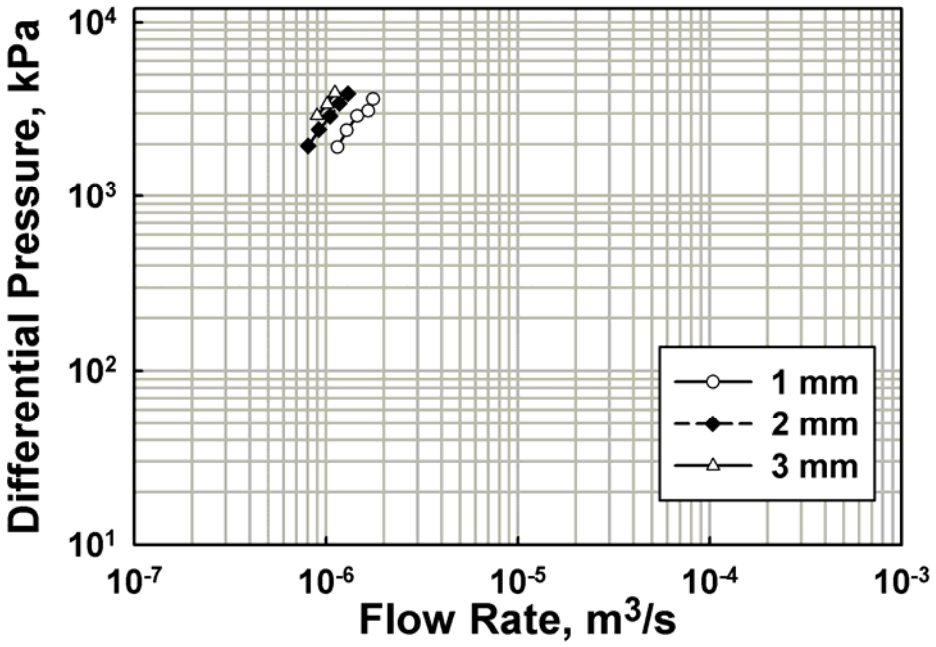

Figure B.22 Effect of Thickness on Pressure Drop -Flow Rate Characteristics for 0.5 mm Diameter Orifices at T ~ -25°C

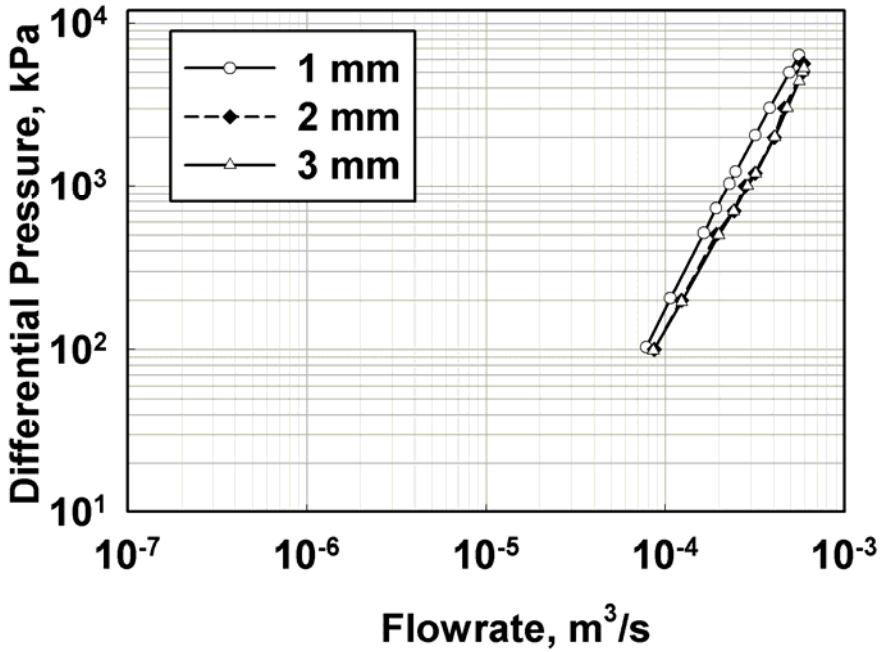

Figure B.23 Effect of Thickness on Pressure Drop -Flow Rate Characteristics for 3 mm Diameter Orifices at T ~ 50°C (Mincks 2002)

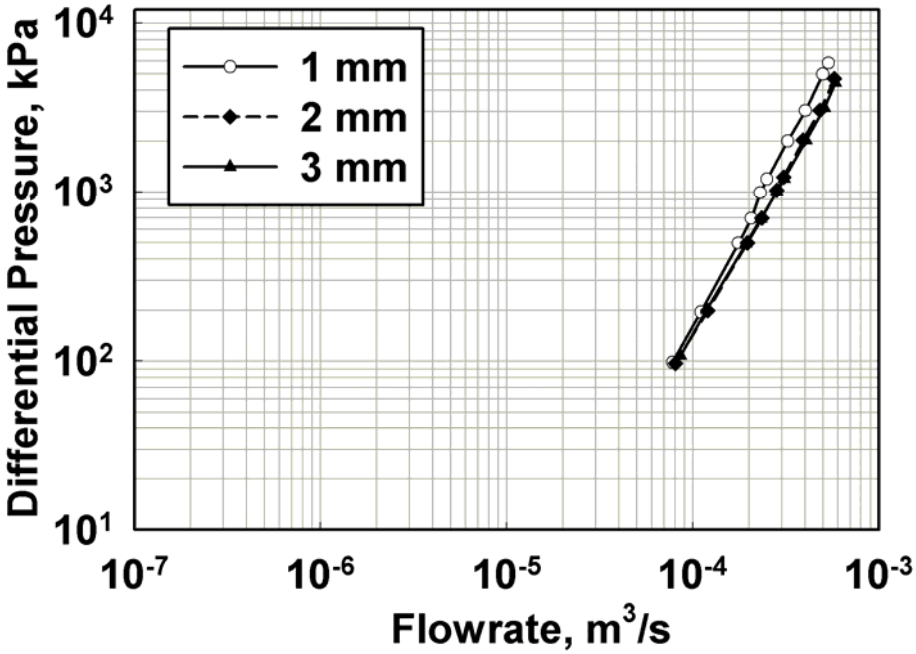

Figure B.24 Effect of Thickness on Pressure Drop -Flow Rate Characteristics for 3 mm Diameter Orifices at T ~ 30°C (Mincks 2002)

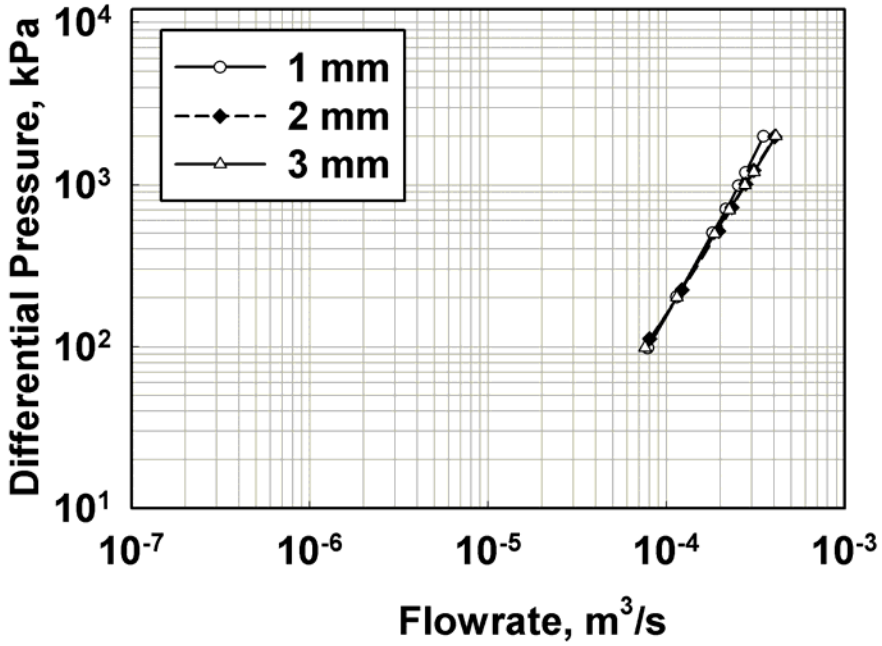

Figure B.25 Effect of Thickness on Pressure Drop -Flow Rate Characteristics for 3 mm Diameter Orifices at T ~ 20°C (Mincks 2002)

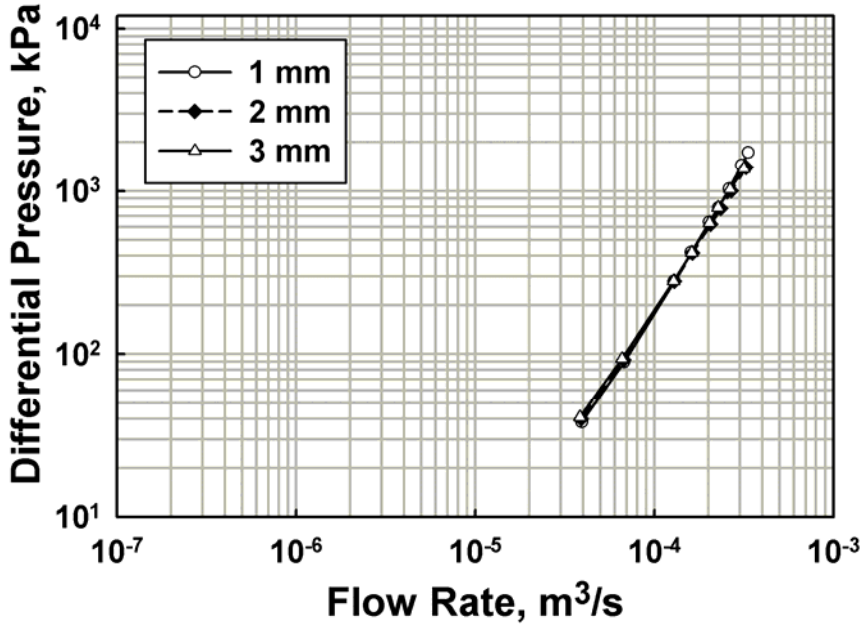

Figure B.26 Effect of Thickness on Pressure Drop -Flow Rate Characteristics for 3 mm Diameter Orifices at T ~ 10°C

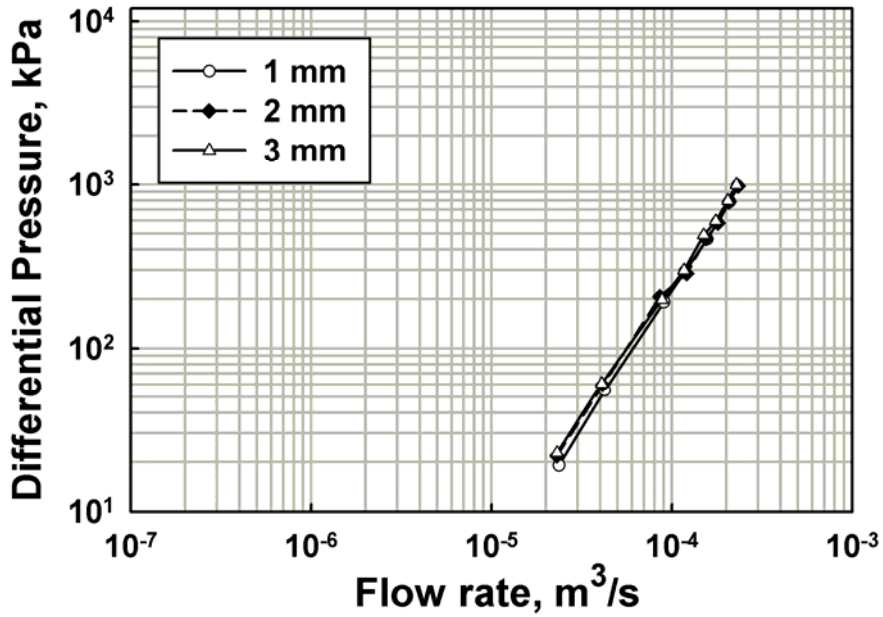

Figure B.27 Effect of Thickness on Pressure Drop -Flow Rate Characteristics for 3 mm Diameter Orifices at T ~ 0°C

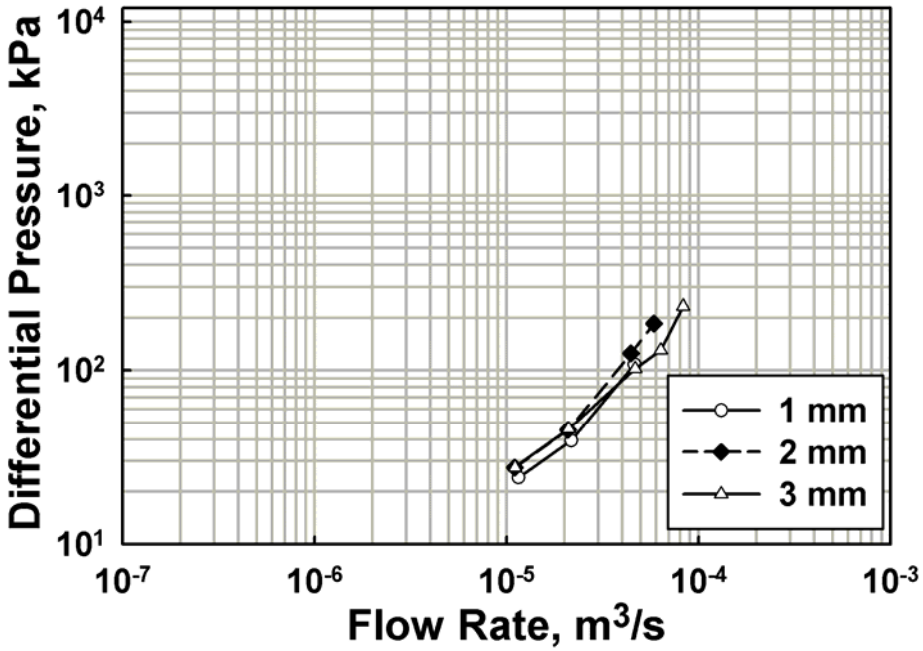

Figure B.28 Effect of Thickness on Pressure Drop -Flow Rate Characteristics for 3 mm Diameter Orifices at T ~ -10°C

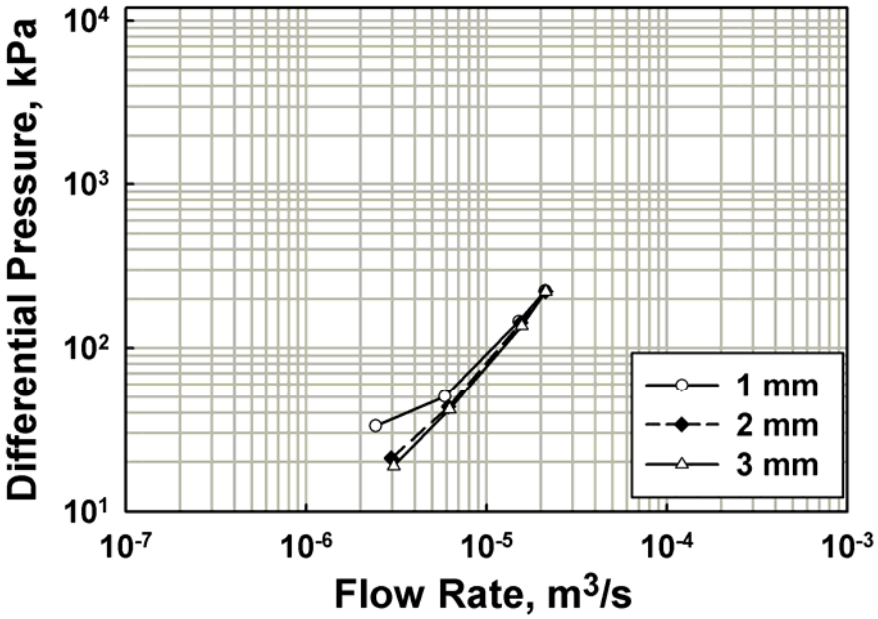

Figure B.29 Effect of Thickness on Pressure Drop -Flow Rate Characteristics for 3 mm Diameter Orifices at T ~ -20°C

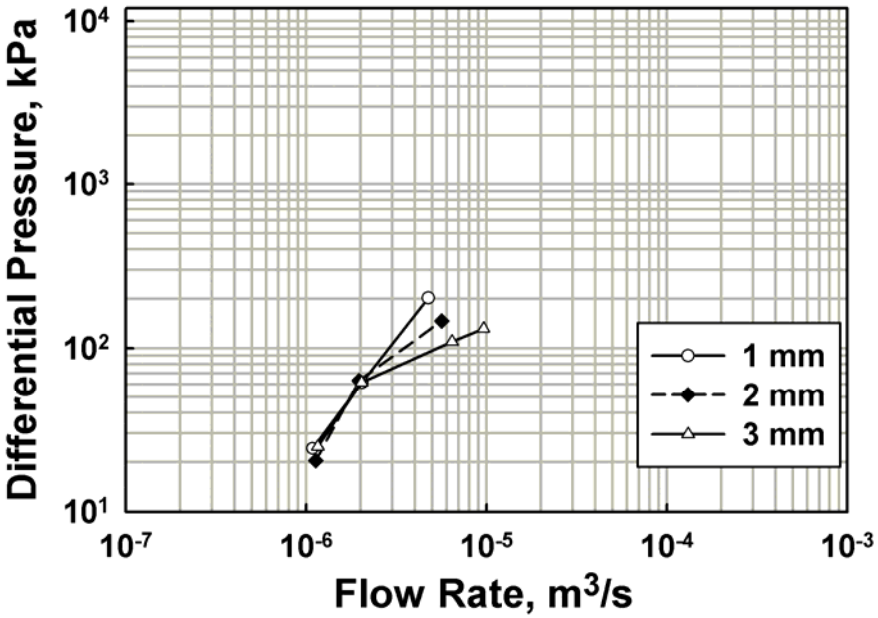

Figure B.30 Effect of Thickness on Pressure Drop -Flow Rate Characteristics for 3 mm Diameter Orifices at T ~ -25°C

APPENDIX C

C1 Effect of Aspect Ratio on Euler Number

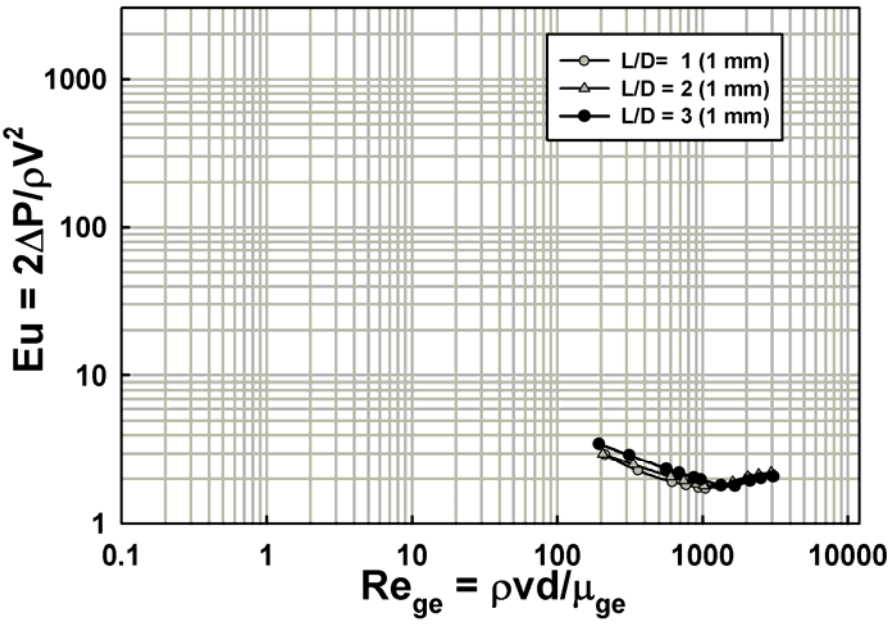

Figure C.1 Effect of Aspect Ratio on Euler Number at T ~ 40°C (Mincks 2002)

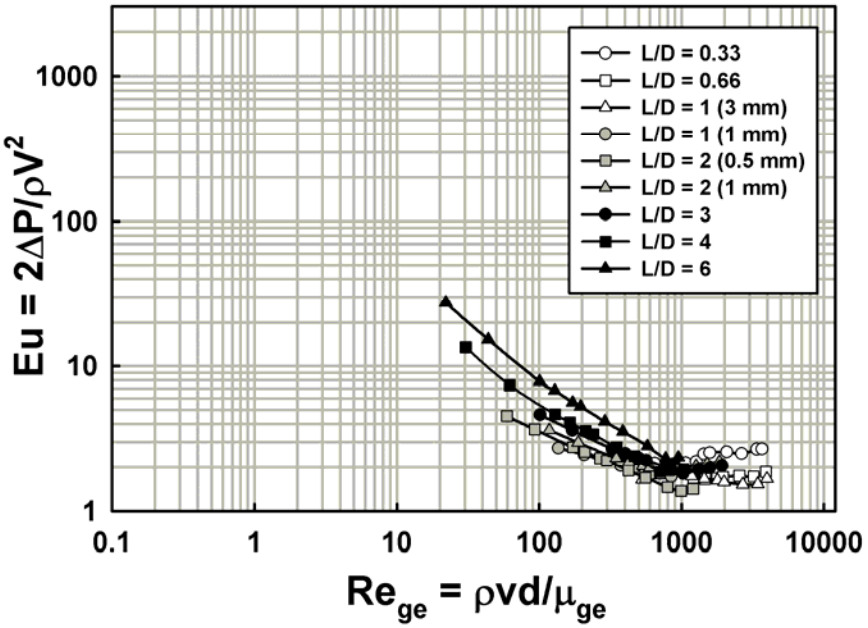

Figure C.2 Effect of Aspect Ratio on Euler Number at T ~ 30°C (Mincks 2002)

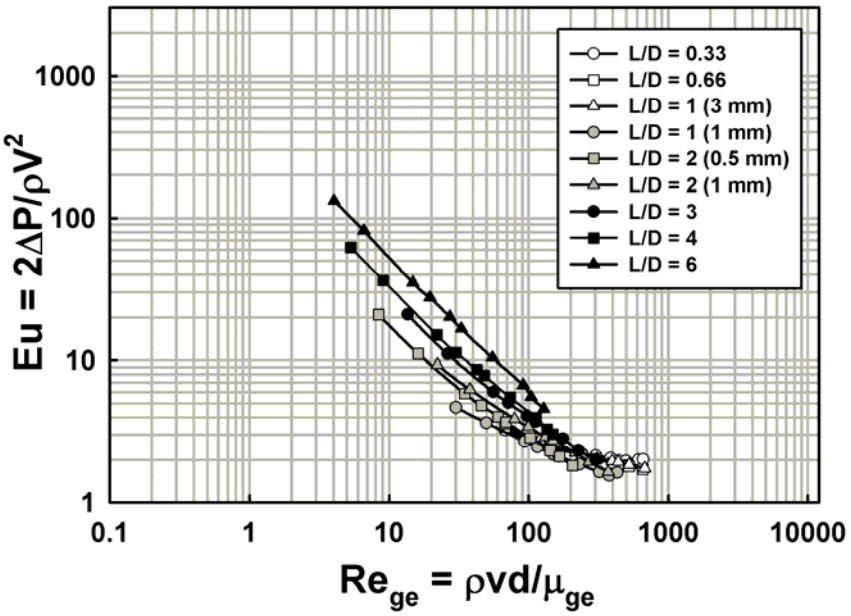

Figure C.3 Effect of Aspect Ratio on Euler Number at T ~ 10°C

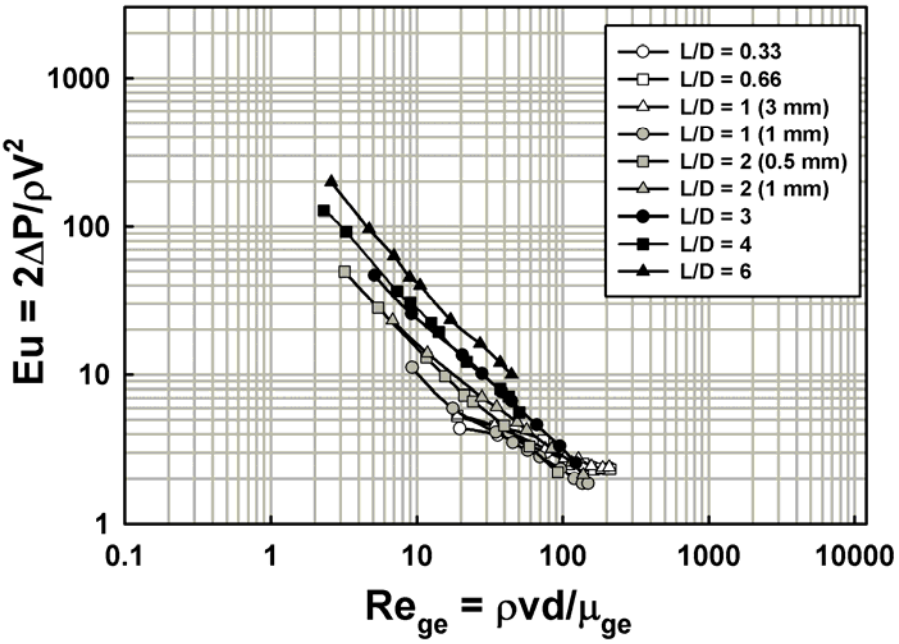

Figure C.4 Effect of Aspect Ratio on Euler Number at T ~ 0°C

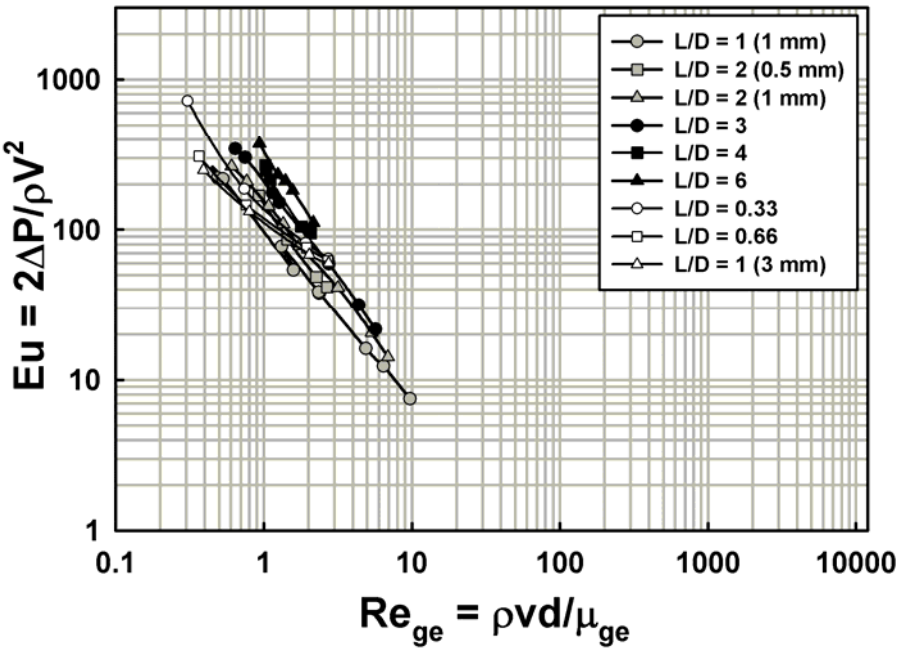

Figure C.5 Effect of Aspect Ratio on Euler Number at T ~ -20°C

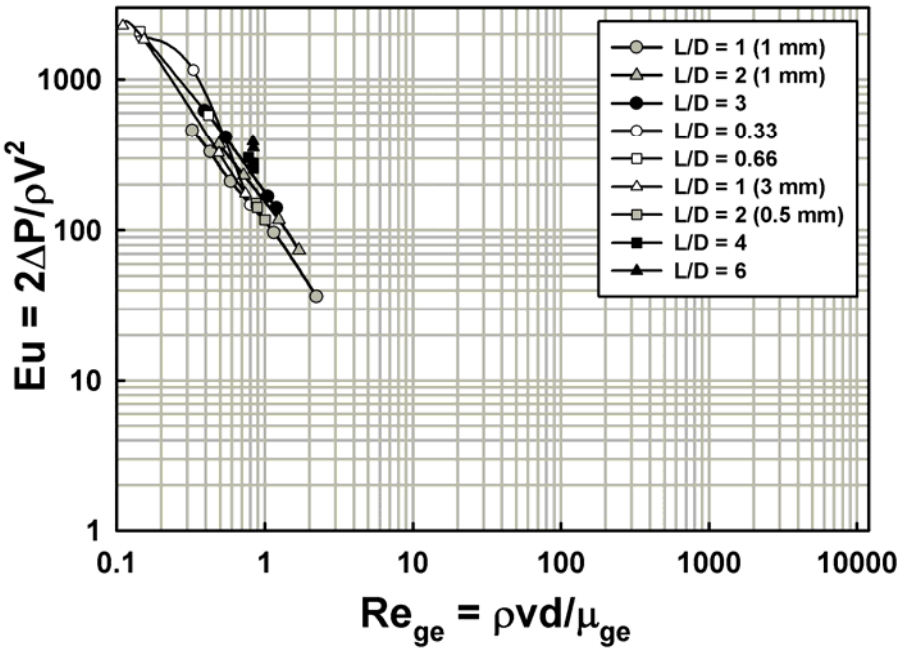

Figure C.6 Effect of Aspect Ratio on Euler Number at T ~ -25°C

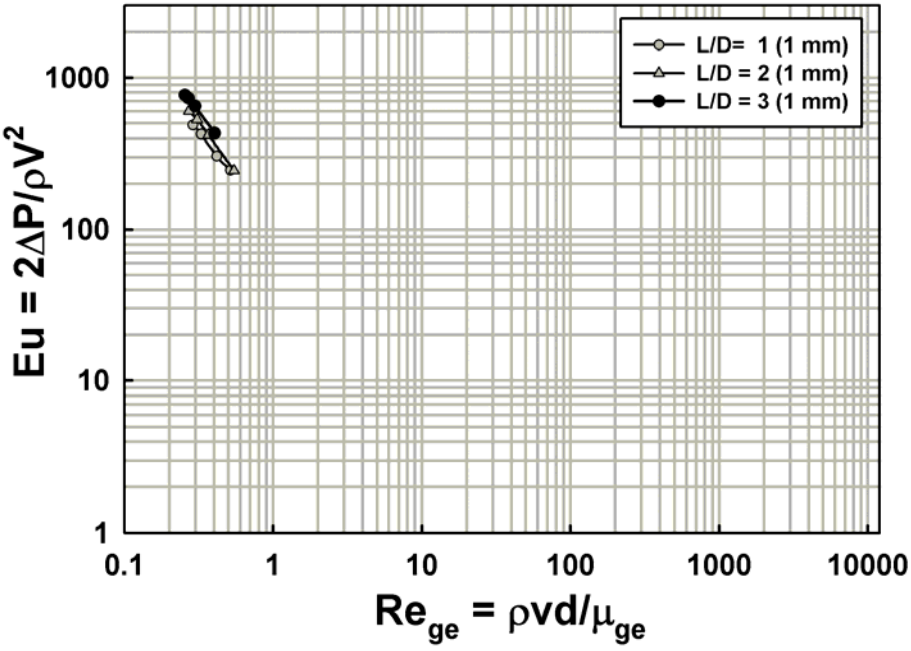

Figure C.7 Effect of Aspect Ratio on Euler Number at T ~ -30°C

LIST OF REFERENCES

AGA (1955), "Orifice Metering of Natural Gas," Gas Measurements Committee Report No. 3, American Gas Association.

Alvi, S. H., Sridharan, K. and Lakshmana Rao, N. S. (1978), "Loss Characteristics of Orifices and Nozzles," *ASME Journal of Fluids Engineering*, Vol. 100(3), pp 299-307.

ASME, (1971), "Fluid Meters," 6th Ed.

ASME, (1990), "Measurement of Fluid Flow in Pipes Using Orifice, Nozzle, and Venturi (ASME MFC-3M-1989)," American Society of Mechanical Engineers Standard.

Avallone, E. A. and Baumeister, T., III, (1996), "Mark's Standard Handbook for Mechanical Engineers," 10th Ed., McGraw-Hill.

Bird, R. B., Armstrong, R. C. and Hassager, O., (1987), "Dynamics of Polymeric Liquids: Fluid Mechanics," 2nd Ed., New York, John Wiley & Sons.

Boger, D. V. and Walters, K. W., (1993), "Rheological Phenomena in Focus," New York, Elsevier.

Bond, W. N. (1922), *Proceedings of the Physics Society*, Vol. 34, pp. 139.

Churchill, S. W. (1977), "Friction-Factor Equation Spans All Fluid Flow Regimes," *Chemical Engineering*, Vol. 84(24), pp 91-92.

Coder, D. W. (1973), "Implicit Solutions of the Unsteady Navier-Stokes Equation for Laminar Flow through an Orifice," University of Maryland, Ph.D. Thesis.

Dagan, Z., Weinbaum, S. and Pfeffer, R. (1982), "An Infinite-Series Solution for the Creeping Motion through an Orifice of Finite Length," *Journal of Fluid Mechanics*, Vol. 115, pp 505-523.

Dugdale, D. S. (1997), "Viscous Flow through a Sharp-Edged Orifice," *International Journal of Engineering Science*, Vol. 35(8), pp 725-729.

Emmons, H. W. (1997), "A Universal Orifice Flow Formula," *Thirteenth Meeting of the UNJR Panel of Fire Research and Safety, March 13-20, 1996*, Vol. 1, pp 229-236.

Epstein, M. and Kenton, M. (1989), "Combined Natural Convection and Forced Flow through Small Openings in a Horizontal Partition, with Special Reference to Flows in Multicomponent Enclosures," *ASME Journal of Heat Transfer*, pp 980-987.

Fitzgerald, J. A. and Garimella, S. V. (1997), "Visualization of the Flow Field in a Confined and Submerged Impinging Jet," *Proceedings, ASME National Heat Transfer Conference, ASME HTD*, Vol. 346(8), pp 93-99.

Fluent, (1995), "Fluent User's Guide," Lebanon, NH, Fluent, Inc.

Gan, G. and Riffat, S. B. (1997), "Pressure Loss Characteristics of Orifice and Perforated Plates," *Experimental Thermal and Fluid Science*, Vol. 14(2), pp 160-165.

Grose, R. D. (1983), "Orifice Flow at Low Reynolds Number," *Journal of Pipelines*, Vol. 3(3), pp 207-214.

Grose, R. D. (1985), "Orifice Contraction Coefficients for Inviscid Incompressible Flow," *ASME Journal of Fluids Engineering*, Vol. 107(1), pp 36-43.

Hasegawa, T., Suganuma, M. and Watanabe, H. (1997), "Anomaly of Excess Pressure Drops of the Flow through Very Small Orifices," *Physics of Fluids*, Vol. 9(1), pp 1-3.

Heskestad, G. and Spaulding, R. D. (1991), "Inflow of Air Required at Wall and Ceiling Apertures to Prevent Escape of Fire Smoke," *Proceedings of the 3rd Simposium of Fire Safety Science*, pp 919-928.

Hodgson, J. L. (1929), "The Laws of Similarity of Orifice and Nozzle Flows," *ASME Transactions*, Vol. 51, pp 303-332.

Idelchik, I. E., Malyavskaya, G. R., Martynenko, O. G. and Fried, E., (1986), "Handbook of Hydraulic Resistance," 2nd Ed., Washington, D. C., Hemisphere.

ISO-5167 (1978), "Measurement of Fluid Flow by Means of Orifices, Flow Nozzles, and Venturies."

James, A. J. (1961), "Flow through a Long Orifice," Nottingham University, B.Sc. Thesis.

Johansen, F. C. (1930), "Flow through Pipe Orifices at Low Reynolds Numbers," *Proceedings of the Royal Society of London, Series A, Containing Papers of a Mathematical and Physical Character*, Vol. 126(801), pp 231-245.

Jones, E. H. J. and Bajura, R. A. (1991), "A Numerical Analysis of Pulsating Laminar Flow through a Pipe Orifice," *ASME Journal of Fluids Engineering*, Vol. 113(2), pp 199-205.

Kayser, J. C. and Shambaugh, R. L. (1991), "Discharge Coefficients for Compressible Flow through Small-Diameter Orifices and Convergent Nozzles," *Chemical Engineering Science*, Vol. 46(7), pp 1697-1711.

Keith, J., T. G. (1971), "Finite Difference Solution of Steady Laminar Flow through a Pipe Orifice," University of Maryland, Ph.D. Thesis.

Kiljanski, T. (1993), "Discharge Coefficients of Free Jets from Orifices at Low Reynolds Numbers," *ASME Journal of Fluids Engineering*, Vol. 115(4), pp 778-781.

Kim, B. C., Pak, B. C., Cho, N. H., Chi, D. S., Choi, H. M., Choi, Y. M. and Park, K. A. (1997), "Effects of Cavitation and Plate Thickness on Small Diameter Ratio Orifice Meters," *Flow Measurement and Instrumentation*, Vol. 8(2), pp 85-92.

Lichtarowicz, A., Duggins, R. K. and Markland, E. (1965), "Discharge Coefficients for Incompressible, Non-Cavitating Flow through Long Orifices," *Journal of Mechanical Engineering Science*, Vol. 7(2), pp 210-219.

Massey, B. S., (1975), "Mechanics of Fluids," Von Nostrand Reinhold.

McNeil, D. A., Addlesee, J. and Stuart, A. (1999), "An Experimental Study of Viscous Flows in Contraction," *Journal of Loss Prevention in the Process Industries*, Vol. 12(4), pp 249-258.

Medaugh, F. W. and Johnson, G. D. (1940), "Investigation of the Discharge and Coefficients of Small Circular Orifices," *Civil Engineering*, Vol. 10(7), pp 422-424.

Miller, R. W. (1979), "The Stolz and ASME-AGA Orifice Equations Compared to Laboratory Data," *ASME Journal of Fluids Engineering*, Vol. 101(4), pp 483-490.

Miller, R. W. and Kneisel, O. (1974), "A Comparison between Orifice and Flow Nozzle Laboratory Data and Published Coefficients," *ASME Journal of Fluids Engineering*, Vol. 96(2), pp. 139.

Mincks, L. M. (2002), "Pressure Drop Characteristics of Viscous Fluid Flow across Orifices," Mechanical Engineering, Iowa State University, Ames, MS Thesis.

Morgan, J. G. D. (1963), "Flow through Long Orifice at Low Reynolds Number," Nottingham University, B.Sc. Thesis.

Morris, G. K. and Garimella, S. V. (1998), "Orifice and Impingement Flow Fields in Confined Jet Impingement," *ASME Journal of Electronic Packaging*, Vol. 120(1), pp 68-72.

Morris, G. K., Garimella, S. V. and Amano, R. S. (1996), "Prediction of Jet Impingement Heat Transfer Using a Hybrid Wall Treatment with Different Turbulent Prandtl Number Function," *ASME Journal of Heat Transfer*, Vol. 118(3), pp 562-569.

Morris, G. K., Garimella, S. V. and Fitzgerald, J. A. (1999), "Flow-Field Prediction in Submerged and Confined Jet Impingement Using the Reynolds Stress Model," *ASME Journal of Electronic Packaging*, Vol. 121(4), pp 255-262.

Munson, B. R., Young, D. F. and Okiishi, T. H., (1998), "Fundamentals of Fluid Mechanics," 3rd Ed., John Wiley & Sons, Inc.

Nigro, F. B. E., Strong, A. B. and Alpay, S. A. (1978), "A Numerical Study of the Laminar, Viscous, Incompressible Flow through a Pipe Orifice," *Journal of Fluids Engineering*, Vol. 100, pp 467-472.

Ramamurthi, K. and Nandakumar, K. (1999), "Characteristics of Flow through Small Sharp-Edged Cylindrical Orifices," *Flow Measurement and Instrumentation*, Vol. 10(3), pp 133-143.

Sahin, B. and Ceyhan, H. (1996), "Numerical and Experimental Analysis of Laminar Flow through Square-Edged Orifice with Variable Thickness," *Transactions of the Institute of Measurement and Control*, Vol. 18(4), pp 166-174.

Samanta, A. K., Banerjee, T. K. and Das, S. K. (1999), "Pressure Losses in Orifices for the Flow of Gas-Non-Newtonian Liquids," *The Canadian Journal of Chemical Engineering*, Vol. 77(3), pp 579-583.

Sampson, R. A. (1891), "On Stokes's Current Function," *Philosophical Transactions of the Royal Society of London. A*, Vol. 182, pp 449-518.

Sanderson, E. W. (1962), "Flow through Long Orifices," Nottingham University, B.Sc. Thesis.

Smith, D. and Walker, W. J. (1923), "Orifice Flow," *Proceedings, Institution of Mechanical Engineers*, pp. 23.

Sorab, J., Holdeman, H. A. and Chui, G. K. (1993), "Viscosity Prediction for Multigrade Oils," *SAE Technical Paper Series*(932833), pp 241-252.

SPSS Inc. (2004), "Sigmaplot 2001 for Windows Version 7.101", Chicago, SPSS Inc.

Sridhar, T. (1990), "Overview of the Project M1," *Journal of Non-Newtonian Fluid Mechanics*, Vol. 35(2-3), pp 85-92.

Steffe, J. F. and Salas-Valerio, W. F. (1990), "Orifice Discharge Coefficients for Power-Law Fluids," *Journal of Food Process Engineering*, Vol. 12(2), pp 89-98.

Stichlmair, J. and Mersmann, A. (1978), "Dimensioning Plate Columns for Absorption and Rectification," *International Journal of Chemical Engineering*, Vol. 18(2), pp 223-236.

Stolz, J. (1975), "An Approach toward a General Correlation of Discharge Coefficients of Orifice Plate Flowmeters," *ISO/TC30/SC2 (France 6)*, pp 645.

Tan, Q. and Jaluria, J. (1992), "Flow through Horizontal Vents as Related to Compartment Fire Environments," *NIST-GCR-92-604*, pp 1-89.

Taylor, B. N. and Kuyatt, C. E. (1993), "Guidelines for Evaluating and Expressing the Uncertainty of NIST Measurement Results," NIST/TN 1297, Report Review, National Institute of Standards & Technology, Washington, DC.

Tuve, G. L. and Sprenkle, R. E. (1933), "Orifice Discharge Coefficients for Viscous Liquids," *Instruments*, Vol. 6(1), pp 210-206.

Valle, D. D., Philippe, A. T. and Carreau, P. J. (2000), "Characterizations of the Extensional Properties of Complex Fluids Using an Orifice Flowmeter," *Journal of Non-Newtonian Fluid Mechanics*, Vol. 94(1), pp 1-13.

Ward-Smith, A. J. (1971), "A Unified Treatment of the Flow and Pressure Drop Characteristics of Constructions Having Orifices with Square Edges," *Part 4 in Pressure Losses in Ducted Flows*, London, Butterworths, Vol. Part 4.

Witte, R. (1928), "Flow Constants of the I. G. Measuring Devices for Water, Oil, Gas, and Steam," *Zeitschrift V. D. I.*, pp 1493-1502.

Zhang, Z. and Cai, J. (1999), "Compromise Orifice Geometry to Minimize Pressure Drop," *Journal of Hydraulic Engineering*, Vol. 125(11), pp 1150-1153.